Title

Interlaminar Connectivity in Mouse Primary Visual Cortex

Author

Rossa, Marley

Publication Date

2023

UNIVERSITY OF CALIFORNIA SAN DIEGO

Interlaminar Connectivity in Mouse Primary Visual Cortex

A dissertation submitted in partial satisfaction of the requirements for the degree

Doctor of Philosophy

in

Neurosciences with a specialization in Computational Neurosciences

by

Marley Rossa

Committee in Charge:
Professor Edward Callaway, Chair
Professor Brenda Bloodgood, Co-Chair
Professor Eran Mukamel
Professor Kay Tye

2023

The dissertation of Marley Rossa is approved, and it is acceptable in quality and form for publication on microfilm and electronically.

University of California San Diego

2023

DEDICATION

This dissertation is dedicated to:

Autri, my husband and life partner -- for remaining steadfast and endlessly encouraging through the ups and downs of graduate school, and whose confidence in me continues to foster confidence in myself;

Papa, the first Dr. Rossa -- for fostering my love of learning about the world, for encouraging me to carve my own path in it, and for instilling in me the values of authenticity, originality, and critical thinking;

Mom, my beacon of strength – for her sincere and unwavering support, and whose selflessness, empathy, and positivity I forever aspire to embrace, and for reminding me to not take life (or myself) too seriously;

Max, my brother – for showing me what pursuing one’s passion truly looks like.

EPIGRAPH

If I want to know how we learn and remember and represent the world,
I will go to neuroscience.

Patricia Churchland
"Causal machines". Interview with Richard Marshall, 2012

TABLE OF CONTENTS

LIST OF ABBREVIATIONS

ChR2	Channelrhodopsin-2
CT	Corticothalamic
LGN	Lateral geniculate nucleus [of the thalamus]
EPSC	Excitatory Postsynaptic Current
EPSQ	Excitatory Postsynaptic Charge / Integrated Postsynaptic Current
ET	Extratelencephalic
FB	Feedback
FF	Feedforward
IT	Intratelencephalic
LGN	Lateral geniculate nucleus (of the thalamus)
RVdG	glycoprotein-deleted rabies virus
scRNAseq	Single-cell RNA sequencing
Sst	Somatostatin
Pvalb	Parvalbumin
Vip	Vasoactive intestinal peptide
L2/3, L4, etc.	Layers 2/3, 4, etc. of the cerebral cortex
V1	Primary visual cortex

LIST OF FIGURES

LIST OF TABLES

ACKNOWLEDGEMENTS

I am forever grateful to Professor Ed Callaway for his support as my mentor and committee chair. I have grown exponentially as a scientist under his mentorship, and the independence he has allowed me and trust he has put in me have made me a more competent and confident scientist as well.

I would like to acknowledge and thank all members of the Callaway lab for fostering a supportive and fun learning environment. I especially want to thank Dr. Joshua Nichols for his patience and mentorship in teaching me how to patch and be a successful electrophysiologist, Dr. Maribel Patiño for her advice and guidance in pioneering the START project described in Chapter 1, and Tyler Kearse, who worked with me as a technician for the past 1.5 years and whose efforts contributed immensely to anterograde tracer method development in the lab (not described here).

I also thank my thesis committee: Professors Brenda Bloodgood, Eran Mukamel, and Kay Tye for their constructive feedback regarding this work. Dr. Bloodgood was especially helpful in technical matters relating to optimizing brain slicing protocols and obtaining healthy cells for patch-clamp recording in Chapter 2. Dr. Mukamel was gracious in setting aside extensive time to explain and construct UMAP analyses for Chapter 1 as well as provide guidance regarding PCA and an LMEM model for data in Chapter 2. Dr. Tye provided helpful and encouraging advice for weaving together a coherent narrative and constructing a thoughtful scientific presentation.

I am grateful to my family and friends for providing an incredible support network while I pursued my PhD. I also thank Dharma for living up to her title of Emotional Support Kitty.

Chapter 1, in full, is currently being prepared for submission for publication of the material. Patiño M & Rossa MA, Lagos WM, Patne N, Callaway EM (2023). The dissertation author was a co-first author and one of 2 primary investigators of this paper.

Chapter 2, in full, is currently being prepared for submission for publication and will include Professor Edward Callaway as the senior author. The dissertation author was the primary investigator and author of this chapter.

VITA

2014	Bachelor of Science, Neuroscience Bachelor of Arts, Philosophy Duke University, Durham, NC, USA
2023	Doctor of Philosophy, Neurosciences with a Specialization in Computational Neurosciences University of California San Diego, La Jolla, CA, USA

PUBLICATIONS

Sibener LJ, Kirchgessner MA, Steiner S, Santiago C, Cassataro D, **Rossa M**, Profaci CP, Padilla-Coreano N. (2022). Lessons from the Stories of Women in Neuroscience. Journal of Neuroscience 42(24) 4769-4773. DOI: 10.1523/JNEUROSCI.0536-22.2022.

Drucker CB, **Rossa M,** Brannon, EM (2016). Comparison of discrete ratios by rhesus macaques (*Macaca mulatta*). *Animal Cognition* 19(1): 75-89. DOI: 10.1007/s10071-015-0914-9.

ABSTRACT OF THE DISSERTATION

Interlaminar Connectivity in Mouse Primary Visual Cortex

by

Marley Rossa

Doctor of Philosophy in Neurosciences with a Specialization in Computational Neurosciences

University of California San Diego, 2023

Professor Edward Callaway, Chair
Professor Brenda Bloodgood, Co-Chair

A distinguishing feature of the mammalian cerebral cortex is its laminar architecture, each layer containing a unique composition of neuronal types with distinct morphologies, molecular markers, and electrophysiological properties. These neurons form precise, specific synaptic connections with one another to form complex microcircuits that underlie sensory information processing. By compartmentalizing computation into layers, the cortex can

efficiently channel and transform information to represent and interact with the external world. Therefore, deciphering the precise input and output connectivity structure of different neuronal types in the context of their respective layers is necessary to fully appreciate their unique functional roles in the representation and manipulation of sensory information. This dissertation builds on the traditional idea of a canonical interlaminar circuit by characterizing fundamental intracortical connections between excitatory and inhibitory cell types. Chapter 1 explores the relative functional input distributions from 5 layer-specific excitatory subpopulations to 4 cell types in mouse primary visual cortex (V1). By optogenetically activating these excitatory subpopulations and recording from targeted excitatory and inhibitory subtypes across cortical layers 2/3-6, I elucidate a complex interlaminar network that provides a novel framework for visual information processing. In Chapter 2, I approach the interlaminar connectivity of mouse V1 from a transcriptomic perspective using our newly developed method Single Transcriptome Assisted Rabies Tracing (START). By combining rabies tracing using glycoprotein (G)-deleted rabies virus (RVdG) with snRNAseq, we identify, and transcriptomic ally characterize cells projecting to the same layer-specific subpopulations as in Chapter 1. We find that START generates results consistent with established circuit models validating the utility of START as a circuit tracing tool. More importantly, with the increased cell type granularity achieved with transcriptomic characterization of inputs, we were able to uncover specific subtypes of somatostatin and parvalbumin interneurons that provide input to excitatory cells across layers. Taken together, findings from Chapters 1 and 2 demonstrate layer and cell type specificity in cortical circuit structure, indicating that a cell’s laminar position and synaptic connectivity are deeply intertwined with its functional role. Understanding cell type diversity in the context of circuit architecture forms the foundation of a novel framework for cortical information processing.

INTRODUCTION

The enormous computational power of the human brain is ultimately achieved through the communication between its some 100 billion neurons[1], each with the ability to form local and long-range synaptic contacts. Crucially, neurons do not form connections randomly but instead are highly selective with whom they communicate. This inherent selectivity and tendency of particular neurons to synapse onto only a subset of others gives rise to hierarchically organized and functionally interconnected circuits that, while complex, simultaneously produce our seamless perception of the world and our ability to interact with it. In particular, the mammalian neocortex represents a central hub for sensory information processing. The visual cortex, for example, receives inputs originating as spots of light in the visual field detected by retinal photoreceptors and relayed through thalamus[2,3]. Neurons in cortical microcircuits then transform these spots of light into representations of lines, edges, and contrasting colors. As this information traverses the cortical hierarchy, its representation manifests as neurons tuned to discrete shapes, textures, and recognizable objects, ultimately forming a unified visual scene.

Many aspects of cortical organization and structure are conserved across functional areas and species[4], suggesting that the underlying principles of microcircuit architecture play a critical role in cortical function. Mapping the detailed connectivity of cortical neurons remains a primary objective in the field, and doing so will enable us to understand how these computations are performed[5]. To fully understand how its form gives rise to function, several large-scale studies have focused on understanding cortical neuron diversity through classification into types by their morphology, molecular markers, and their intrinsic physiology[6]. These studies raise important questions about circuit organization at the level of these cell types. Specifically, the organization of the cortex into 6 characteristic layers remains a central tenet of modern theories of brain function[7].

Significance of cortical laminae

Evolutionarily, based on commonalities in gene expression between cell types residing in particular layers across species, the cortex's laminar structure is thought to have originated from 3-layer olfactive cortex, with 3 primary (excitatory) cell types containing distinct basic circuit modules; corticothalamic (CT), pyramidal tract (PT), and intratelencephalic (IT) cells and their associated interneurons, each with their own unique modular circuit structure. Of the 3 aforementioned cell types, only IT neurons project within cortex; thus, neocortical lamination reflects increased IT connectivity (expansion of the IT circuit module)[8]. While the cortex's organization into layers could simply be a byproduct of neocortical evolution without a specific role in cortical function, the predominating theory in the literature posits that the conservation of laminar structure serves an important functional purpose[8]. Additionally, a substantial body of work has attributed unique functions to each layer[9] and to cell populations residing in those layers[10]. For example, CT pyramidal cells specific to L6 connect to thalamic nuclei and TRN[10], while L2/3 principal cells provide cortico-cortical connections[11]. Functioning of distinct layers as computational units includes the idea that additional layers were acquired to accommodate additional interlaminar cortico-cortical processing and association (IT cells) while relaying sensory inputs and motor outputs through longer-routing ET projections. Thus, increased layering of IT cells and elaboration of cortical areas give cortex the ability to represent the complexities of the world.

The cerebral cortex's unique developmental trajectory further underscores a potential precise function of each layer. In particular, neurons formed in the ventricular zone migrate to a precise final laminar location in a precisely timed, sequential process. L1 is the most superficial layer and is formed first, L4-L6 are formed next, and L2/L3 are formed last[12]. Each set of layers includes a different composition of cell types with distinct developmentally relevant genes expressed[13]. The cortical layers' stereotyped developmental timelines, as well as the migration pathways and genetic diversity of the neurons they contain, suggests they may serve distinct functional purposes in how information is compartmentalized in cortex.

When considering their distinct cellular composition and connectivity structure, each cortical lamina may be thought of as its own computational unit. The specificity of these cortical networks and subnetworks demands further characterization in the context of laminar location, as visual information from thalamus is received in upper layers and is transformed and filtered, transmuted and further deconstructed with each additional synaptic contact. One predominating theory of interlaminar computation posits that upper layers may serve to transform information, while lower layers preserve functional maps[14]. Input can be topographically precise, widespread (nonspecific) or patchy (somewhere in between)[15]. Focused projections preserve architecture of their origin while diverging projections rearrange & form new sensory maps. In another theoretical framework that sees sensory processing as probabilistic inference, neurons in different layers play unique roles in computing conditional probabilities that a given pattern of input represents a particular sensory stimulus[16,17]. This model posits that principal cells in superficial layers compare afferent input with an internal model of the sensory environment and pass this information across layers through feedback connections, while neurons in deeper layers encode the predictions to which bottom-up information is compared. Ultimately, in order to understand how a coherent visual perception of the world is rendered, we need to figure out where these layer-specific subnetworks are sending their information, and to whom.

Existence of a canonical cortical circuit

The true significance of the cortex's laminar structure can only be fully grasped when the precise connectivity between its constituent subpopulations is mapped. The earliest attempts to map the circuit can be attributed to work from Gilbert & Wiesel and Binzegger in the 1980s, primarily consisting of anatomical reconstructions of neurons in cat visual cortex. The finding that cells in each layer form precise, specific connections with cells in other layers formed the blueprint for a simple, feedforward "canonical circuit" model where information from thalamus is primarily relayed to L4 IT cells from core thalamic cells[18], L4 projects to L2/3, and L2/3 down to deeper layers 5/6 before being routed to other cortical and subcortical regions[11,19–21]. Since then, substantial work has gone into more finely characterizing these connections. For example, Matrix cells from higher order thalamic nuclei project to L1 and largely avoid L4[18]. Despite their extensive input to L2/3 and L5[22], L4 IT neurons do not receive comparable reciprocal input from these layers. Unlike L4 IT neurons which are specialized for processing extrinsic inputs, IT neurons in other layers are thought to primarily integrate signals from other cortical inputs; L2/3 IT tend to be bidirectionally connected with L5 IT neurons[11,14]. L6 IT neurons are the least studied IT group, but some work[23] suggests that they receive input primarily from other deep layer neurons. ET neurons function as integrators of local cortical and thalamic inputs to relay information to distal subcortical structures, suggested by their extensive input from IT neurons in all cortical layers, especially L2/3 IT. L6 CT neurons lack substantial local input from other cortical layers and instead receive most of the inputs from higher order cortical areas[24], while arborizing in L4[21].

Clearly, across the past several decades of intricate circuit mapping in mammalian visual cortex, layer-specific functional subpopulations have been identified and the general cortical circuit structure is becoming increasingly focused. Moreover, as our current understanding of the circuit continues to evolve and become more refined, we can appreciate that the true circuit structure is highly nuanced, immensely more complex than the original feedforward canonical model. Despite these advances, however, some challenges remain, 2 of which this dissertation seeks to address. First, the extent to which axonal arborization and morphological reconstructions are reflected in these neuronal populations' *functional* connectivity (i.e., the number and strength of synaptic inputs from one population to another) between remains to be seen and is the primary focus of Chapter 1. Second, to what extent are broad designations in cell types sufficient for understanding the computational structure of the sensory circuit? Emerging evidence, especially from single cell transcriptome sequencing but also from other high-throughput assays, suggests a much greater diversity in cell types exists than was previously appreciated in the development of the canonical circuit model. More granular distinctions between cells and their subtypes will therefore be necessary to build accurate theoretical models of cortex and to mechanistically identify how the cortex modifies sensory information.

Cell type classification schemes & levels of organization

One crucial point of note here, one that immediately becomes apparent in discussing layer-specific cell types—the notion of a cortical layer and the cell types that reside within it are fundamentally intertwined. Thus, when considering the functional relevance of cortical lamination, a tangential yet equally important question is: what is the functional significance of segregated and functionally distinct neuron populations within a single cortical region? To address this question, we must integrate our understanding of cell types with their functional roles and with whom they form synaptic contacts. To start, we can turn to the two major classes of neurons, glutamatergic excitatory pyramidal neurons and GABAergic inhibitory interneurons. While excitatory neurons are responsible for propagating signals in a feedforward manner, inhibitory interneurons gate signal flow and sculpt network dynamics through phenomena such as feedback inhibition[25,26]. Although inhibitory interneurons represent a minority of cortical neurons[27], dense axonal arborization allows them to balance and shape excitatory neuron activity, maintaining a fine-tuned excitation-inhibition balance throughout the cortex[28].

Cortical interneurons are a diverse population that have diverse morphological, molecular, and electrophysiological properties. They can be organized into several major groups based on their developmental origins (i.e. whether they are derived from the medial ganglionic or caudal ganglionic eminences), expression of selective markers: parvalbumin (Pvalb), somatostatin (Sst) and serotonin receptor 5HT3aR[28,29]. Physiologically, Pvalb basket cells, the largest group of cortical interneurons, exhibit fast-spiking firing properties and their basket-shaped axonal boutons preferentially target the perisomatic region of their innervation target[28]. The majority of Sst interneurons, termed Martinotti cells, are characterized by an ascending axon that arborizes in layer 1 and targets the distal dendritic compartments of neurons[28]. The 5HT3aR population, includes vasoactive intestinal peptide (Vip) interneurons that are characterized by irregular burst spike firing properties and bipolar morphology[28]. Furthermore, connectivity studies[30–32] have shown that Pvalb interneurons not only inhibit pyramidal neurons, but also selectively inhibit one another. In contrast, Sst interneurons inhibit all inhibitory populations, except themselves. Vip interneurons preferentially inhibit Sst interneurons and provide little input to pyramidal neurons[33–35].

In addition to connectivity studies, with the emergence of tools to manipulate and monitor activity of defined cell types in vivo, specific inhibitory populations have become implicated in specific circuit functions. Studies across multiple cortical areas have implicated Pvalb interneurons in gain control, and they may also coordinate large-scale activity in the temporal domain due to their precise timing/signal filtering; their dense connections may assist in generating gamma oscillations during attention and arousal[36]. Sst interneurons have been implicated in the suppression of lateral and top-down interactions, and Vip interneurons in cortical disinhibition (by predominately inhibiting Sst interneurons[37]) as well as modulation of visual feature selectivity[38,39].

Like inhibitory neurons, excitatory neurons in the primary visual cortex have diverse projection properties, morphology, and intrinsic physiology. They can be divided into three main groups according to their axonal projection patterns: intratelencephalic (IT) neurons, extratelencephalic (ET) neurons, and corticothalamic (CT) neurons. IT excitatory neurons are found across layers (L) 2-6 of the cortex and project to other neurons within the telencephalon including the striatum, amygdala, claustrum and ipsilateral and contralateral cerebral cortices[24]. ET neurons are large pyramidal neurons found primarily in L5b[24] and project to subcortical destinations such as the brainstem, spinal cord, and thalamus. CT neurons are found in L6 and project primarily to the ipsilateral thalamus. Taken together, systematic categorization of neuronal subpopulations reveals that their laminar location, in addition to anatomical and functional properties, is a prominent and distinguishing feature across levels of the taxonomic hierarchy.

Functional, cell type-specific organization of interlaminar circuits

A given neuron's somatic location can likely be associated with its functional role in cortical computation. To bridge this gap, one must understand its fundamental circuit connectivity structure. On the broadest level, the circuit must exhibit balance between excitation and inhibition[40,41]. Neurons require an extremely finely structured balance of excitation and inhibition to generate complex behaviors; too much excitation can kill a neuron and/or destabilize a neural network[41–43] while too much inhibition could lead to complete silencing of a neuron and therefore an inability to feed forward any meaningful information. Moreover, as previously mentioned, different inhibitory subtypes exhibit a vast array of electrophysiological and biophysical properties, as evidenced by differential distributions of transmembrane ion channels and transporters and synapses made on different cell types and subcellular compartments as previously discussed. Aside from differences in inhibitory neuron morphology, activity differences result from differential distribution of ion channels: the amplitude, and instantaneous frequency, and subcellular location of synaptic input to a given cell--can lead to differential modifications of output. Some effort has been made to determine different functional roles of distinct inhibitory neuron types given their distinct anatomical and functional properties: Vip neurons, for example, may underlie the amplification of visual information outside of one's field of attention and have frequently been demonstrated to underlie modulation of behavioral state Pvalb and Sst neurons may contribute to perceptual phenomena including gain control and surround suppression, respectively.

Data from the Allen Institute suggests that MET types typically co-occur in 1 or 2 distinct layers: they are not evenly distributed. This further highlights that interneuron subtypes and their connectivity are layer dependent. Experiments functionally characterizing canonical circuits have largely used paired recordings and direct comparisons of synaptic responses between neurons in a single layer[30,44]. Given the remarkable diversity of interneuron types, it's likely that these canonical connectivity rules in fact do not hold across cortical layers.

Studies probing functional connectivity using paired recordings also run into the issue of cut axons. This is a major caveat because when to directly accurately compare connections between different cell types, whether or not a connection is detected depends on whether intrinsic connectivity is actually preserved in the recording setup. Moreover, because neuron types have different branching patterns and vastly different morphologies the likelihood of the original connection being preserved is cell type dependent. This therefore introduces a huge bias in these experiments, where cells whose connections are more distal are more likely to be cut. Large-scale functional connectivity studies that bypass the issue of cut axons are needed to determine the relative distribution of synaptic connectivity between layers and between cell populations residing in those layers. To this end, in Chapter 1 I describe a series of experiments where I use transgenic mouse lines, viral vectors, and optogenetic approaches combined with targeted whole cell recordings to bypass the issue of cut axons and determine the extent to which layer-specific excitatory populations in each cortical layer provide input to distinct populations in other layers.

Anatomical approaches for fine-scale dissection of cortical circuitry

While key principles of cortical connectivity continue to be uncovered, a detailed understanding of the specialized connectivity patterns underlying cortical networks remain largely incomplete and many aspects of cortical circuit organization remain unknown. Single-cell sequencing technologies have only recently begun to reveal the extent of cortical cell type diversity. Recent studies utilizing scRNAseq to study cortical cell type diversity across cortical areas, have found large numbers of clusters corresponding to transcriptomic cell types. In particular, work from the Allen Institute[45] has amassed scRNAseq data from more than 23,000 neurons from primary visual cortex (V1) and the anterior lateral motor cortex (ALM) and revealed 133 distinct transcriptomic cell types: 61 inhibitory types, 56 glutamatergic, and 16 non-neuronal types. The transcriptomic inhibitory cell types identified included 20 Sst+, 10 Pvalb+, 16 Vip+, and 13 5HTR3A+/Vip- clusters, subdividing the major established inhibitory cell classes into a multitude of cell subtypes. Importantly, transcriptomic correlates of electrophysiological and morphological diversity within and across excitatory and inhibitory neuron have already begun to be established in multiple studies [45–47]. Albeit relying on in vitro strategies, correlation was also established between other transcriptomic clusters and morphological and electrophysiological distinct cell types in studies using PatchSeq to simultaneously conduct single-cell characterization of gene expression and electrophysiology in the same cell[46,48]. Together, these studies demonstrate that the utility of transcriptomic characterization in untangling the precise circuit connections underlying cortical function.

In addition to transcriptomic approaches, Monosynaptic rabies tracing using glycoprotein (G)-deleted rabies virus (RVdG) has been widely used for circuit tracing studies because it allows identification of the direct presynaptic inputs to specific cell types or to single neurons of interest, across the whole brain[31,49,50]. G-deleted rabies tracing has been used in previous studies to identify inputs to layer specific excitatory neurons[51], local interlaminar connectivity[52], and the brain-wide inputs to cortical inhibitory neurons[31] and excitatory neurons[52,53]. However, these studies focus on regional distribution of synaptic input and only superficially investigate cell types providing that input. Crucially, as new tools for dissecting neural circuits continue to emerge across transcriptomic, imaging, and electrophysiological modalities, distinctions between interneuron types that are limited to general subclasses (e.g., Sst, Vip+, and Pvalb+) may be insufficient for capturing inhibitory neuron diversity. In Chapter 2, we therefore seek to understand cortical wiring specificity on a finer, subclass level by combining monosynaptic rabies tracing with single nucleus RNA sequencing (snRNAseq) and determining transcriptomic cell type specificity by which interlaminar cortical microcircuits are wired. We demonstrate use of this novel combination of tools, which we term Single Transcriptome investigate local interlaminar connectivity in mouse primary visual cortex and provide compelling evidence that START can facilitate the discovery of new cortical circuit motifs.

References

1. Purves, Dale, Augustine, George J., Fitzpatrick, D., Katz, Lawrence, LaMantia, Anthony-Samuel, McNamara, James, & Williams, Mark. (2001). *Neuroscience* (2nd ed.). Sinauer Associates.
2. Douglas, R., Martin, K., & Whitteridge, D. (1989). A Canonical Microcircuit for Neocortex. *Neural Computation - NECO*, *1*, 480–488. https://doi.org/10.1162/neco.1989.1.4.480
3. Gilbert, C. D. (1983). Microcircuitry of the visual cortex. *Annual Review of Neuroscience*, *Vol. 6*, 217–247. https://doi.org/10.1146/annurev.ne.06.030183.001245
4. Douglas, R. J., & Martin, K. A. C. (2004). Neuronal circuits of the neocortex. *Annual Review of Neuroscience*, *27*, 419–451. https://doi.org/10.1146/annurev.neuro.27.070203.144152
5. Luo, L., Callaway, E. M., & Svoboda, K. (2018). Genetic Dissection of Neural Circuits: A Decade of Progress. *Neuron*, *98*(2), 256–281. https://doi.org/10.1016/j.neuron.2018.03.040
6. Armand, E. J., Li, J., Xie, F., Luo, C., & Mukamel, E. A. (2021). Single-Cell Sequencing of Brain Cell Transcriptomes and Epigenomes. *Neuron*, *109*(1), 11–26. https://doi.org/10.1016/j.neuron.2020.12.010
7. Raizada, R. D. S., & Grossberg, S. (2003). Towards a Theory of the Laminar Architecture of Cerebral Cortex: Computational Clues from the Visual System. *Cerebral Cortex*, *13*(1), 100–113. https://doi.org/10.1093/cercor/13.1.100
8. Shepherd, G. M., & Rowe, T. B. (2017). Neocortical Lamination: Insights from Neuron Types and Evolutionary Precursors. *Frontiers in Neuroanatomy*, *11*, 100. https://doi.org/10.3389/fnana.2017.00100

9. Larkum, M. E., Petro, L. S., Sachdev, R. N. S., & Muckli, L. (2018). A Perspective on Cortical Layering and Layer-Spanning Neuronal Elements. *Frontiers in Neuroanatomy*, *12*, 56. https://doi.org/10.3389/fnana.2018.00056
10. Thomson, A. M., & Lamy, C. (2007). Functional Maps of Neocortical Local Circuitry. *Frontiers in Neuroscience*, *1*(1), 19–42. https://doi.org/10.3389/neuro.01.1.1.002.2007
11. Gilbert, C. D. (1983). Microcircuitry of the Visual Cortex. *Annual Review of Neuroscience*, *6*(1), 217–247. https://doi.org/10.1146/annurev.ne.06.030183.001245
12. Meyer, G. (2007). Genetic control of neuronal migrations in human cortical development. *Advances in Anatomy, Embryology, and Cell Biology*, *189*, 1 p preceding 1, 1–111.
13. Germain, N., Banda, E., & Grabel, L. (2010). Embryonic stem cell neurogenesis and neural specification. *Journal of Cellular Biochemistry*, *111*(3), 535–542. https://doi.org/10.1002/jcb.22747
14. Burkhalter, A. (1989). Intrinsic connections of rat primary visual cortex: Laminar organization of axonal projections. *Journal of Comparative Neurology*, *279*(2), 171–186. https://doi.org/10.1002/cne.902790202
15. Watakabe, A., Skibbe, H., Nakae, K., Abe, H., Ichinohe, N., Rachmadi, M. F., Wang, J., Takaji, M., Mizukami, H., Woodward, A., Gong, R., Hata, J., Van Essen, D. C., Okano, H., Ishii, S., & Yamamori, T. (2023). Local and long-distance organization of prefrontal cortex circuits in the marmoset brain. *Neuron*, S0896-6273(23)00338-0. https://doi.org/10.1016/j.neuron.2023.04.028
16. Adesnik, H., & Naka, A. (2018). Cracking the function of layers in the sensory cortex. *Neuron*, *100*(5), 1028–1043. https://doi.org/10.1016/j.neuron.2018.10.032
17. Bastos, A. M., Usrey, W. M., Adams, R. A., Mangun, G. R., Fries, P., & Friston, K. J. (2012). Canonical Microcircuits for Predictive Coding. *Neuron*, *76*(4), 695–711. https://doi.org/10.1016/j.neuron.2012.10.038
18. Jones, E. G. (2001). The thalamic matrix and thalamocortical synchrony. *Trends in Neurosciences*, *24*(10), 595–601. https://doi.org/10.1016/S0166-2236(00)01922-6
19. Binzegger, T. (2004). A Quantitative Map of the Circuit of Cat Primary Visual Cortex. *Journal of Neuroscience*, *24*(39), 8441–8453. https://doi.org/10.1523/JNEUROSCI.1400-04.2004
20. Binzegger, T., Douglas, R. J., & Martin, K. A. C. (2009). Topology and dynamics of the canonical circuit of cat V1. *Neural Networks*, *22*(8), 1071–1078. https://doi.org/10.1016/j.neunet.2009.07.011
21. Gilbert, C. D., & Wiesel, T. N. (1989). Columnar specificity of intrinsic horizontal and corticocortical connections in cat visual cortex. *The Journal of Neuroscience: The Official Journal of the Society for Neuroscience*, *9*(7), 2432–2442. https://doi.org/10.1523/JNEUROSCI.09-07-02432.1989
22. Thomson, A. M., & Bannister, A. P. (2003). Interlaminar Connections in the Neocortex. *Cerebral Cortex*, *13*(1), 5–14. https://doi.org/10.1093/cercor/13.1.5
23. Vélez-Fort, M., Rousseau, C. V., Niedworok, C. J., Wickersham, I. R., Rancz, E. A., Brown, A. P. Y., Strom, M., & Margrie, T. W. (2014). The Stimulus Selectivity and Connectivity of Layer Six Principal Cells Reveals Cortical Microcircuits Underlying Visual Processing. *Neuron*, *83*(6), 1431–1443. https://doi.org/10.1016/j.neuron.2014.08.001
24. Harris, K. D., & Shepherd, G. M. G. (2015). The neocortical circuit: Themes and variations. *Nature Neuroscience*, *18*(2), Article 2. https://doi.org/10.1038/nn.3917

25. Burkhalter, A., D'Souza, R. D., Ji, W., & Meier, A. M. (2023). Integration of Feedforward and Feedback Information Streams in the Modular Architecture of Mouse Visual Cortex. *Annual Review of Neuroscience*, *46*(1), null. https://doi.org/10.1146/annurev-neuro-083122-021241
26. Callaway, E. M. (2004). Feedforward, feedback and inhibitory connections in primate visual cortex. *Neural Networks*, *17*(5–6), 625–632. https://doi.org/10.1016/j.neunet.2004.04.004
27. Markram, H., Toledo-Rodriguez, M., Wang, Y., Gupta, A., Silberberg, G., & Wu, C. (2004). Interneurons of the neocortical inhibitory system. *Nature Reviews Neuroscience*, *5*(10), Article 10. https://doi.org/10.1038/nrn1519
28. Tremblay, R., Lee, S., & Rudy, B. (2016). GABAergic Interneurons in the Neocortex: From Cellular Properties to Circuits. *Neuron*, *91*(2), 260–292. https://doi.org/10.1016/j.neuron.2016.06.033
29. Zeng, H., & Sanes, J. R. (2017). Neuronal cell-type classification: Challenges, opportunities and the path forward. *Nature Reviews Neuroscience*, *18*(9), Article 9. https://doi.org/10.1038/nrn.2017.85
30. Pfeffer, C. K., Xue, M., He, M., Huang, Z. J., & Scanziani, M. (2013). Inhibition of inhibition in visual cortex: The logic of connections between molecularly distinct interneurons. *Nature Neuroscience*, *16*(8), 1068–1076. https://doi.org/10.1038/nn.3446
31. Wall, N. R., De La Parra, M., Sorokin, J. M., Taniguchi, H., Huang, Z. J., & Callaway, E. M. (2016). Brain-Wide Maps of Synaptic Input to Cortical Interneurons. *The Journal of Neuroscience*, *36*(14), 4000–4009. https://doi.org/10.1523/JNEUROSCI.3967-15.2016
32. Xu, H., Jeong, H.-Y., Tremblay, R., & Rudy, B. (2013). Neocortical Somatostatin-Expressing GABAergic Interneurons Disinhibit the Thalamorecipient Layer 4. *Neuron*, *77*(1), 155–167. https://doi.org/10.1016/j.neuron.2012.11.004
33. Karnani, M. M., Agetsuma, M., & Yuste, R. (2014). A blanket of inhibition: Functional inferences from dense inhibitory circuit structure. *Current Opinion in Neurobiology*, *0*, 96–102. https://doi.org/10.1016/j.conb.2013.12.015
34. Karnani, M. M., Jackson, J., Ayzenshtat, I., Hamzehei Sichani, A., Manoocheri, K., Kim, S., & Yuste, R. (2016). Opening Holes in the Blanket of Inhibition: Localized Lateral Disinhibition by VIP Interneurons. *Journal of Neuroscience*, *36*(12), 3471–3480. https://doi.org/10.1523/JNEUROSCI.3646-15.2016
35. Karnani, M. M., Jackson, J., Ayzenshtat, I., Tucciarone, J., Manoocheri, K., Snider, W. G., & Yuste, R. (2016). Cooperative subnetworks of molecularly-similar interneurons in mouse neocortex. *Neuron*, *90*(1), 86–100. https://doi.org/10.1016/j.neuron.2016.02.037
36. Cardin, J. A., Carlén, M., Meletis, K., Knoblich, U., Zhang, F., Deisseroth, K., Tsai, L.-H., & Moore, C. I. (2009). Driving fast-spiking cells induces gamma rhythm and controls sensory responses. *Nature*, *459*(7247), 663–667. https://doi.org/10.1038/nature08002
37. Kepecs, A., & Fishell, G. (2014). Interneuron cell types are fit to function. *Nature*, *505*(7483), Article 7483. https://doi.org/10.1038/nature12983
38. Millman, D. J., Ocker, G. K., Caldejon, S., Kato, I., Larkin, J. D., Lee, E. K., Luviano, J., Nayan, C., Nguyen, T. V., North, K., Seid, S., White, C., Lecoq, J., Reid, C., Buice, M. A., & de Vries, S. E. (2020). VIP interneurons in mouse primary visual cortex selectively enhance responses to weak but specific stimuli. *ELife*, *9*, e55130. https://doi.org/10.7554/eLife.55130

39. Muñoz, W., Tremblay, R., Levenstein, D., & Rudy, B. (2017). Layer-specific modulation of neocortical dendritic inhibition during active wakefulness. *Science*, *355*(6328), 954–959. https://doi.org/10.1126/science.aag2599
40. Adesnik, H. (2018). Layer-specific excitation/inhibition balances during neuronal synchronization in the visual cortex: Laminar origins of neural synchronization in V1. *The Journal of Physiology*, *596*(9), 1639–1657. https://doi.org/10.1113/JP274986
41. Sanzeni, A., Akitake, B., Goldbach, H. C., Leedy, C. E., Brunel, N., & Histed, M. H. (2020). Inhibition stabilization is a widespread property of cortical networks. *ELife*, *9*, e54875. https://doi.org/10.7554/eLife.54875
42. Litwin-Kumar, A., Rosenbaum, R., & Doiron, B. (2016). Inhibitory stabilization and visual coding in cortical circuits with multiple interneuron subtypes. *Journal of Neurophysiology*, *115*(3), 1399–1409. https://doi.org/10.1152/jn.00732.2015
43. Hutt, A., Rich, S., Valiante, T. A., & Lefebvre, J. (2022). *Intrinsic neural diversity quenches the dynamic volatility of neural networks* (p. 2022.08.25.505270). bioRxiv. https://doi.org/10.1101/2022.08.25.505270
44. Jiang, X., Shen, S., Cadwell, C. R., Berens, P., Sinz, F., Ecker, A. S., Patel, S., & Tolias, A. S. (2015). Principles of connectivity among morphologically defined cell types in adult neocortex. *Science*, *350*(6264), aac9462. https://doi.org/10.1126/science.aac9462
45. Tasic, B., Yao, Z., Graybuck, L. T., Smith, K. A., Nguyen, T. N., Bertagnolli, D., Goldy, J., Garren, E., Economo, M. N., Viswanathan, S., Penn, O., Bakken, T., Menon, V., Miller, J., Fong, O., Hirokawa, K. E., Lathia, K., Rimorin, C., Tieu, M., … Zeng, H. (2018). Shared and distinct transcriptomic cell types across neocortical areas. *Nature*, *563*(7729), 72–78. https://doi.org/10.1038/s41586-018-0654-5
46. Gouwens, N. W., Sorensen, S. A., Baftizadeh, F., Budzillo, A., Lee, B. R., Jarsky, T., Alfiler, L., Baker, K., Barkan, E., Berry, K., Bertagnolli, D., Bickley, K., Bomben, J., Braun, T., Brouner, K., Casper, T., Crichton, K., Daigle, T. L., Dalley, R., … Zeng, H. (2020). Integrated Morphoelectric and Transcriptomic Classification of Cortical GABAergic Cells. *Cell*, *183*(4), 935-953.e19. https://doi.org/10.1016/j.cell.2020.09.057
47. Naka, A., Veit, J., Shababo, B., Chance, R. K., Risso, D., Stafford, D., Snyder, B., Egladyous, A., Chu, D., Sridharan, S., Mossing, D. P., Paninski, L., Ngai, J., & Adesnik, H. (2019). Complementary networks of cortical somatostatin interneurons enforce layer specific control. *ELife*, *8*, e43696. https://doi.org/10.7554/eLife.43696
48. Gouwens, N. W., Sorensen, S. A., Berg, J., Lee, C., Jarsky, T., Ting, J., Sunkin, S. M., Feng, D., Anastassiou, C. A., Barkan, E., Bickley, K., Blesie, N., Braun, T., Brouner, K., Budzillo, A., Caldejon, S., Casper, T., Castelli, D., Chong, P., … Koch, C. (2019). Classification of electrophysiological and morphological neuron types in the mouse visual cortex. *Nature Neuroscience*, *22*(7), 1182–1195. https://doi.org/10.1038/s41593-019-0417-0
49. Wickersham, I. R., Lyon, D. C., Barnard, R. J. O., Mori, T., Finke, S., Conzelmann, K.-K., Young, J. A. T., & Callaway, E. M. (2007). Monosynaptic Restriction of Transsynaptic Tracing from Single, Genetically Targeted Neurons. *Neuron*, *53*(5), 639–647. https://doi.org/10.1016/j.neuron.2007.01.033
50. Wickersham, I. R., Finke, S., Conzelmann, K.-K., & Callaway, E. M. (2007). Retrograde neuronal tracing with a deletion-mutant rabies virus. *Nature Methods*, *4*(1), 47–49. https://doi.org/10.1038/nmeth999

51. Yetman, M. J., Washburn, E., Hyun, J. H., Osakada, F., Hayano, Y., Zeng, H., Callaway, E. M., Kwon, H.-B., & Taniguchi, H. (2019). Intersectional Monosynaptic Tracing for Dissecting Subtype-Specific Organization of GABAergic Interneuron Inputs. *Nature Neuroscience*, *22*(3), 492–502. https://doi.org/10.1038/s41593-018-0322-y
52. DeNardo, L. A., Berns, D. S., DeLoach, K., & Luo, L. (2015). Connectivity of mouse somatosensory and prefrontal cortex examined with trans-synaptic tracing. *Nature Neuroscience*, *18*(11), 1687–1697. https://doi.org/10.1038/nn.4131
53. Kim, E. J., Juavinett, A. L., Kyubwa, E. M., Jacobs, M. W., & Callaway, E. M. (2015). Three Types of Cortical Layer 5 Neurons That Differ in Brain-wide Connectivity and Function. *Neuron*, *88*(6), 1253–1267. https://doi.org/10.1016/j.neuron.2015.11.002

Chapter 1. Functional Interlaminar Connectivity in Mouse Primary Visual Cortex

Abstract

One of the defining characteristics of the cerebral cortex is its organization into layers, each distinguishable by a unique composition of cell types and together representing a fundamental component of sensory information-processing. Most of what we know about functional interlaminar connectivity is from paired recordings in slice preparations which, due to cut axons, dramatically underestimate the rate of interlaminar connections. This leaves us with an incomplete understanding of how cortical circuits transform sensory information across layers. In this study, we use an optogenetic approach to bypass the issue of cut axons and comprehensively characterize relative synaptic input strength to 3 inhibitory cell subtypes in cortical layers 2/3, 4, 5, and 6. We used transgenic mouse lines and viral vectors to restrict Channelrhodopsin-2 (ChR2) expression to excitatory cell populations within a single layer and selectively label cells of somatostatin (Sst)-, parvalbumin (Pvalb)-, or vasoactive intestinal polypeptide (Vip)-expressing inhibitory subtypes in mouse primary visual cortex. We then pair optogenetic stimulation of axon terminals (including live, cut axons) with ex vivo intracellular recordings in excitatory and inhibitory cells across cortical layers and measure the monosynaptic input strength from the stimulated cell population to the recorded cells. This enables us to compare postsynaptic responses within and between inhibitory subtypes and cells recorded in different layers. We can thereby quantify the proportion of excitatory input from each cortical layer to each inhibitory subpopulation within and between layers. Our data and analyses suggest input strength from a given layer to a particular inhibitory cell type depends strongly on both the input layer, the laminar location and the inhibitory subtype of the recipient cell. We also find that functional

input strength differs between excitatory cells and inhibitory subpopulations and examine the degree to which each layer provides input to excitatory versus inhibitory cells. Together, our results provide a more complete picture of the relative distribution of excitatory synaptic input from each layer to distinct cell subpopulations across layers within a single cortical region.

Introduction

A comprehensive understanding of the circuit organization and connectivity between cortical cell types is needed to gain insight into cortical function and transformation of sensory information. Anatomical reconstructions of neurons in cat visual cortex show that cells in each layer make precise, specific connections with cells in other cortical layers[1,2] and that each layer can be distinguished by a unique composition of cell types. These findings formed the basis for a canonical cortical microcircuit governing sensory information flow, in which sensory input is relayed through thalamus LGN to L4 → L2/3 → L5/6 which in turn provide recurrent input back to L4 and output to other cortical and subcortical regions[3–5]. Although some previous research supports the existence of a canonical, feedforward excitatory cortical circuit excitatory cell populations provide functional input to multiple layers[6]. Thus, the canonical cortical circuit as traditionally understood does not capture the inherent complexity of interlaminar circuitry considered to be the primary output layer of the cortex. Moreover, the construction of this excitatory, feedforward cortical circuit from anatomical data rests on the assumption that dendritic overlap is directly proportional to the number of synaptic contacts made between neurons. Because dendritic overlap does not necessarily reflect functional connectivity strength[7]—that is, synaptic strength varies greatly by cell type--the presence of functional synapses can only be captured/validated through electrophysiological recordings.

Most of what we know about functional interlaminar connectivity is from paired recordings in slice[6]. While electrophysiology is the most precise way of detecting and measuring functional connectivity between cells, paired recordings dramatically underestimate the rate of interlaminar connections between cortical cells due to cut axons[8]. Moreover, due to the vast diversity in dendritic branching across cortical cell types and that a large proportion of synaptic terminals are several hundred microns away from the soma[8] the fraction of potential cut synapses varies by depth, vertical distance between cells, and cell type. This bias in the likelihood of dendritic/axonal truncation during slicing has dramatic implications for experiments in cortical tissue slices where pre- and postsynaptic cells are several hundred microns apart. Thus, previous studies provide an incomplete understanding of how and to what extent sensory information is relayed within a particular cortical region. Recent advances in technology have enabled the targeted identification of distinct cell populations, which in turn have revealed unique projection patterns, transcriptomic and electrophysiological characteristics[9,10]. Moreover, the relative strength of these functional interlaminar connections is not well understood. Functional role of individual neurons is dictated by its synaptic inputs within cortical circuitry; therefore, understanding the laminar distribution of input to each individual cell type is necessary to gain a complete understanding of the functional role of each neuron type.

In this foundational study we use an optogenetic approach to bypass the issue of cut axons and comprehensively characterize relative synaptic input strength between layers 2/3, 4, 5, and 6. We use a combination of transgenic mouse lines and viral vectors to restrict Channelrhodopsin-2 (ChR2) expression to excitatory cells within a single cortical layer. We then pair optogenetic stimulation with intracellular patch-clamp recordings in cells across all cortical layers to measure the monosynaptic input strength from the stimulated cell population to the recorded cell[11]. We thereby compare the relative peak amplitude and charge transfer between cells recorded in each layer and quantify the proportion of total input from a single cortical layer to other layers. Broadly, we find that interlaminar input strength to excitatory neurons varies by laminar location. Consistent with previous research, L4--the primary layer receiving sensory input relayed from thalamus—provides most of its input to L2/3, and L2/3 provides strong input both within L2/3 and to L5. Our results also suggest that relative interlaminar input strength varies by cell type. For example, we find that while subcortically-projecting neurons in L5 primarily provide input to other cells in L5, cortically-projecting neurons provide most of their input to L2/3. Interestingly, inputs from L6 subcortically-projecting neurons are evenly distributed between L4, L5, and L6. Together, our results provide a more complete picture of the relative distribution of synaptic input from each layer to other layer within a single cortical region.

Results

Experimental Strategy

We restricted ChR2 expression to a specific cortical layer in V1 using Cre mouse lines, where Cre recombinase is expressed in a specific population of excitatory cells within L2/3 (SepW1^{Cre}), L4 (Scnn1a^{Cre} and Nr5a1^{Cre}), L5 (Tlx3^{Cre} and Npr3^{Cre}), and L6 (Ntsr1^{Cre}) (Figure 1.1A). To restrict functional connections to V1, we used a viral vector-based approach and injected an AAV containing Cre-dependent ChR2 (Figure 1.1B). This way, while ChR2 expression is restricted to cells within a single cortical layer, ChR2 is expressed on these cells' dendritic processes which extend to other layers. We then conducted in vitro slice recordings to probe functional connections (Figure 1.1C-D). After waiting 3-4 weeks for the virus to express in a particular layer, we conducted whole-cell recordings paired with full-field optogenetic stimulation to evoke neurotransmitter release at axon terminals of the ChR2-expressing population[11]. We recorded postsynaptic responses in the presence of TTX and 4-AP to isolate monosynaptic connections (see Methods). Excitatory input from cortical L2/3 was assessed using the SepW1-Cre mouse line, which expresses Cre in all L2/3 excitatory pyramidal cells Previous research suggests that excitatory input from L2/3 is largely restricted to L2/3 and to L5. Excitatory pyramidal neurons in L2/3 receive strong excitatory input from middle cortical layers [12]. Stimulating L6 CT cells inhibits neurons in L4 but powerfully excites neurons in L5a[13].

To quantify interlaminar excitatory input from each postsynaptic recording, responses were baseline-subtracted and averaged across trials. All recordings were conducted in voltage-clamp using a Cesium-based internal solution and containing biocytin to verify recorded cells' laminar location post-hoc.

We quantified functional input strength using both trial-averaged peak response amplitude (maximum negative value of the EPSC) and total integrated current/charge transfer (EPSQ)[14]. The window in which EPSQ was calculated was determined by the time at which the average EPSC trace fell below 10% of the peak amplitude (Figure 1.2A). Cells containing ChR2 were readily distinguished by their location in Cre-expressing layer (i.e. the mouse line in which the experiment was conducted), as well as their short onset latency and low variability in response shape (Figure 1.2B, see Methods). To quantify each cell's response, we used 2 metrics: the charge transfer or integrated current (EPSQ) and the peak amplitude. To directly compare responses across trials, we subtracted the average leak current pre-stimulus from the post-stimulus response for each trial, effectively bringing the baseline to 0 to align the traces. By

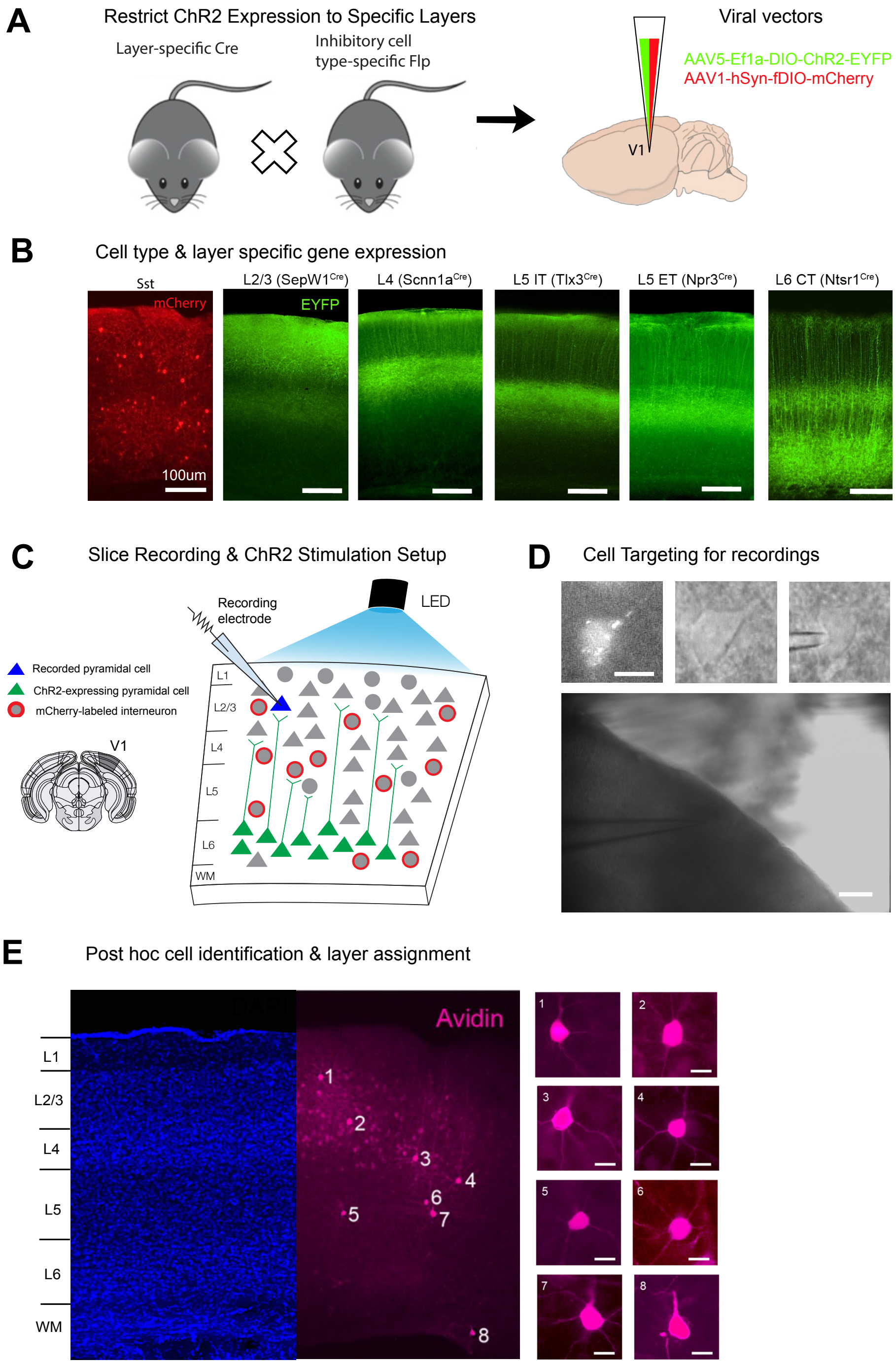

Figure 1.1 Experimental Strategy. (A) Mice expressing layer-specific Cre were crossed to inhibitory neuron subpopulation-specific Flp. Following genotyping, AAV mixture of Cre-dependent ChR2-EYFP and Flp-dependent mCherry was injected into V1. (B). After 3 weeks of virus incubation, resultant interneuron population (Sst in this example)-specific mCherry and layer-specific ChR2 expression in 5 different mouse lines used. (C) Slice Recording and LED stimulation setup. (D) mCherry fluorescence (first panel, top)- and DIC microscopy-based cell targeting for intracellular recordings. Top 3 images in panel show Sst+ cell targeted; scale bar is 10um. Bottom image: image of pipette in slice during recording; scale bar is 100um. (E) Coronal section showing post-hoc DAPI stain (left) used to define layer boundaries and avidin stain (right) showing biocytin-filled cells in magenta. Zoomed images on far left show close-ups of filled cells. Scale bars represent 100um (hemisection images) and 10um (zoomed images).

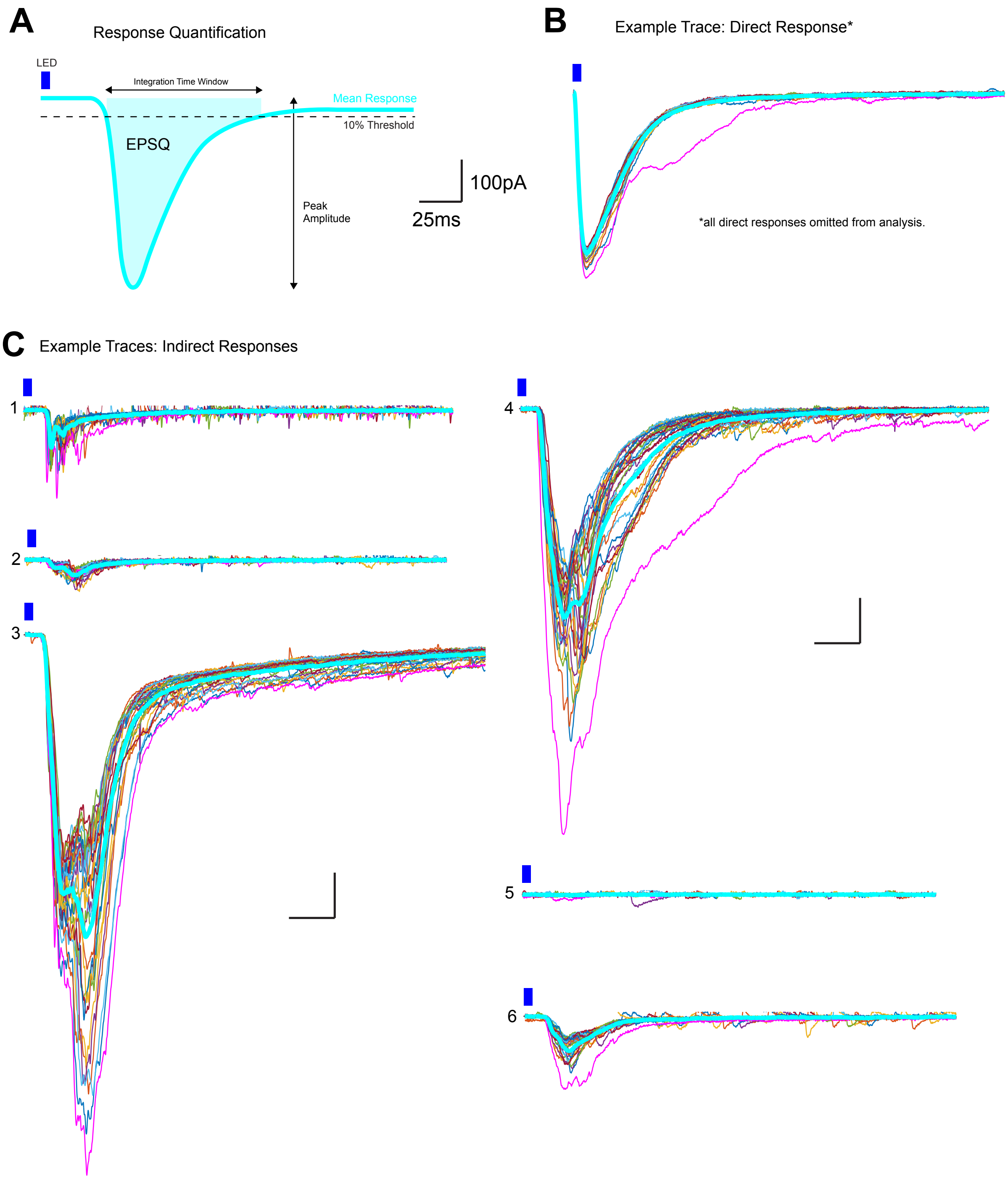

*all direct responses omitted from analysis.

Figure 1.2. EPSC response quantification and example recording traces. Thick cyan traces denote averaged response across trials. Shaded cyan region denotes time window in which current was integrated to calculate EPSQ in subsequent analyses; the boundaries of the time window correspond to the time points at which the average recorded current was >10% of peak amplitude. 10% threshold denoted with dotted line in (A). Dark blue box corresponds to LED stimulus onset (5ms). (B, C). Example traces shown are from different cells all recorded in the same slice from an Scnn1a^{Cre} mouse (all responses are monosynaptic input from L4 pyramidal neurons). (B), Example recorded direct response to ChR2 activation observed in a L4 pyramidal neuron. Note the immediate response onset and low variability in response shape, characteristic of direct responses. (C), example indirect responses from 6 cells. 1, L6 pyramidal cell; 2, L6 Sst cell; 3, L5 Sst cell; 4, L5 pyramidal cell; 5, L6 Sst cell (no response); 6, L6 Sst cell.

averaging traces across trials, the effect of spontaneous currents is compensated for, and we can see whether a consistent, detectable evoked response occurred. Recorded cells exhibited a wide variety of response shapes and amplitudes, including some where no response was detected (Figure 1.2C). In subsequent analyses, both methods of quantification revealed similar results; see Table 1.S4-S5 for statistical comparisons of populations for both metrics.

General patterns of functional input distribution

Before assigning recorded cells to their layers, we first wanted to determine whether postsynaptic input strength exhibited a consistent relationship with recorded depth in cortex. By plotting each cell's peak amplitude against normalized cortical depth while distinguishing between input population and recorded cell type, clear trends begin to emerge. We see that excitatory neurons provide substantial input to all cell types within L2/3, especially inhibitory cells. Of the input provided to each inhibitory subtype from L2/3, the vast majority of Sst, Pvalb, and Vip cells receiving L2/3 input were themselves in upper layers. L2/3's input to pyramidal cells appeared more evenly spread across layers (Figure 1.3A). A similar trend was observed for input from L4 (Figure 1.3B), though input to pyramidal neurons appeared more concentrated to very superficial layers. Input to inhibitory subtypes appeared broadly scattered to upper layers. Strikingly, input from L5 IT and ET subpopulations differed dramatically (Figure 1.3C-D); superficial pyramidal neurons received more input from L5 IT while L5 ET sent its input almost exclusively to deeper layers. This pattern was generally conserved across inhibitory subtypes, where L5 IT provided input to all subtypes across all layers, with input to Sst neurons focused on upper layers, while L5 ET cells mostly provided input to Sst and Pvalb neurons in deeper layers.

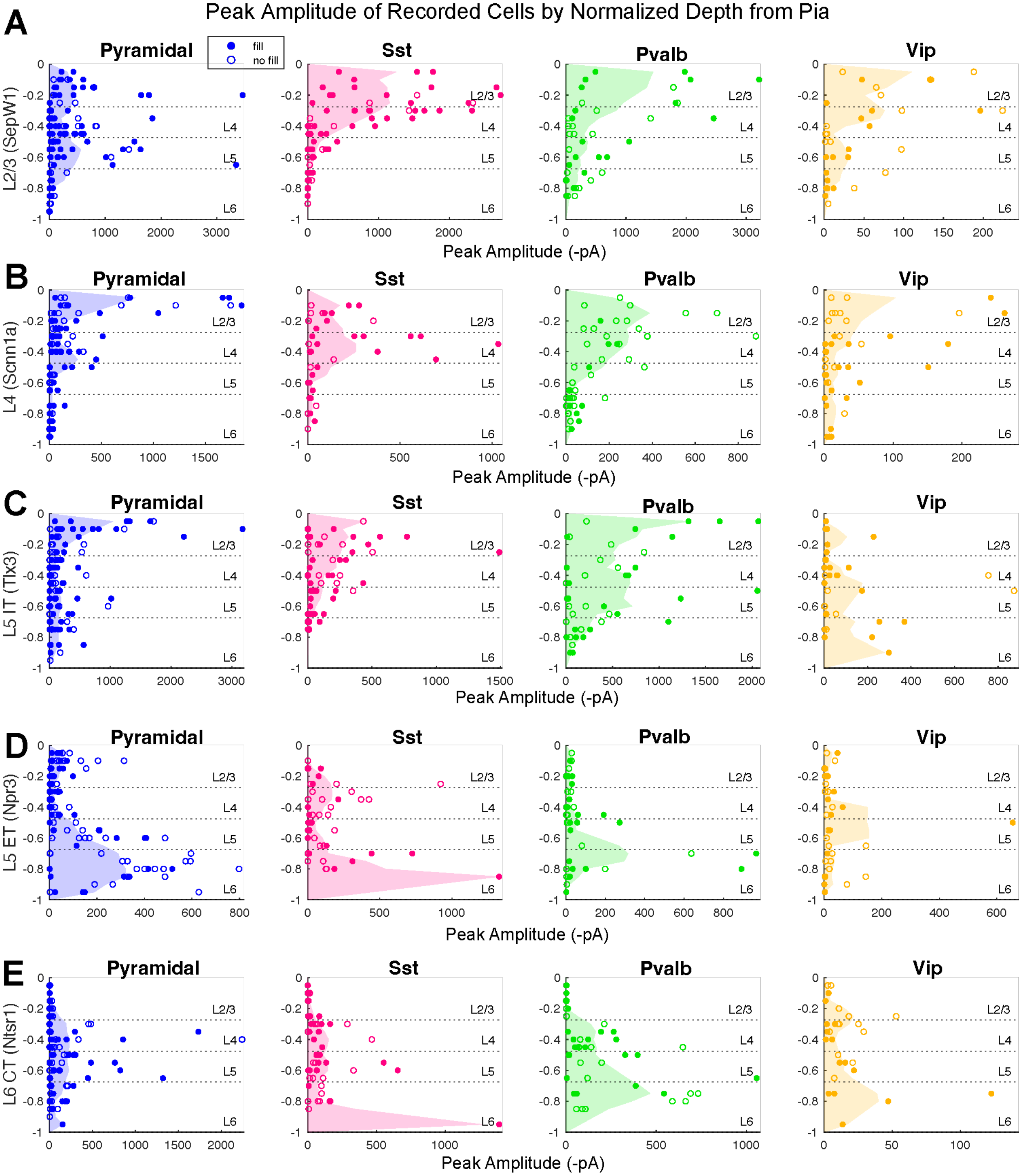

Figure 1.3. Interlaminar input by recorded cell depth. Peak Amplitude (left column) distributions by normalized depth from top of L2/3 to bottom of L6. Y axis shows normalized depth of each recorded cell. Columns and color of dots denotes cell type recorded, ChR2-expressing layer (Cre line) represented in each row: (A) shows input from L2/3, (B), input from L4, (C), input from L5 IT, (D), input from L5 ET, and E, input from L6 CT cells. Shaded area represents smoothed average responses recorded at each depth. Layer boundaries are approximate, estimated from recording depth.

L6 CT neurons appeared to provide input to all cell types, concentrated mostly in middle layers but scattered throughout with no clear preference for superficial vs. deep layers (Figure 1.3E).

Recorded cells were next identified and assigned as belonging to a particular cortical layer from using biocytin in our internal recording solution for post-hoc reconstruction and using a DAPI stain to define layer boundaries (Figure 1.1E, see Methods). We then asked whether input from each layer provided different amounts of synaptic input to each recorded cell type and whether this input distribution was also layer-dependent. Plotting each recorded cell's EPSC peak amplitude as a function of layer and cell type revealed that indeed, the amount of synaptic input received from a particular layer-restricted population was wholly dependent on both the presynaptic population as well as the post-synaptic cell type and laminar location. Consistent with previous work and with the original canonical circuit model, L2/3 IT pyramidals provide substantial input to L5; we also observed significant input to pyramidal neurons within L2/3 and L4, with very little input pyramidals in L6 (Figure 1.4A). L2/3 IT cells' input to inhibitory subpopulations consisted primarily of Sst neurons in upper layers and Pvalb neurons in L2/3. As can be seen from the axis scaling in the rightmost column of Figure 1.4, responses in Vip neurons were significantly smaller than EPSCs recorded in the other 3 cell types, suggesting that these cells receive very little synaptic input from the ChR2-expressing pyramidal cell populations. We hypothesize that instead, these populations likely receive more input from more distal cortical regions[15] interneurons, as has been suggested previously[16]; Vip neurons are thought to regulate feedback inhibition in cortex through reciprocal inhibition of Martinotti-type Sst-expressing neurons.

Also consistent with the original canonical circuit model, L4 neurons provide most of their input to pyramidal neurons in L2/3 (Figure 1.4B). Interestingly, we also see that this same

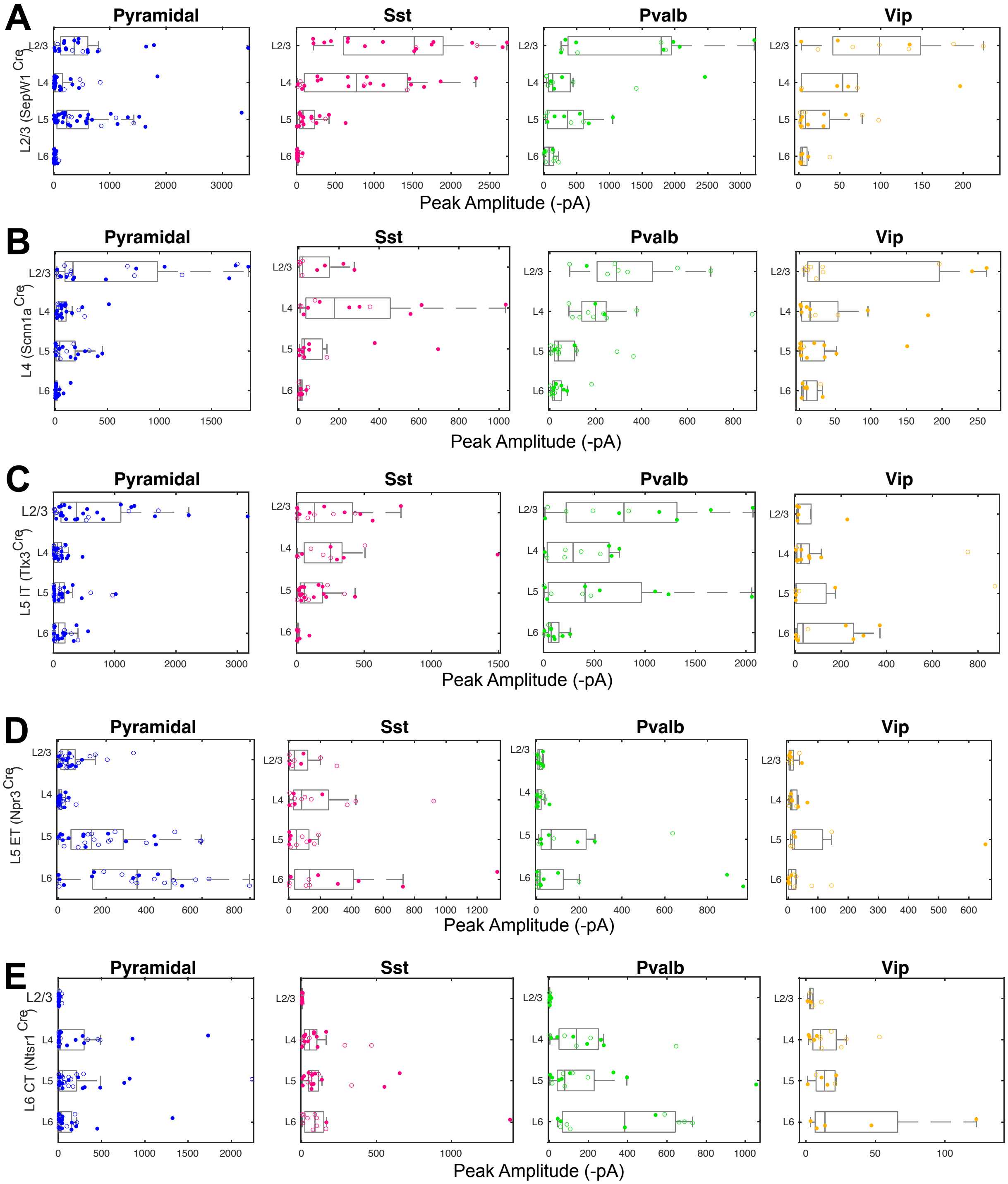

Figure 1.4. Peak Amplitude distributions by assigned cell layer. Statistical comparisons not displayed for clarity; see Table 1.S6 for all pairwise comparisons and associated p-values. (a-b) Responses to ChR2 stimulation in L2/3 (n = 103 cells). (c-d) Responses to ChR2 stimulation in L4 (n = 39 cells). (e-f) Responses to ChR2 stimulation in L5 IT cells (n = 95). (g-h) Responses to ChR2 stimulation in L5 ET cells (n = 85). (i-j) Responses to ChR2 stimulation in L6 CT cells (n = 85).

pyramidal population provides a large amount of input to L2/3 Pvalb neurons and Sst neurons in L4. From L5 and L6, the original model proposes that some information gets routed extracortically (the deeper layers serve as the cortical output layers), with some feedback that gets sent back to L2/3. Our results are somewhat consistent with this model in that for the L5 IT population (Figure 1.4C)—cells that project within telencephalon—send most of their input back to L2/3 while L5 ET cells that project extratelencephalically (Figure 1.4D) send most of their intracortical input within deeper layers with very little input to any cells outside of L5/6. EPSCs were generally smaller in amplitude for inputs from L5 ET vs IT populations, consistent with the idea that the former send synaptic input primarily extracortically. However, given previous work showing that L5 IT neurons provide more input to L5 ET neurons than L5 ET neurons to themselves[7], we expected L5 IT neurons to provide substantial input to other L5 pyramidal cells which was not the case. In short, the L5 IT → L2/3 connection appears stronger than previously described in the literature but could also be plausibly be explained by our experimental setup which enables detection of more distal dendritic contacts versus previous studies in paired recordings which would have likely severed many L5 → L2/3 connections[8].

Like the L5 ET population, L6 CT neurons are perceived as an "output" center of the cortex in that they project extracortically and exert a suppressive effect on superficial cortical layers[17–19] through recruitment of interlaminar Pvalb neurons. We therefore expected to see strong input to L6 Pvalb neurons and indeed observed large responses in this cell type (Figure 1.4E). Inputs to both pyramidal neurons and Sst interneurons appeared sparse and scattered across all layers except L2/3.

The original canonical circuit model makes no mention of inhibitory cells, instead focusing exclusively on excitatory FF interlaminar connectivity. Despite the lack of concrete modifications since its initial conception, a large body of evidence clearly demonstrates the existence of inhibitory interlaminar circuits[20,21]. In light of this, one of our primary objectives in this project was to definitively characterize and quantify these functional interlaminar connections between defined excitatory and inhibitory subpopulations. We observe clear interlaminar input to each inhibitory subtype recorded, especially Pvalb neurons. While L2/3, L4, and L6 CT pyramidal populations primarily synapse onto Sst neurons in the same layer, L5 IT & ET pyramidal cells provide input to Sst neurons outside of L5—L5 IT sends 80% of its input to Sst neurons to those in upper layers, and L5 ET sends 61% of its Sst inputs to those in L6 (Figure 1.5B). This was also observed for inputs to Pvalb neurons, where L5 IT pyramidals send 52% of their Pvalb input to those in L2/3 while L5 ET pyramidals send 52% of their Pvalb input to L6. Interestingly, with the exception of L6 CT neurons, relative functional input to pyramidal neurons largely mirrored input to Pvalb neurons, consistent with the idea that they may receive correlated information and form precisely organized circuits with each other[22–24]. The interlaminar connectivity patterns between inhibitory subtypes was heterogeneous, though a few commonalities existed: L2/3 pyramidals provided input to all 3 types within L2/3, and L5 IT neurons provided extensive input to all 3 types outside of L5.

Accounting for response variability

Although we found that the LED light intensity had no significant effect on response amplitude (Figure 1.S4), we nevertheless wanted to determine whether variability in ChR2 expression across slices may have influenced our results. In other words, could observed differences in peak amplitude across layers be explained by variability in ChR2 expression levels across slices, rather than differences in input strength? To this end, we used a linear mixed-

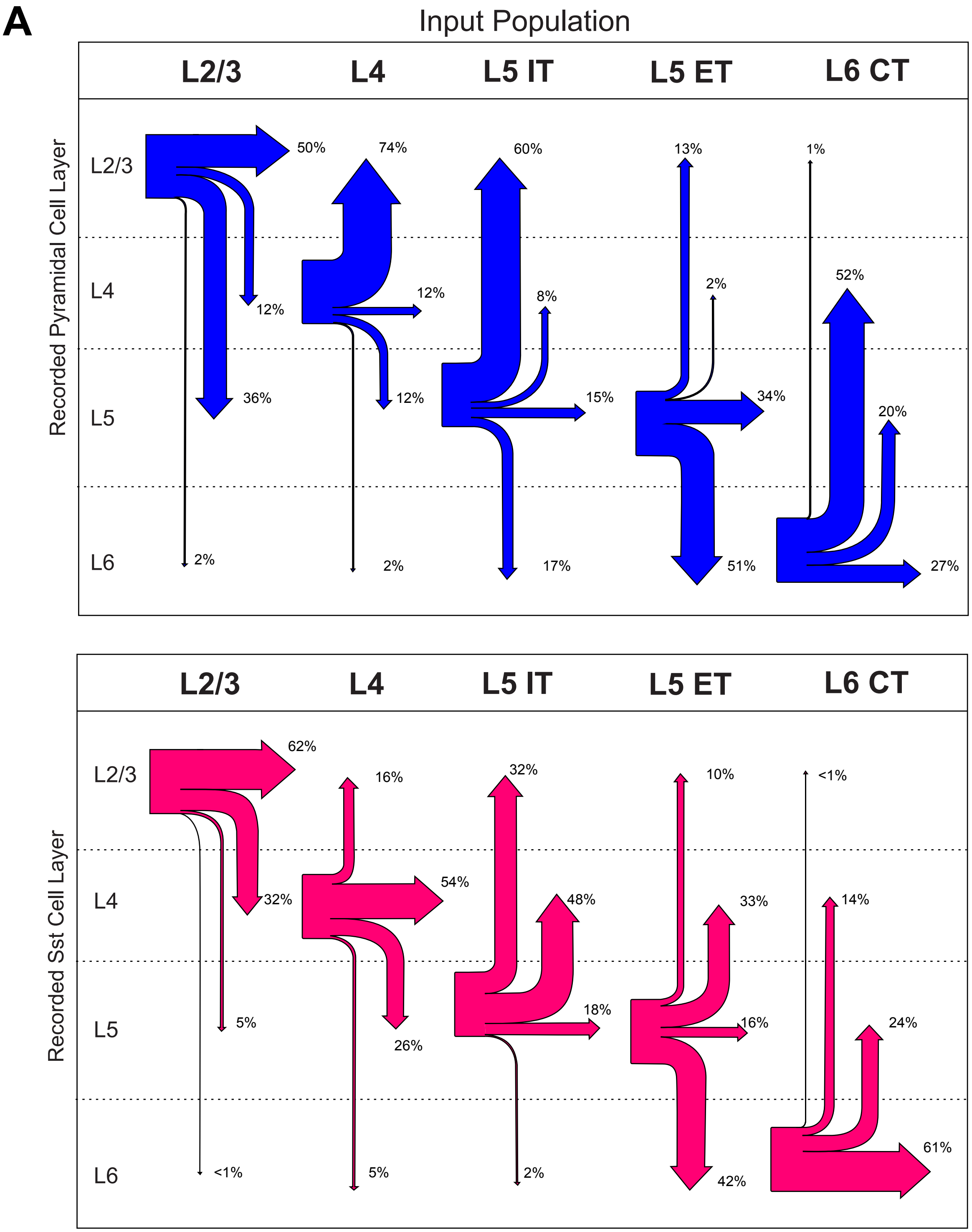

Figure 1.5. Summary of inputs to pyramidal and Sst-expressing neurons. Relative Interlaminar Distribution to pyramidal (A) and Sst (B) cells from each layer-specific input cell population. Values expressed as percent of total input to recorded cells in each layer from the ChR2-expressing layer. For each cell type, Percentages were calculated for each ChR2-expressing (input) cell population by taking the mean EPSQ of recorded cells in each layer and dividing by the sum of the mean epsq of cells of that subtype across all layers. A, Total inputs to pyramidal cells from L2/3 (n = 122 cells), L4 (n = 95), L5 IT (n = 109), L5 ET (n = 105), L6 (n = 109). B, Total inputs to Sst cells from L2/3 (n = 73 cells), L4 (n = 42), L5 IT (n = 57), L5 ET (n = 44), L6 (n = 56).

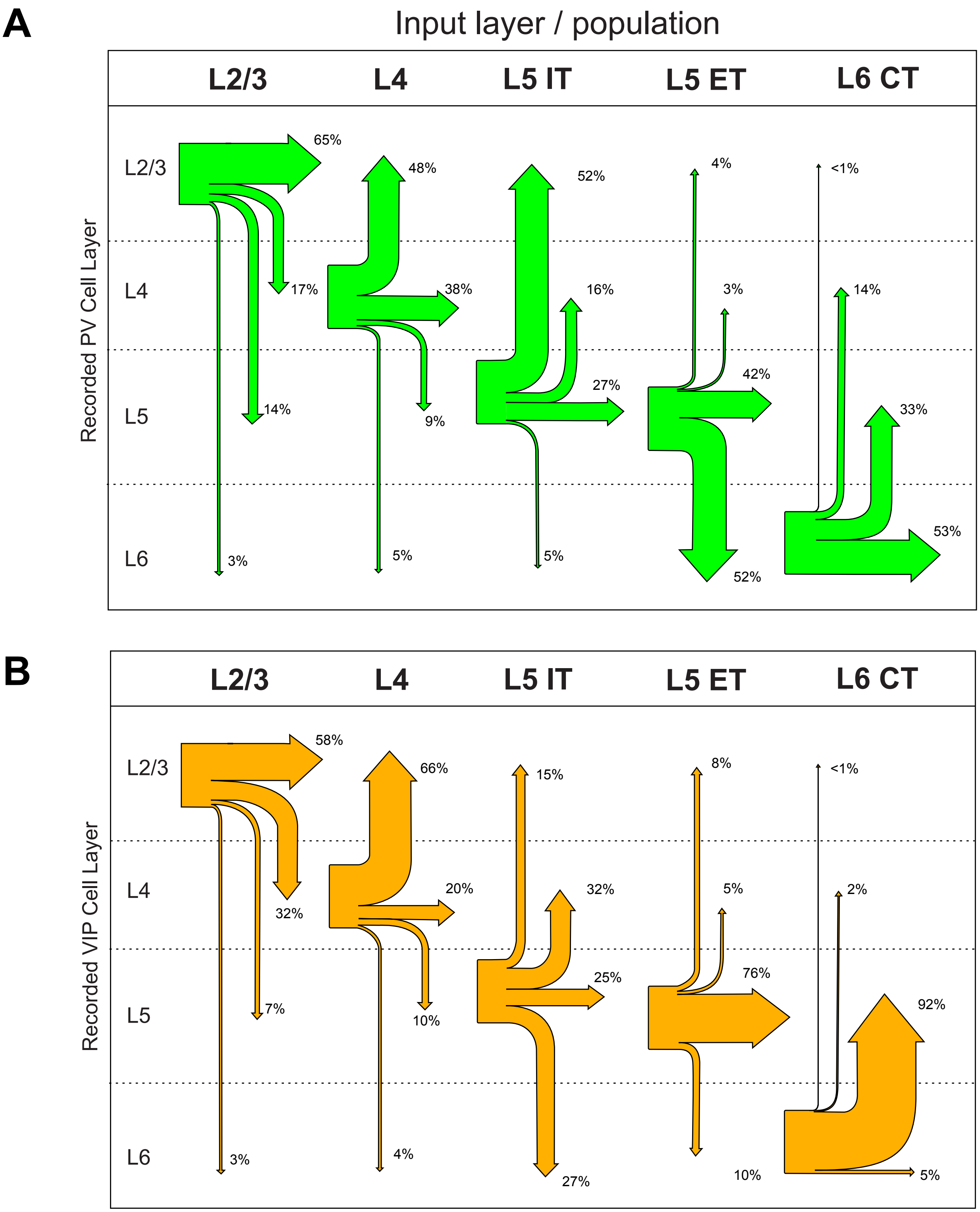

Figure 1.6. Summary of inputs to Pvalb- and Vip-expressing neurons. Same as in Figure 1.5; relative distribution to Pvalb- (A) and Vip- (B) cells from each layer-specific input cell population. Total inputs to PV cells from L2/3 (n = 42 cells), L4 (n = 47), L5 IT (n = 42), L5 ET (n = 44), L6 (n = 45). D, Total inputs to VIP cells from L2/3 (n = 35 cells), L4 (n = 41), L5 IT (n = 33), L5 ET (n = 36), L6 (n = 30). See Table 1.X for n values for cells of each subtype recorded in each layer.

effects model (LMEM) to determine whether differences in synaptic input strength to each recorded cell layer were still present after accounting for inherent slice-to-slice variability in ChR2 expression (see Methods). We found that overall, accounting for variability in ChR2 expressing did not affect our findings; synaptic input strength was highly dependent on the recorded cell layer, the input population (and layer), and the recorded cell type. See Figure 1.S9 for model results.

To gain a more holistic perspective on how the excitatory interlaminar circuit appears and to compare it more directly with the traditional canonical model, we calculated the overall distribution of synaptic input from each layer-specific ChR2-expressing population to the 4 recorded cell types in each layer by dividing the sum of mean EPSQs across layers by the mean EPSQ in each layer across all cells of a given type. We were thereby able to visualize the relative amount of interlaminar synaptic input provided to each cell type as illustrated in Figures 1.5 and 1.6. For pyramidal-to-pyramidal inputs, as previously described and in accordance with the traditional model, L4 and L5 IT provide very strong inputs to L2/3; the L4 → L2/3 connection is considered FF and L5 IT → L2/3 is FB. In contrast to the canonical model, however, L2/3 actually provides more input within L2/3 vs. down to L5 (Figure 1.5A). L6 CT sends more input to L4 pyramidal neurons than to those in any other layer, consistent with previous work demonstrating prominent axon termination patterns in this layer[25].

Discussion

The cerebral cortex's organization into six distinct layers across all mammalian species suggests a deep evolutionary significance. Characterizing the function of this unique feature is essential for us understand how cognition arises from functional cortical connections. Fine-scale specificity in interlaminar connections between cells suggest that these populations play specific functional roles, and similar findings across multiple cortical areas imply a common organizational mechanism for processing information. These ideas have given rise the appealing notion of a simple, excitatory “canonical cortical circuit” motif underlying sensory information processing. Although this theory continues to predominate the literature, the central structure of the canonical cortical circuit is based on experimental findings containing critical shortcomings. In particular, severed axonal connections in *ex vivo* paired intracellular recordings preclude accurate characterization of interlaminar functional connectivity. Understanding the relative strength of these connections is essential to determine the extent to which functional connectivity strength can be inferred from dendritic overlap between cells, to better understand the unique computational role of each cortical layer, and ultimately to elucidate the hierarchical mechanisms underlying cortical function.

Using a combination of transgenic mouse lines exhibiting layer-specific Cre expression, electrophysiological recordings, optogenetic manipulations, and morphological reconstructions, we have comprehensively characterized relative functional input strength from specific cell populations in a particular cortical layer to other cortical layers. Unlike past work that has largely focused on microcircuits within a single layer or on long-range inputs to cortical populations, we have quantified the relative distribution of input to other layers and the cell types that receive that input within a single cortical region. We conclude that despite general pathways aligning with prior documented connections between layers, these connections depend on the identity of the cell providing the input and the identity of the receiving cell. Our results suggest a more complex, nuanced organization of interlaminar cortical circuitry and highlight the need to more closely re-examine the traditional notion of the canonical cortical circuit.

Moreover, one of the most striking findings in our data, that can be immediately gleaned from the boxplots (Figure 1.4) and from Tables 1.S4, is the immense diversity in response amplitudes. If input from the stimulated population were somewhat uniform, as might be expected if a true feedforward canonical circuit were to exist, we would anticipate variability in input strength to be relatively consistent across recorded cells of a particular type. However, the prominent variability we see in response amplitude and EPSQ within cell types—even those recorded in the same layer of the same slice (Figure 1.S5)—indicate that input from a given layer-specific excitatory subpopulation is highly variable. We hypothesize that in the case of Sst and Pvalb neurons, which have been transcriptomically well-characterized using Patchseq[26,27] input from a given layer may be subtype-dependent. In other words, excitatory subpopulations within a specific cortical layer may only provide synaptic input onto specific subtypes of these interneuron populations.

An alternative explanation, especially in the case of pyramidal neurons, it is possible that the strength of input to a given cell is dependent on the functional subnetwork to which that cell belongs. Increasing evidence suggests excitatory synaptic strength is highly concentrated, and that pyramidal cells with similar tuning preferences form fine-scale functional subnetworks within L2/3[28] leading to a highly skewed distribution of synaptic connectivity strength, where a few strong synapses dominate over the majority of weak synapses. If input from entire layer-specific excitatory subpopulation is activated as was the case in our experiments, one might expect the resulting postsynaptic response to be highly variable and dependent on the extent to which the recorded cell's functional subnetwork was activated.

To what extent can inputs to recorded cell types be compared with each other? Mean EPSQs for each cell population & layer were then multiplied by population sizes below to estimate relative distribution of synaptic output from layer-specific Cre population to each cell population within each V1 layer. After accounting for each cell type's relative population size, density within layer, and layer thickness (see Methods), we found that of all measured synaptic output from each excitatory population, the majority of synaptic output was to other pyramidal cells in all other layers (Figure 1.S2).

While we made every effort to ensure consistency across recordings and effective experimental controls, our results do contain caveats. For example, could the variability in response strength seen between layers be explained by variability in the amount of ChR2 in the slice? If many cells in a particular layer with large responses are recorded in a slice with unusually high ChR2 expression, it's possible that this would bias our results in favor of inputs to cells in the recorded layer(s). To determine whether differences in responses truly reflected the amount of input received from the stimulated layer rather than variability in ChR2 expression across slices, we recorded from at least 2 cells in at least 2 different layers in each cortical slice, recorded cells were restricted to regions with maximal ChR2 expression, and varied the order in which each layer was recorded. By recording from multiple cells and multiple layers in each slice, we could compare the relative variability in response amplitude between cells recorded in the same slice versus cells in different slices (Figure 1.S5). We found that variability in response amplitude between recorded cells within slice was comparable to variability across slices, indicating that the differences we see in interlaminar input strength cannot be due to differences in ChR2 expression alone.

In addition to accounting for variation in ChR2 expression, we also used post-hoc histological stains to verify the identity and location of recorded cells. As previously mentioned, cells were assigned to a particular cortical layer based on their location (identified via biocytin fill) relative to layer boundaries defined by DAPI staining in each slice. All cells were assigned a single layer including those close to the laminar borders; is therefore possible that a small proportion of cells' assigned layer was incorrect. Lastly, although excitatory pyramidal cells were targeted in recordings based on shape and biocytin-filled recorded cells revealed to be inhibitory were omitted from analysis, it is possible that a small number of unfilled cells were non-pyramidal because their morphological characteristics could not be verified.

This work forms the foundation for understanding the function of cortical layers common to all mammalian species. To fully capture the extent to which functional connectivity can be inferred from anatomical reconstructions, future studies in mice should explore the relationship between dendritic overlap and synaptic connection strength between cells Additional work is needed to understand how interlaminar connectivity relates to cognition on a broader scale--that is, how does this organization of functional connections transform sensory information and affect behavior? The connections probed in this study are excitatory, and only inputs to pyramidal cells were investigated here. Moreover, whether the distribution of inputs to inhibitory cells is similar remains to be seen. Additional use of cell-type specific Cre lines will enable the characterization of interlaminar inputs to these cell types. In addition, with the advent of Patchseq and advanced transcriptomic analyses, we will be better able to determine whether input to a specific cell type within each cortical layer is transcriptomic subtype-dependent.

Methods

AAV Injections

In accordance with approved IACUC protocol, transgenic mice aged p22-p32 were injected with 100nL of either 1:1 HBSS : AAV8-Ef1a-ChR2-EYFP dilution or a 2:2:1 mixture of

HBSS : AAV8-Ef1a-ChR2-EYFP : AAV1-hSyn-FlpO-mCherry used for separate experiments into V1 (from lambda: -2.55mm ML, .6mm AP) at a pial depth of -.3mm. Recordings were conducted at least 21 days post-injection to allow for adequate viral incubation and ChR2 expression.

Slice Preparation

Mice aged p43-p85 were anesthetized using isoflurane. 350um-thick coronal slices were sectioned using a Leica VT1200 (Leica Biosystems) vibratome in ice cold, oxygenated sucrose solution (in mM): 2.5 KCl, 1.25 NaH_2PO_4•H_2O, 10 $MgSO_4$•$7H_2O$, .5 $CaCl_2$•$2H_2O$, 11 Glucose, 234 Sucrose (Sigma-Aldrich). Slices were immediately transferred to a holding chamber holding ACSF (in mM): 2.5 KCl, 10 Glucose, 126 NaCl, 1.25 NaH_2PO_4•H_2O, 10$MgSO_4$•$7H_2O$, 2 $CaCl_2$•$2H_2O$ and incubated for at least 1 hour at 37˚C, then held at room temperature until used in experiments.

Electrophysiological Recordings

Borosilicate glass pipettes (Sutter Instruments) with 2-4MΩ resistance were pulled using programs in a Sutter Instruments p-97 puller and filled with a 280mOsm (pH ~7.3) Cs-Gluconate based internal solution containing (in mM): 130 CsOH (50% wt), 130 Gluconic Acid (50% wt), 10 HEPES, 5 TEA-Cl, 12 Na-phosphocreatine, .2 EGTA and .1% Biocytin. Voltage Clamp recordings were conducted at an uncorrected holding potential of -70mV (-83mV corrected for liquid junction potential). Series Resistance was not compensated. 1uM TTX and 10 mM 4-AP (Sigma-Aldrich) were added to the recording bath ACSF and continuously recirculated at 34˚C.

V1 was visually identified in each slice using a 4x objective (Olympus). Cells were targeted for recordings by shape and size through a 60x microscope objective. ChR2 expression in slices was validated before each recording session in double transgenic Cre(+) x SomFlp(+) mice where Flp-dependent mCherry and Cre-dependent ChR2/EYFP were co-injected (55/65 mice). Cells with an $R_{access} > 30M\Omega$ and $R_{access} < 10\%$ of R_{input} were excluded from analysis, as well as cells with a holding current <-150pA and those in which <20 stable trials were recorded (see Criteria for Omission for further details).

Optogenetic Stimulation

Cells were stimulated using full-field LED stimulation (16 mW) delivered through a fixed cannula approx. 1cm from the slice. The cannula was oriented perpendicularly to the pial surface of the region of V1 with maximal ChR2 expression, L2/3 oriented closest to the cannula and L6 furthest away. Light intensity was measured using a photodetector and the illumination intensity drop-off was determined to be <10% across the cortical depth (Figure 1.X). 5ms LED stimuli were triggered with a TTL pulse in 30 x 5s recording sweeps while post-synaptic responses were recorded from cortical neurons in pClamp (Molecular Devices).

Direct responses to photostimulation—recordings from cells containing ChR2—were identified by their decreased latency (<5ms vs ~10ms for indirect responses, see Table #), large response amplitude, and low variability in response shape/amplitude across trials, and location in ChR2-expressing layer. Direct responses were omitted from analysis (see Figure 1.2).

Criteria for Omission

Cells omitted from analysis fell into one of four categories. (1) A direct response was detected (the cell expressed ChR2, see Optogenetic Stimulation in Methods); (2) no responses >10pA were recorded in any cells in slice (usually corresponding to very little ChR2 expression as revealed in post-hoc IHC); (3) insufficient data (<20 trials) were obtained to adequately characterize response, see prev. paragraph for cell health criteria; or (4) the cell was located medial or lateral of the region of the slice containing ChR2 as revealed in post-hoc IHC. Biocytin-filled, recorded cells that were not excitatory were also omitted from analysis (5/715 cells).

Statistical Analysis

Data were analyzed using custom software written in MATLAB (MathWorks, 2018b). Sweeps were first baseline-subtracted; baseline window was 50ms immediately preceding LED stimulus onset. Cells were classified as NR if the average R was <10pA across trials. Slices in which no responses were observed, cells did not span multiple cortical layers, or <3 cell recordings were made were excluded from analysis. Peak Amplitude was recorded as the maximum (negative) deflection from baseline averaged over trials, and EPSQ was calculated by integrating recorded current (EPSC) over the time period in which current exceeded 10% of its peak amplitude. Due to the large variability in response shape, a fixed analysis time window for all cells would result in the large responses getting cut off and calculated EPSQs for small/brief responses artificially shrunk. To systematically adjust the time window in EPSQ calculations, we found the average (negative) peak current response across all 30 trials and defined boundaries of the analysis window by the period during which the evoked current was greater than 10% of the max—and the end of the window is marked by the return to 90% of its baseline value (0).

Distributions of synaptic input between recorded cell types (Figure 1.S2) were calculated using the layer-specific cell proportions (percentages) taken from Lee et al. 2010[29]. For inhibitory neuron populations, these proportions were then multiplied by .2. Pyramidal population was by default 100% of the excitatory population, which was then multiplied by .8 as a rough estimate of a 4:1 ratio of excitatory to inhibitory neurons within each layer.

Linear Mixed-Effects Model

We used the general equation:

$$Y = \overset{\text{Intercept}}{\beta_{0j}} + \overset{\text{Fixed effect(s)}}{\beta_{ij} X_{ij}} + \overset{\text{Random effect(s)}}{b_{ij} z_{ij}} + \overset{\text{Error}}{\varepsilon_{ij}}$$

Where Y is the response variable (EPSC peak amplitude), X_{ij} is the fixed predictor variable (4 recorded cell layers), z_{ij} is the random predictor variable (slice, and by extension mouse), and i,j corresponds to observation i (cell) in group j (layer). The null hypothesis H_0 is that the fixed effects coefficient $\beta_{ij} = 0$, i.e. that recorded cell layer is independent of the amount of synaptic input it receives from the ChR2-expressing layer. Due to the nature of the model, comparing all pairwise combinations of layer is not possible; therefore, to test the null hypothesis in each recorded cell type within a single mouse line, a “reference” layer was used to which responses in all other layers were compared. See Figure 1.S11 for additional details. We found that accounting for random variability in ChR2 expression did not explain differences in observed amplitude across layers, adding additional evidence that input strength to a given recorded cell is indeed layer-dependent.

Immunohistochemistry / Histology

Tissue was fixed in 4% paraformaldehyde for 48-72 hours immediately after recording. In some cases, slices were subsequently transferred to a 30% sucrose solution (in PBS) for 24-48 hours and resectioned on a microtome. Laminar boundaries were identified using DAPI staining, and Somatostatin+ cells were identified as part of a separate set of experiments) using Donkey anti-Rabbit/AlexaFluor DsRed 594 (Takara Biosciences). ChR2-EYFP expression was validated using Donkey anti-Chicken 488 (Jackson Immunolabs), and filled cells were identified using a fluorescent avidin stain.

Morphology was visualized using projections from z-stacks, enabling straightforward classification of filled cells as pyramidal or non-pyramidal. Cells were designated as excitatory pyramidal by the presence of visible dendritic spines, thick apical dendrite, descending axon, large pyramidally-shaped soma, and lack of mCherry expression.

Cell morphological identity was confirmed via biocytin fills and laminar location through an LSM/AiryScan 880 microscope (Zeiss) or Olympus BX63. Locations of unfilled cells were determined using images captured during recordings enabling triangulation based on location of filled cells. If no cells were successfully filled in a slice, the laminar location was estimated using overall average laminar boundaries across experiments and measured pial depth taken during recordings. If the cell was not successfully filled with biocytin, the position / laminar location was determined by triangulating coordinates from other cells in the slice and pipette pictures taken during recordings. In 2 experiments, where there were no successful cell fills in the slice, the cell layer was estimated based on its depth from pia, in alignment with other slices and with the Allen Brain Atlas.

There were 25 (of 1207 cells, ~2% of dataset) instances of FlpO-mCherry virus leak, in which recorded cells expressing mCherry were later confirmed to be & assigned as pyramidal. All but 4 of these instances occurred in experiments from VipFlp crosses (Vip cells targeted during recordings).

Appendix

Table 1.S1. Population parameters for recorded cell types. Cell types listed in leftmost column, combined population data in final row. For each parameter, mean is in left column and std deviation on the right. Window refers to integration window by which EPSQ was calculated: the time period in which the EPSC was <10% of its (negative) peak amplitude). Latency refers to the time at which EPSC initially crossed the 10% threshold, i.e. the start of the window post-stimulus onset. Recorded cells with response amplitude <10pA were excluded from Window and Latency calculations. R_{access}, $R_{membrane}$, and $C_{membrane}$ were recorded during test pulse measurement and calculated automatically using Multiclamp 700B software.

	Window (ms)		**Latency** (ms)		**R_{access}** (MΩ)		**$R_{membrane}$** (MΩ)		**$C_{membrane}$** (pF)	
	mean	std. dev.	mean	std. dev.	mean	std. dev.	mean	std. dev.	mean	std. dev.
Pyramidal	109.20	76.58	10.51	5.19	15.69	7.00	398.97	245.18	51.46	51.38
Sst	117.95	98.93	11.08	4.31	14.18	5.82	366.30	224.07	27.72	26.24
Pvalb	108.12	68.08	9.94	4.19	13.87	5.35	254.54	144.02	20.09	9.75
Vip	142.64	114.41	11.64	5.99	14.27	6.01	786.30	474.83	13.15	18.00
Combined	**115.42**	**86.99**	**10.68**	**4.97**	**14.81**	**6.37**	**421.46**	**315.89**	**32.81**	**38.94**

Table 1.S2. Final sample sizes for each mouse line. Mouse line in left column, number of mice for that line are listed in the right column. The average number of cells recorded in each slice was 7.271 cells, with a minimum of 4 cells per slice required for inclusion in dataset.

Line	**# mice**
SepW1	24
Scnn1a	23
Tlx3	28
Npr3	19
Ntsr1	28
Total	**122**

Table 1.S3. Final counts for each recorded cell type. Input layer (Cre mouse line) is listed in top row, recorded cell layer in leftmost column. Bottom row represents total number of cells of each type recorded across all layers in that mouse line. (A), input from L2/3; (B), input from L4; (C), input from L5 IT; (D), input from L5 ET; (E), input from L6 CT.

A	**L2/3**			
	Pyr	**Sst**	**Pvalb**	**Vip**
L2/3	23	17	11	9
L4	32	22	11	6
L5	42	20	10	13
L6	25	14	10	7
Total	122	73	42	35

B	**L4**			
	Pyr	**Sst**	**Pvalb**	**Vip**
L2/3	23	9	8	10
L4	24	12	11	10
L5	25	11	14	14
L6	23	10	14	7
Total	95	42	47	41

C	**L5 IT**			
	Pyr	**Sst**	**Pvalb**	**Vip**
L2/3	30	15	10	5
L4	29	11	10	11
L5	26	22	11	7
L6	24	9	11	10
Total	109	57	42	33

D	**L5 ET**			
	Pyr	**Sst**	**Pvalb**	**Vip**
L2/3	27	9	11	9
L4	28	13	12	9
L5	27	11	8	7
L6	23	11	13	11
Total	105	44	44	36

E	**L6 CT**			
	Pyr	**Sst**	**Pvalb**	**Vip**
L2/3	26	10	10	6
L4	22	17	11	12
L5	33	18	13	7
L6	28	11	11	5
Total	109	56	45	30

Table 1.S4. Population data—Peak Amplitude. Mean peak amplitude of responses for each input layer/population (Cre mouse line), or each recorded cell type, and within each recorded layer. All units are in pA. Top row indicates input layer (Cre mouse line), 2nd row indicates recorded cell type (output population). Leftmost column indicates the assigned layer of postsynaptic cell. Within each cell type, left column indicates mean peak amplitude for the recorded population, right column is the standard deviation. (A), input from L2/3; (B), input from L4; (C), input from L5 IT; (D), input from L5 ET; (E), input from L6 CT.

A	**L2/3**							
	Pyr		**Sst**		**Pvalb**		**Vip**	
	mean	std. dev.	mean	std. dev.	mean	std. dev.	mean	std. dev.
L2/3	-579.693	779.923	-1332.661	848.093	-1326.289	994.422	-102.083	74.873
L4	-173.467	362.796	-788.836	686.240	-475.670	766.975	-63.435	71.112
L5	-481.752	649.402	-153.377	167.799	-390.154	335.916	-25.184	32.276
L6	-18.334	21.178	-14.965	23.178	-87.858	80.621	-9.427	12.918

B	**L4**							
	Pyr		**Sst**		**Pvalb**		**Vip**	
	mean	std. dev.	mean	std. dev.	mean	std. dev.	mean	std. dev.
L2/3	-574.766	649.697	-86.065	104.024	-334.236	202.470	-83.378	105.065
L4	-101.116	116.043	-282.574	316.000	-258.353	222.231	-39.948	57.394
L5	-112.657	134.764	-128.237	217.629	-80.652	110.935	-23.133	40.249
L6	-18.350	33.567	-14.193	15.881	-36.742	47.063	-14.047	12.023

C	**L5 IT**							
	Pyr		**Sst**		**Pvalb**		**Vip**	
	mean	std. dev.	mean	std. dev.	mean	std. dev.	mean	std. dev.
L2/3	-653.185	759.286	-226.985	242.556	-851.659	693.009	-54.058	96.734
L4	-87.075	102.104	-317.056	419.585	-347.213	289.551	-97.214	220.970
L5	-181.705	280.047	-110.923	116.558	-574.344	646.083	-152.830	324.206
L6	-137.638	153.102	-16.415	29.295	-96.381	79.234	-122.968	145.368

D	**L5 ET**							
	Pyr		**Sst**		**Pvalb**		**Vip**	
	mean	std. dev.	mean	std. dev.	mean	std. dev.	mean	std. dev.
L2/3	-60.060	70.793	-81.535	105.530	-17.022	11.279	-14.650	15.963
L4	-12.647	16.785	-183.068	261.117	-14.773	18.732	-20.293	19.413
L5	-193.540	176.519	-67.871	70.190	-161.847	213.161	-126.392	237.877
L6	-310.573	221.603	-306.381	403.544	-173.794	340.088	-28.816	44.410

E	**L6 CT**							
	Pyr		**Sst**		**Pvalb**		**Vip**	
	mean	std. dev.	mean	std. dev.	mean	std. dev.	mean	std. dev.
L2/3	-7.753	10.851	-3.030	2.042	-3.576	3.029	-4.390	3.493
L4	-220.453	404.538	-91.475	120.584	-181.343	181.762	-14.883	14.738
L5	-137.254	203.865	-136.674	185.328	-192.979	285.519	-331.047	841.734
L6	-117.635	257.034	-195.124	401.291	-360.295	290.105	-38.794	49.854

Table 1.S5. Population data—Integrated Synaptic Current (EPSQ). Mean EPSQ of responses for each input layer/population (Cre mouse line), or each recorded cell type, and within each recorded layer. All units are in pC. Organization as in Table 1.SX. (A), input from L2/3; (B), input from L4; (C), input from L5 IT; (D), input from L5 ET; (E), input from L6 CT.

A	**L2/3**							
	Pyr		**Sst**		**Pvalb**		**Vip**	
	mean	std. dev.	mean	std. dev.	mean	std. dev.	mean	std. dev.
L2/3	-16.437	26.848	-57.917	54.587	-45.855	50.630	-2.797	1.672
L4	-4.049	9.084	-29.900	37.146	-12.310	20.391	-1.532	1.731
L5	-11.840	17.741	-4.993	7.079	-10.154	10.105	-0.348	0.479
L6	-0.562	0.717	-0.446	0.859	-2.044	1.687	-0.131	0.222

B	**L4**							
	Pyr		**Sst**		**Pvalb**		**Vip**	
	mean	std. dev.	mean	std. dev.	mean	std. dev.	mean	std. dev.
L2/3	-29.087	41.107	-3.053	3.677	-13.916	7.578	-6.477	8.434
L4	-4.574	6.377	-10.350	12.898	-10.955	7.615	-1.972	3.741
L5	-4.633	5.808	-4.960	10.040	-2.677	3.902	-0.940	1.407
L6	-0.773	1.503	-0.870	1.435	-1.379	2.465	-0.353	0.311

C	**L5 IT**							
	Pyr		**Sst**		**Pvalb**		**Vip**	
	mean	std. dev.	mean	std. dev.	mean	std. dev.	mean	std. dev.
L2/3	-31.092	36.513	-8.552	12.498	-35.783	31.431	-2.278	2.616
L4	-4.135	5.516	-12.549	23.288	-11.144	9.767	-4.773	10.410
L5	-7.828	10.861	-4.719	6.004	-18.984	27.244	-3.736	7.948
L6	-9.064	10.768	-0.568	0.806	-3.208	3.607	-4.014	5.013

D	**L5 ET**							
	Pyr		**Sst**		**Pvalb**		**Vip**	
	mean	std. dev.	mean	std. dev.	mean	std. dev.	mean	std. dev.
L2/3	-2.696	3.343	-2.692	4.343	-0.621	0.638	-0.930	1.394
L4	-0.485	0.776	-8.610	17.436	-0.504	0.691	-0.591	0.476
L5	-7.220	6.988	-4.125	5.020	-7.277	13.555	-8.519	15.238
L6	-11.025	8.582	-11.001	15.199	-9.048	21.679	-1.182	2.038

E	**L6 CT**							
	Pyr		**Sst**		**Pvalb**		**Vip**	
	mean	std. dev.	mean	std. dev.	mean	std. dev.	mean	std. dev.
L2/3	-0.377	0.725	-0.121	0.227	-0.105	0.309	-0.227	0.314
L4	-16.618	40.812	-4.693	7.291	-7.198	7.847	-0.872	0.862
L5	-12.884	39.542	-8.079	11.081	-17.130	41.349	-0.380	0.289
L6	-8.421	16.895	-20.547	44.897	-27.840	31.154	-1.777	2.061

Table 1.S6. Pairwise statistical comparison lookup tables—Peak Amplitude. Pairwise comparison of mean peak amplitude of responses for each cell type. Top row indicates input layer (Cre mouse line), 2nd row indicates recorded cell type (output population). Leftmost column indicates the layers being compared within mouse line; for each cell type, values represent the p-value for paired Wilcoxon signed rank test, and adjacent (right) column indicates significance value of p-values: ***p<.001, **p<.01, *p<.05, otherwise n.s. All values are Bonferroni-corrected. (A), input from L2/3; (B), input from L4; (C), input from L5 IT; (D), input from L5 ET; (E), input from L6 CT.

A	**L2/3**							
	Pyr		**Sst**		**Pvalb**		**Vip**	
L2/3 vs L4	0.002	**	0.224	n.s.	0.052	n.s.	2.330	n.s.
L2/3 vs L5	2.001	n.s.	0.000	***	0.227	n.s.	0.055	n.s.
L2/3 vs L6	0.000	***	0.000	***	0.001	***	0.020	*
L4 vs L5	0.002	**	0.009	**	3.584	n.s.	1.464	n.s.
L4 vs L6	0.183	n.s.	0.000	***	0.588	n.s.	0.441	n.s.
L5 vs L6	0.000	***	0.003	**	0.127	n.s.	3.475	n.s.

B	**L4**							
	Pyr		**Sst**		**Pvalb**		**Vip**	
L2/3 vs L4	0.017	*	0.420	n.s.	1.236	n.s.	1.115	n.s.
L2/3 vs L5	0.018	*	5.275	n.s.	0.018	*	0.195	n.s.
L2/3 vs L6	0.000	***	0.392	n.s.	0.002	**	0.259	n.s.
L4 vs L5	3.251	n.s.	1.115	n.s.	0.017	*	1.672	n.s.
L4 vs L6	0.000	***	0.010	*	0.000	***	4.014	n.s.
L5 vs L6	0.008	**	0.159	n.s.	0.967	n.s.	2.871	n.s.

C	**L5 IT**							
	Pyr		**Sst**		**Pvalb**		**Vip**	
L2/3 vs L4	0.000	***	4.298	n.s.	0.454	n.s.	5.478	n.s.
L2/3 vs L5	0.003	**	2.073	n.s.	1.472	n.s.	2.591	n.s.
L2/3 vs L6	0.005	**	0.074	n.s.	0.075	n.s.	4.072	n.s.
L4 vs L5	4.688	n.s.	0.580	n.s.	4.508	n.s.	2.250	n.s.
L4 vs L6	1.876	n.s.	0.030	*	0.435	n.s.	4.191	n.s.
L5 vs L6	3.251	n.s.	0.005	**	0.604	n.s.	1.889	n.s.

D	**L5 ET**							
	Pyr		**Sst**		**Pvalb**		**Vip**	
L2/3 vs L4	0.000	***	1.376	n.s.	1.242	n.s.	2.041	n.s.
L2/3 vs L5	0.010	*	5.637	n.s.	0.094	n.s.	0.329	n.s.
L2/3 vs L6	0.003	**	1.179	n.s.	4.369	n.s.	5.275	n.s.
L4 vs L5	0.000	***	1.782	n.s.	0.029	*	1.263	n.s.
L4 vs L6	0.000	***	3.374	n.s.	0.808	n.s.	3.260	n.s.
L5 vs L6	0.440	n.s.	0.786	n.s.	1.082	n.s.	1.075	n.s.

E	**L6 CT**							
	Pyr		**Sst**		**Pvalb**		**Vip**	
L2/3 vs L4	0.068	n.s.	0.002	**	0.002	**	0.498	n.s.
L2/3 vs L5	0.000	***	0.000	***	0.000	***	0.210	n.s.
L2/3 vs L6	0.000	***	0.003	**	0.001	***	0.312	n.s.
L4 vs L5	2.428	n.s.	2.746	n.s.	4.110	n.s.	3.215	n.s.
L4 vs L6	5.486	n.s.	3.435	n.s.	1.273	n.s.	3.035	n.s.
L5 vs L6	1.395	n.s.	5.038	n.s.	0.885	n.s.	6.000	n.s.

Table 1.S7. Pairwise statistical comparison lookup tables—EPSQ. (A), pairwise comparison of mean EPSQ of responses for each cell type. Top row indicates input layer (Cre mouse line), 2nd row indicates recorded cell type (output population). Leftmost column indicates the layers being compared within mouse line. For each cell type, values in left column represent the p-value for Wilcoxon signed rank test. Adjacent (right) column significance value of p-values: ***p<.001, **p<.01, *p<.05, otherwise n.s. All values are Bonferroni-corrected. (A), input from L2/3; (B), input from L4; (C), input from L5 IT; (D), input from L5 ET; (E), input from L6 CT.

A	**L2/3**							
	Pyr		**Sst**		**Pvalb**		**Vip**	
L2/3 vs L4	0.001	***	0.552	n.s.	0.052	n.s.	1.633	n.s.
L2/3 vs L5	1.546	n.s.	0.000	***	0.159	n.s.	0.006	**
L2/3 vs L6	0.000	***	0.000	***	0.001	***	0.013	*
L4 vs L5	0.003	**	0.024	*	2.272	n.s.	0.525	n.s.
L4 vs L6	0.453	n.s.	0.000	***	0.507	n.s.	0.308	n.s.
L5 vs L6	0.000	***	0.008	**	0.154	n.s.	2.854	n.s.

B	**L4**							
	Pyr		**Sst**		**Pvalb**		**Vip**	
L2/3 vs L4	0.043	*	0.759	n.s.	2.370	n.s.	0.727	n.s.
L2/3 vs L5	0.026	*	5.637	n.s.	0.007	**	0.091	n.s.
L2/3 vs L6	0.000	***	0.677	n.s.	0.002	**	0.019	*
L4 vs L5	3.660	n.s.	0.543	n.s.	0.007	**	2.575	n.s.
L4 vs L6	0.000	***	0.030	*	0.001	***	2.183	n.s.
L5 vs L6	0.005	**	1.472	n.s.	1.448	n.s.	4.764	n.s.

C	**L5 IT**							
	Pyr		**Sst**		**Pvalb**		**Vip**	
L2/3 vs L4	0.001	***	3.623	n.s.	0.323	n.s.	3.967	n.s.
L2/3 vs L5	0.009	**	3.790	n.s.	0.679	n.s.	1.212	n.s.
L2/3 vs L6	0.079	n.s.	0.102	n.s.	0.061	n.s.	5.155	n.s.
L4 vs L5	4.294	n.s.	1.374	n.s.	6.000	n.s.	1.478	n.s.
L4 vs L6	1.171	n.s.	0.047	*	0.507	n.s.	4.508	n.s.
L5 vs L6	3.577	n.s.	0.023	*	0.786	n.s.	1.377	n.s.

D	**L5 ET**							
	Pyr		**Sst**		**Pvalb**		**Vip**	
L2/3 vs L4	0.003	**	0.851	n.s.	2.875	n.s.	3.629	n.s.
L2/3 vs L5	0.063	n.s.	4.567	n.s.	0.005	**	0.544	n.s.
L2/3 vs L6	0.007	**	0.568	n.s.	5.172	n.s.	4.918	n.s.
L4 vs L5	0.000	***	3.612	n.s.	0.014	*	0.329	n.s.
L4 vs L6	0.000	***	3.144	n.s.	2.777	n.s.	2.684	n.s.
L5 vs L6	0.717	n.s.	1.586	n.s.	0.234	n.s.	0.207	n.s.

E	**L6 CT**							
	Pyr		**Sst**		**Pvalb**		**Vip**	
L2/3 vs L4	0.042	*	0.012	*	0.002	**	1.277	n.s.
L2/3 vs L5	0.000	***	0.000	***	0.001	***	0.441	n.s.
L2/3 vs L6	0.000	***	0.005	**	0.001	***	0.494	n.s.
L4 vs L5	2.606	n.s.	1.701	n.s.	4.900	n.s.	5.022	n.s.
L4 vs L6	3.876	n.s.	1.438	n.s.	1.134	n.s.	2.653	n.s.
L5 vs L6	3.347	n.s.	4.621	n.s.	0.558	n.s.	3.182	n.s.

Table 1.S8. Estimated population sizes in each V1 layer for each cell type within cortical layer. Data used for normalizing mean EPSQs in stacked barplots (figure 1.S8). Relative cortical layer thicknesses were used from Keller et al. 2018. (A) density of interneuron types from Xu & Callaway 2018[30]. Pyramidal cell density was calculated by multiplying density of GABAergic cells (Xu & Callaway 2018) by 4, with the estimation that excitatory neurons in each layer outnumbered inhibitory cells approximately 4:1. Cell densities were multiplied by relative layer thicknesses to determine relative population sizes. (B) Relative population sizes of 3 interneuron populations within cortical layers, from Lee et al. 2010[29], used for normalizing input distributions for within-layer analysis (far right column in figure 1.8). Pyramidal cells assumed to outnumber inhibitory cells approximately 4:1 in each layer.

A	**Cell population size (10^3 cells/mm^3)** Adjusted for layer thickness			
	Pyr	**Sst**	**Pvalb**	**Vip**
L2/3	3606.96	71.022	186.732	151.487
L4	3220	169.1	405.5	52.1
L5	4909.8	305.443	666.831	50.768
L6	3800	194.2	487.6	77.6

B	**Within-layer proportion** of all GABAergic cells		
	Sst	**Pvalb**	**Vip**
L2/3	0.2	0.3	0.2
L4	0.3	0.55	0.045
L5	0.45	0.45	0.0225
L6	0.45	0.45	0.045

Table 1.S9. Linear mixed-effects model. P-value lookup tables for all tested comparisons for each mouse line. (A) Reference layer used for each mouse line and each recorded cell type. Reference layer was assigned to be the layer with the highest average EPSQ for that cell type (the layer that received the most synaptic input). Recorded cell EPSQs were compared between reference layer and all other layers. (B-F). For each mouse line (input population at top) p-value of model fit using fixed effect of recorded cell layer and random effect of slice (and by extension, mouse). For each pairwise layer comparison within cell type, p-value is listed in left column and significance is listed in the right (***p<.001, **p<.01, *p<.05, otherwise n.s.). Values are Bonferroni-corrected.

A	**Reference Layer**			
	Pyr	**Sst**	**Pvalb**	**Vip**
L2/3	2/3	2/3	2/3	2/3
L4	2/3	4	2/3	2/3
L5 IT	2/3	4	2/3	4
L5 ET	6	6	6	5
L6 CT	4	6	6	5

B	**L2/3**							
	Pyr		**Sst**		**Pvalb**		**Vip**	
L2/3 vs L4	0.006	**	0.000	***	0.003	**	0.165	n.s.
L2/3 vs L5	0.501	n.s.	0.000	***	0.003	**	0.000	***
L2/3 vs L6	0.000	***	0.000	***	0.000	***	0.000	***
L4 vs L5								
L4 vs L6								
L5 vs L6								

C	**L4**							
	Pyr		**Sst**		**Pvalb**		**Vip**	
L2/3 vs L4	0.000	***	0.033	*	0.262	n.s.	0.023	*
L2/3 vs L5	0.000	***			0.000	***	0.001	***
L2/3 vs L6	0.000	***			0.000	***	0.003	**
L4 vs L5			0.068	n.s.				
L4 vs L6			0.003	**				
L5 vs L6								

D	**L5 IT**							
	Pyr		**Sst**		**Pvalb**		**Vip**	
L2/3 vs L4	0.000	***	0.348	n.s.	0.004	**	0.685	n.s.
L2/3 vs L5	0.000	***			0.153	n.s.		
L2/3 vs L6	0.000	***			0.000	***		
L4 vs L5			0.012	*			0.170	n.s.
L4 vs L6			0.003	**			0.907	n.s.
L5 vs L6								

E	**L5 ET**							
	Pyr		**Sst**		**Pvalb**		**Vip**	
L2/3 vs L4								
L2/3 vs L5							0.017	*
L2/3 vs L6	0.000	***	0.046	*	0.059	n.s.		
L4 vs L5							0.064	n.s.
L4 vs L6	0.000	***	0.222	n.s.	0.051	n.s.		
L5 vs L6	0.003	**	0.026	*	0.893	n.s.	0.112	n.s.

F	**L6 CT**							
	Pyr		**Sst**		**Pvalb**		**Vip**	
L2/3 vs L4	0.003	**						
L2/3 vs L5							0.131	n.s.
L2/3 vs L6			0.040	*	0.001	***		
L4 vs L5	0.220	n.s.					0.090	n.s.
L4 vs L6	0.144	n.s.	0.204	n.s.	0.016	*		
L5 vs L6			0.466	n.s.	0.047	*	0.197	n.s.

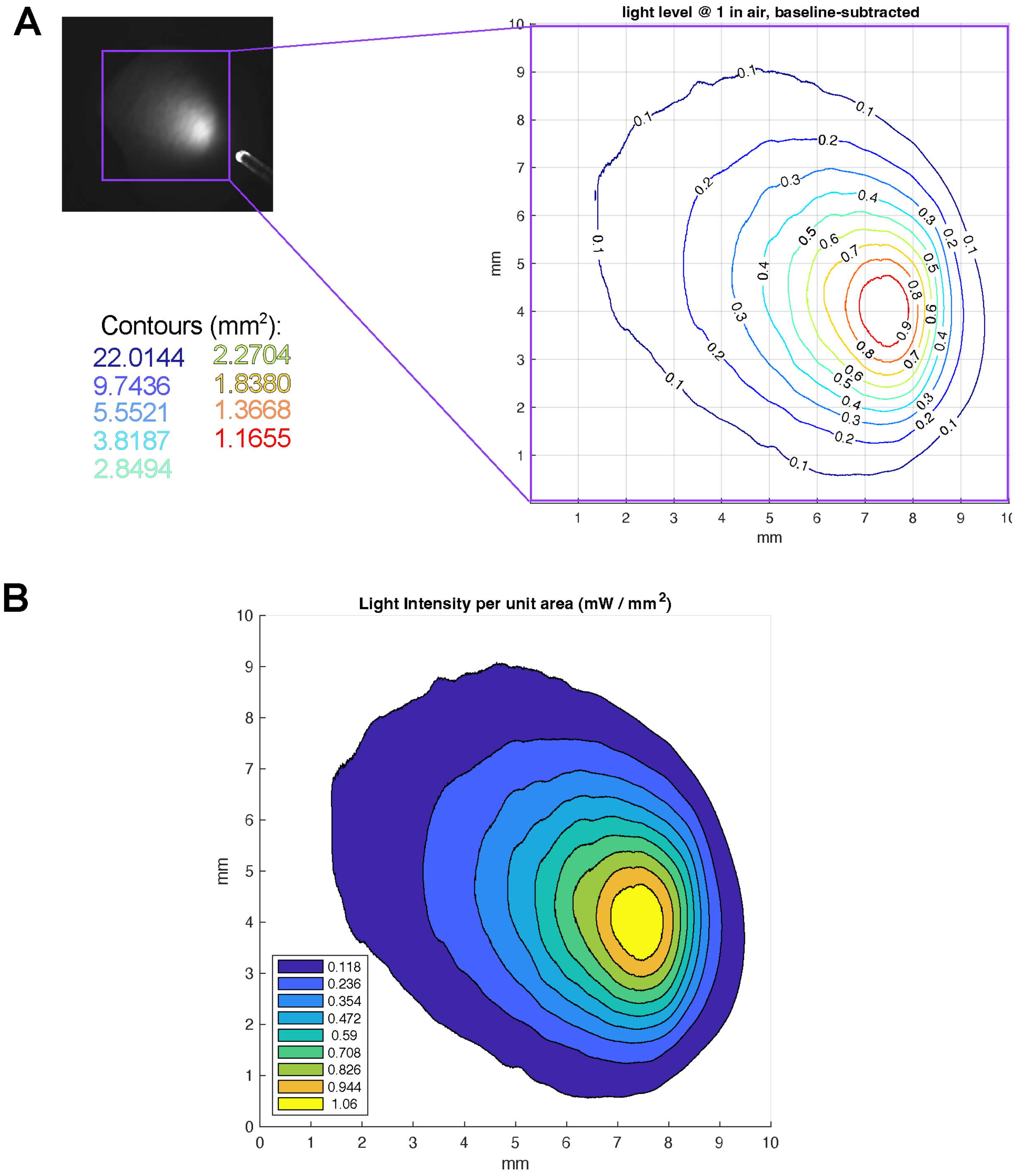

Figure 1.S1. LED intensity drop off with distance. (A) Left, photo of setup, LED light source in bottom right corner. Illumination intensity for the region framed in purple was measured to determine extent to which illumination decreased over the surface of recorded slice. Contours represent 10% of max LED intensity as measured with photosensor (16mW in air). (B), estimated light intensity per unit area based on contour and maximum illumination intensity.

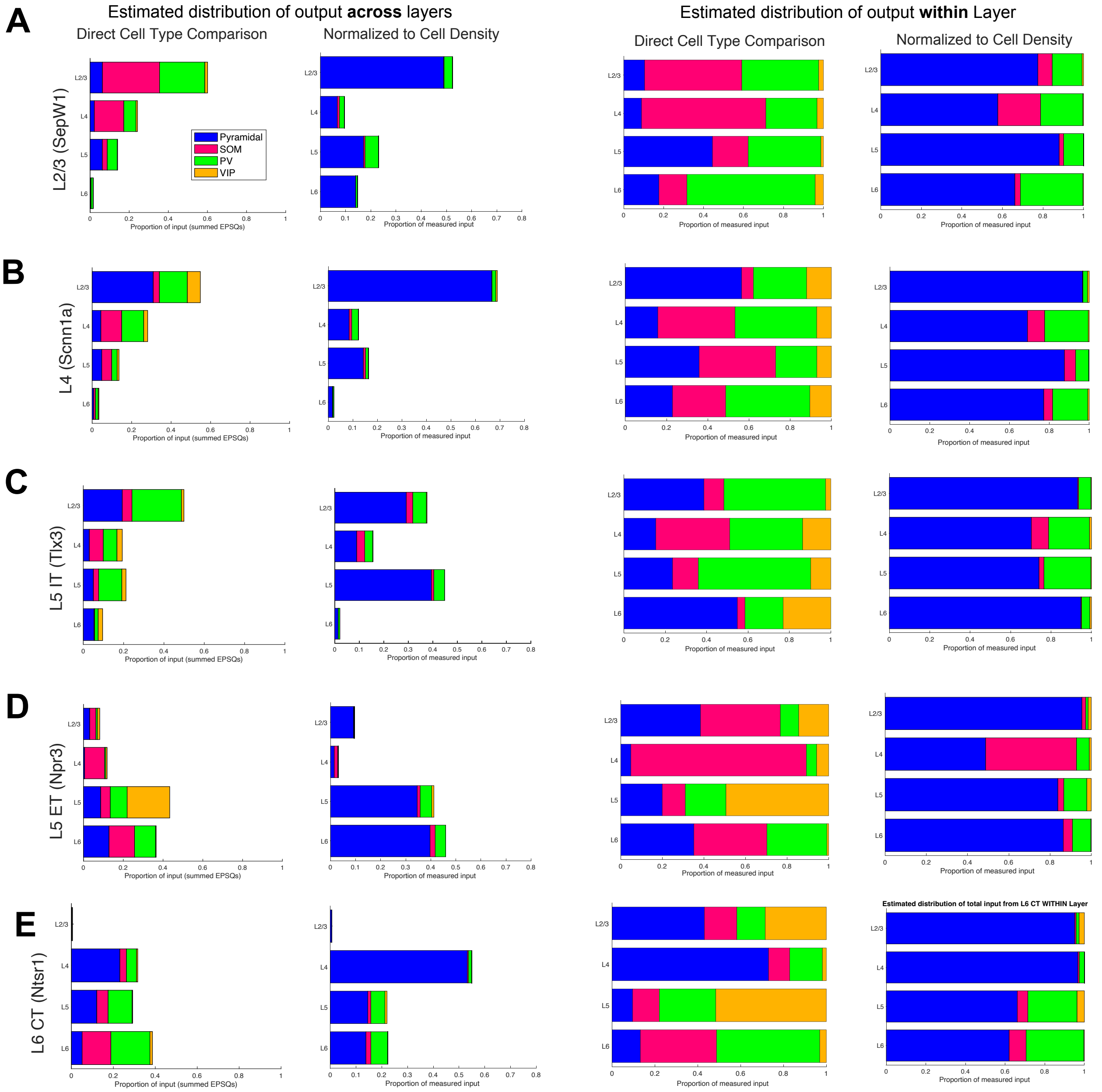

Figure 1.S2. Comparison of synaptic input distribution to each recorded cell type. The first column of stacked bars represents the proportion of input provided to each recorded cell type within each layer, calculated by summing the mean EPSQ for all 16 populations (4 recorded cell types across 4 layers) and dividing by the mean EPSQ for that cell type within a single layer. The 2nd column is the same data from the first column, normalized to cell population size in each layer (calculated from cell type density & layer thickness, see table 1.SX for values used). 3rd column: summed mean EPSQ of 4 cell types within layer, divided by mean EPSQ for each type. 4th column: estimated distribution of synaptic input within layer, determined by relative proportion of cell populations within that layer (see table 1.SX for values used). (A), input from L2/3; (B), input from L4; (C), input from L5 IT; (D), input from L5 ET; (E), input from L6 CT.

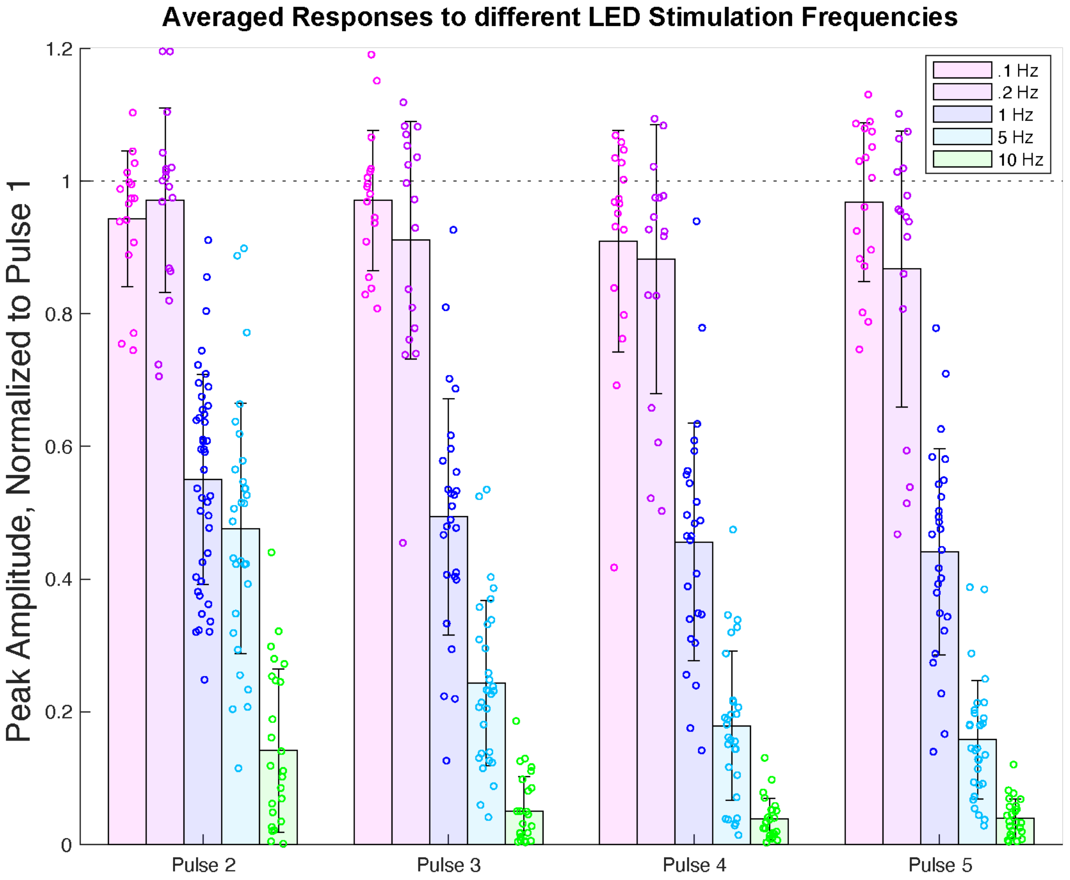

Figure 1.S3. LED Stimulation frequencies ≤.2Hz do not affect EPSC Amplitude. 5 LED pulses were delivered to recorded cells at 5 different frequencies. Each point represents averaged peak amplitude for a single recorded cell for pulses 2-5 across a minimum of 10 trials. Responses are normalized to the amplitude observed after the first light pulse at that particular frequency. At .2Hz, peak amplitude did not significantly decrease across pulses; therefore, the frequency used in subsequent experiments was .2Hz (5s trials). Error bars denote s.e.m.

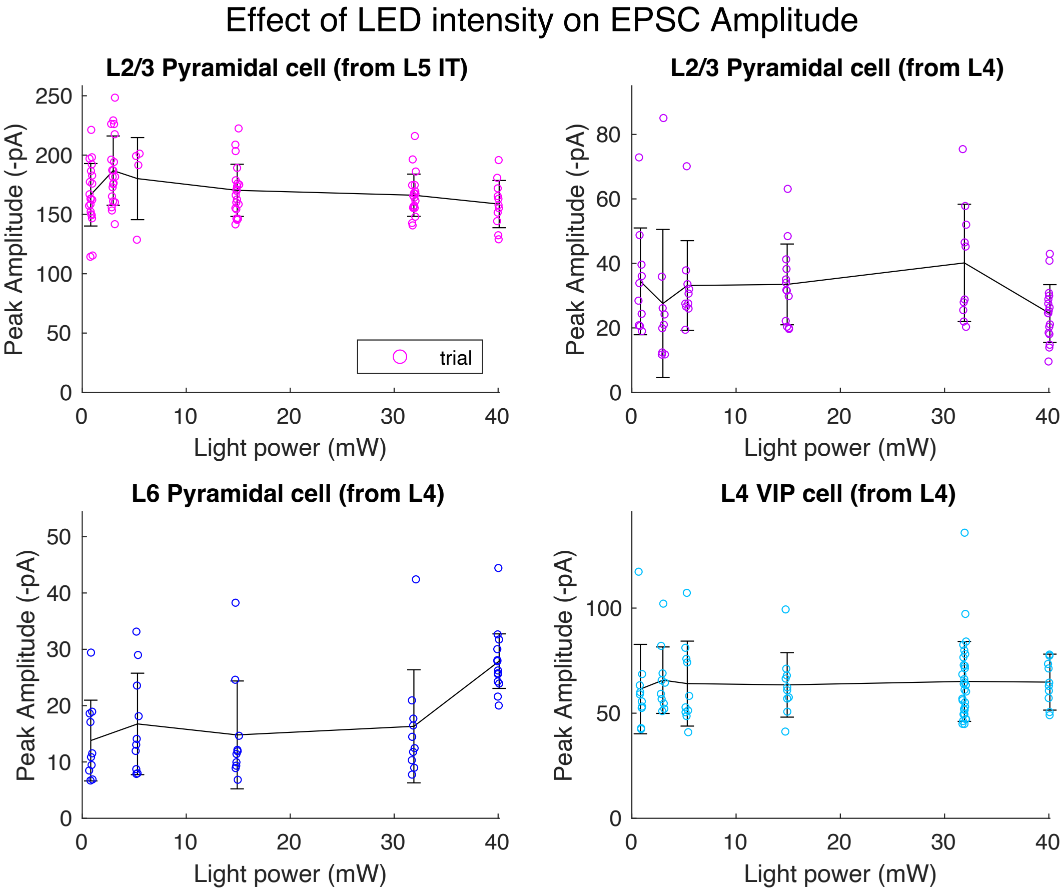

Figure 1.S4. LED Intensity does not affect response amplitude. Data from 4 different cells was collected after initial stimulation protocol was run. Each plotted cell's data is from a different slice experiment. Each plot is data from a different cell, and each point represents recorded peak amplitude of EPSC in a single trial. Light levels were varied in pseudorandom order and responses were recorded. Light power (x-axis) corresponding to each light level was calculated post-hoc using a photodetector. No significant differences in peak amplitude were noted across light levels or trials for any of the recorded cells. Error bars denote s.e.m.

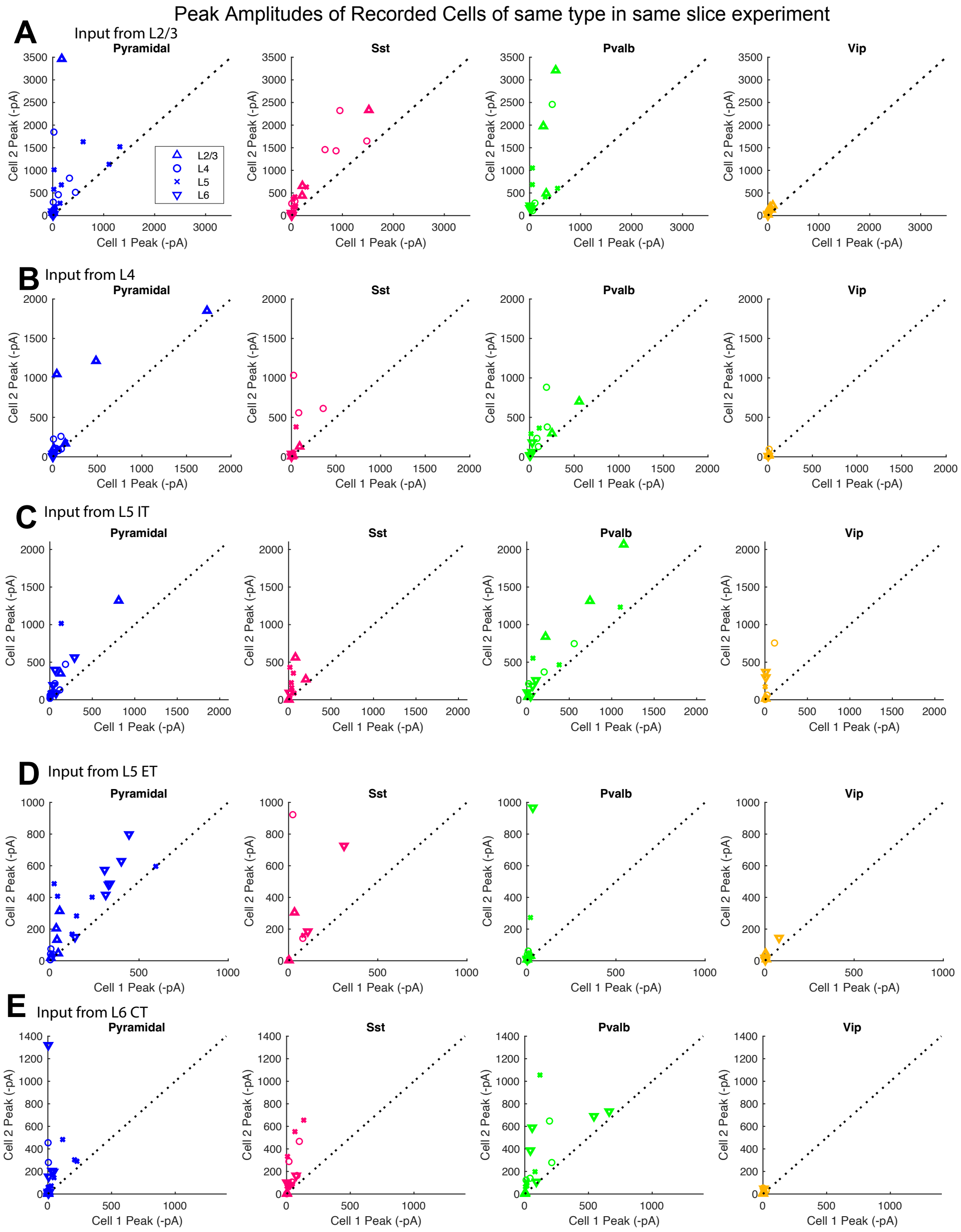

Figure 1.S5. Cells of the same type in the same slice experiment exhibit large variability in response amplitudes. Comparison of response amplitudes exhibited by cells of the same type, in the same recorded layer, of the same slice, ordered by mean response amplitude. Cell 1 peak (smaller response) is plotted on the x-axis, and cell 2 peak is plotted on y. Dotted line is x = y; points deviating more strongly from line indicate higher variability in response. Axes are identical within each input population, highlighting variability in EPSCs across cell types. (A), input from L2/3; (B), input from L4; (C), input from L5 IT; (D), input from L5 ET; (E), input from L6 CT. Each column/color scheme indicates postsynaptic cell type.

Acknowledgments

Chapter 1, in full, is currently being prepared for submission for publication and will include Professor Edward Callaway as the senior author. The dissertation author was the primary investigator and author of this chapter.

References

1. Gilbert, C. D. (1983). Microcircuitry of the visual cortex. *Annual Review of Neuroscience, Vol. 6*, 217–247. https://doi.org/10.1146/annurev.ne.06.030183.001245
2. Binzegger, T. (2004). A Quantitative Map of the Circuit of Cat Primary Visual Cortex. *Journal of Neuroscience*, *24*(39), 8441–8453. https://doi.org/10.1523/JNEUROSCI.1400-04.2004
3. Douglas, R. J., & Martin, K. A. (1991). A functional microcircuit for cat visual cortex. *The Journal of Physiology*, *440*(1), 735–769. https://doi.org/10.1113/jphysiol.1991.sp018733
4. Douglas, R. J., & Martin, K. A. C. (2004). Neuronal circuits of the neocortex. *Annual Review of Neuroscience*, *27*, 419–451. https://doi.org/10.1146/annurev.neuro.27.070203.144152
5. Thomson, A. M., & Lamy, C. (2007). Functional Maps of Neocortical Local Circuitry. *Frontiers in Neuroscience*, *1*(1), 19–42. https://doi.org/10.3389/neuro.01.1.1.002.2007
6. Lefort, S., Tomm, C., Sarria, J.-C. F., & Petersen, C. C. H. (2009). The Excitatory Neuronal Network of the C2 Barrel Column in Mouse Primary Somatosensory Cortex. *Neuron*, *61*(4), 301–316. https://doi.org/10.1016/j.neuron.2008.12.020
7. Brown, S. P., & Hestrin, S. (2009). Intracortical circuits of pyramidal neurons reflect their long-range axonal targets. *Nature*, *457*(7233), 1133–1136. https://doi.org/10.1038/nature07658
8. Stepanyants, A., Martinez, L. M., Ferecskó, A. S., & Kisvárday, Z. F. (2009). The fractions of short- and long-range connections in the visual cortex. *Proceedings of the National Academy of Sciences of the United States of America*, *106*(9), 3555–3560. https://doi.org/10.1073/pnas.0810390106
9. Gouwens, N. W., Sorensen, S. A., Berg, J., Lee, C., Jarsky, T., Ting, J., Sunkin, S. M., Feng, D., Anastassiou, C. A., Barkan, E., Bickley, K., Blesie, N., Braun, T., Brouner, K., Budzillo, A., Caldejon, S., Casper, T., Castelli, D., Chong, P., … Koch, C. (2019). Classification of electrophysiological and morphological neuron types in the mouse visual cortex. *Nature Neuroscience*, *22*(7), 1182–1195. https://doi.org/10.1038/s41593-019-0417-0
10. Gouwens, N. W., Sorensen, S. A., Baftizadeh, F., Budzillo, A., Lee, B. R., Jarsky, T., Alfiler, L., Baker, K., Barkan, E., Berry, K., Bertagnolli, D., Bickley, K., Bomben, J., Braun, T., Brouner, K., Casper, T., Crichton, K., Daigle, T. L., Dalley, R., … Zeng, H. (2020). Integrated Morphoelectric and Transcriptomic Classification of Cortical GABAergic Cells. *Cell*, *183*(4), 935-953.e19. https://doi.org/10.1016/j.cell.2020.09.057

11. Petreanu, L., Mao, T., Sternson, S. M., & Svoboda, K. (2009). The subcellular organization of neocortical excitatory connections. *Nature*, *457*(7233), 1142–1145. https://doi.org/10.1038/nature07709
12. Dantzker, J. L., & Callaway, E. M. (2000). Laminar sources of synaptic input to cortical inhibitory interneurons and pyramidal neurons. *Nature Neuroscience*, *3*(7), 701–707. https://doi.org/10.1038/76656
13. Kim, J., Matney, C. J., Blankenship, A., Hestrin, S., & Brown, S. P. (2014). Layer 6 Corticothalamic Neurons Activate a Cortical Output Layer, Layer 5a. *Journal of Neuroscience*, *34*(29), 9656–9664. https://doi.org/10.1523/JNEUROSCI.1325-14.2014
14. Gardner, D. (1980). Time integral of synaptic conductance. *The Journal of Physiology*, *304*, 181–191.
15. Lee, C., Côté, S. L., Raman, N., Chaudhary, H., Mercado, B. C., & Chen, S. X. (2023). Whole-brain mapping of long-range inputs to the VIP-expressing inhibitory neurons in the primary motor cortex. *Frontiers in Neural Circuits*, *17*. https://www.frontiersin.org/articles/10.3389/fncir.2023.1093066
16. Pfeffer, C. K., Xue, M., He, M., Huang, Z. J., & Scanziani, M. (2013). Inhibition of inhibition in visual cortex: The logic of connections between molecularly distinct interneurons. *Nature Neuroscience*, *16*(8), 1068–1076. https://doi.org/10.1038/nn.3446
17. Olsen, S. R., Bortone, D. S., Adesnik, H., & Scanziani, M. (2012). Gain control by layer six in cortical circuits of vision. *Nature*, *483*(7387), 47–52. https://doi.org/10.1038/nature10835
18. Frandolig, J. E., Matney, C. J., Lee, K., Kim, J., Chevée, M., Kim, S.-J., Bickert, A. A., & Brown, S. P. (2019). The Synaptic Organization of Layer 6 Circuits Reveals Inhibition as a Major Output of a Neocortical Sublamina. *Cell Reports*, *28*(12), 3131-3143.e5. https://doi.org/10.1016/j.celrep.2019.08.048
19. Bortone, D. S., Olsen, S. R., & Scanziani, M. (2014). Translaminar Inhibitory Cells Recruited by Layer 6 Corticothalamic Neurons Suppress Visual Cortex. *Neuron*, *82*(2), 474–485. https://doi.org/10.1016/j.neuron.2014.02.021
20. Kätzel, D., Zemelman, B. V., Buetfering, C., Wölfel, M., & Miesenböck, G. (2011). The columnar and laminar organization of inhibitory connections to neocortical excitatory cells. *Nature Neuroscience*, *14*(1), Article 1. https://doi.org/10.1038/nn.2687
21. Pluta, S., Naka, A., Veit, J., Telian, G., Yao, L., Hakim, R., Taylor, D., & Adesnik, H. (2015). A direct translaminar inhibitory circuit tunes cortical output. *Nature Neuroscience*, *18*(11), 1631–1640. https://doi.org/10.1038/nn.4123
22. Okoro, S. U., Goz, R. U., Njeri, B. W., Harish, M., Ruff, C. F., Ross, S. E., Gerfen, C. R., & Hooks, B. M. (2022). Organization of cortical and thalamic input to inhibitory neurons in mouse motor cortex. *Journal of Neuroscience*. https://doi.org/10.1523/JNEUROSCI.0950-22.2022
23. Goz, R. U., & Hooks, B. M. (2023). Correlated Somatosensory Input in Parvalbumin/Pyramidal Cells in Mouse Motor Cortex. *ENeuro*, *10*(5). https://doi.org/10.1523/ENEURO.0488-22.2023
24. Negrón, A., Getz, M. P., Handy, G., & Doiron, B. (2023). The mechanics of correlated variability in segregated cortical excitatory subnetworks. *BioRxiv: The Preprint Server for Biology*, 2023.04.25.538323. https://doi.org/10.1101/2023.04.25.538323
25. Peng, H., Xie, P., Liu, L., Kuang, X., Wang, Y., Qu, L., Gong, H., Jiang, S., Li, A., Ruan, Z., Ding, L., Yao, Z., Chen, C., Chen, M., Daigle, T. L., Dalley, R., Ding, Z., Duan, Y.,

Feiner, A., … Zeng, H. (2021). Morphological diversity of single neurons in molecularly defined cell types. *Nature*, *598*(7879), 174–181. https://doi.org/10.1038/s41586-021-03941-1

26. Cadwell, C. R., Palasantza, A., Jiang, X., Berens, P., Deng, Q., Yilmaz, M., Reimer, J., Shen, S., Bethge, M., Tolias, K. F., Sandberg, R., & Tolias, A. S. (2016). Electrophysiological, transcriptomic and morphologic profiling of single neurons using Patch-seq. *Nature Biotechnology*, *34*(2), Article 2. https://doi.org/10.1038/nbt.3445
27. Cadwell, C. R., Scala, F., Li, S., Livrizzi, G., Shen, S., Sandberg, R., Jiang, X., & Tolias, A. S. (2017). Multimodal profiling of single-cell morphology, electrophysiology, and gene expression using Patch-seq. *Nature Protocols*, *12*(12), Article 12. https://doi.org/10.1038/nprot.2017.120
28. Cossell, L., Iacaruso, M. F., Muir, D. R., Houlton, R., Sader, E. N., Ko, H., Hofer, S. B., & Mrsic-Flogel, T. D. (2015). Functional organization of excitatory synaptic strength in primary visual cortex. *Nature*, *518*(7539), Article 7539. https://doi.org/10.1038/nature14182
29. Lee, S., Hjerling-Leffler, J., Zagha, E., Fishell, G., & Rudy, B. (2010). The Largest Group of Superficial Neocortical GABAergic Interneurons Expresses Ionotropic Serotonin Receptors. *Journal of Neuroscience*, *30*(50), 16796–16808. https://doi.org/10.1523/JNEUROSCI.1869-10.2010
30. Xu, X., Roby, K. D., & Callaway, E. M. (2010). Immunochemical characterization of inhibitory mouse cortical neurons: Three chemically distinct classes of inhibitory cells. *The Journal of Comparative Neurology*, *518*(3), 389–404. https://doi.org/10.1002/cne.22229

Chapter 2. Transcriptomic Cell Type Specificity of Local Cortical Circuits

Abstract

The complex functions of the neocortex rely on networks of interconnected excitatory and inhibitory interneurons, each of which are composed of multiple neuron types. Prior studies have established rules of local connectivity between major subclasses of inhibitory and excitatory cortical neurons, but the advent of single-cell transcriptomic technologies has revealed a remarkable diversity in transcriptomic neuronal subtypes. Is there specificity of synaptic connections between cortical neurons classified at the level of transcriptomic subtypes, as might be expected if the different types mediate different functions? Here we present a novel method that ties together transcriptomic cell type and anatomical connectivity, "**S**ingle **T**ranscriptome **A**ssisted **R**abies **T**racing" (START). START combines monosynaptic rabies tracing and single-nuclei RNA sequencing (snRNA-seq) to identify the transcriptomic cell types for 23,940 neurons providing monosynaptic inputs to defined populations of neurons. We employed START in conjunction with Cre driver mouse lines to transcriptomically characterize the monosynaptic inputs to 5 layer-specific excitatory cortical neuron populations in mouse V1. At the subclass level, we observed the results expected from prior studies that resolved neuronal subclasses based on antibody staining, Cre-expressing mouse lines, or morphological characterization. With improved neuronal subtype granularity achieved with START, we were able to demonstrate transcriptomic subtype specificity of inhibitory inputs to the different subclasses of excitatory neurons. These results establish a new set of local connectivity rules at the resolution of transcriptomic inhibitory cell types.

Introduction

The neocortex is composed of an array of neuronal types that serve unique functional roles in sensory information processing and can be defined based on morphological, molecular, and physiological properties[1]. Recently, the use of transcriptomic classification in conjunction with morphological and electrophysiological cell characterization has highlighted the myriad ways in which neurons can be typified and the specificity of their unique functional characteristics [2–5]. These expansive multi-omics datasets raise new questions about the level of granularity by which neurons are most accurately and effectively distinguished[6]. In addition to intrinsic properties, the functional contributions of neurons are determined by their excitatory and inhibitory inputs and outputs; therefore, to understand how cell type identity contributes to cortical function it is necessary to accurately characterize the precise ways that neurons connect to one another at the level of cell types. Prior work has revealed that the majority of synaptic connections in the neocortex are made between neighboring neurons that compose local microcircuits[7] and the idea of a canonical microcircuit established by layer-specific patterns of excitatory connections predominates much of the literature[8–10]. The idea of canonical circuits is further reinforced by studies that have demonstrated cell-type specificity of cortical connections at the resolution of neuronal subclasses, e.g. cortical layers for excitatory neurons or inhibitory neurons expressing subclass marker proteins. Such studies suggest that parvalbumin (Pvalb) neurons primarily connect to pyramidal cells and each other, somatostatin (Sst) neurons to other inhibitory neurons, but not themselves, and vasoactive intestinal peptide (Vip) neurons to Sst interneurons[11]. Do principles of connectivity established at the level of neuronal classes and subclasses extend to the far greater numbers of neuronal subtypes revealed by single cell transcriptomics? And which, if any, of the different inhibitory neuron subtypes can be distinguished based on their inputs to different classes of excitatory neurons?

Here we introduce a method, Single Transcriptome Assisted Rabies Tracing (START), which combines monosynaptic rabies virus (RV) tracing[12–14] and single-nuclei RNA sequencing (snRNA-seq)[2,15] to identify the transcriptomic cell types that provide monosynaptic inputs to defined populations of neurons. We employ START to characterize the synaptic connectivity of mouse V1 at the level transcriptomic neuronal subtypes defined by single cell gene expression. We conduct retrograde transsynaptic tracing to identify inputs to L2/3, L4, L5 intratelencephalic (IT), L5 extratelencephalic (ET), and L6 cortico-thalamic (CT) excitatory neurons. Using the transcriptome-wide profiles of input neurons we are able to classify them at much finer resolution (transcriptomic subtypes) compared to circuit tracing methods that rely on cell body locations, antibody staining or intersectional genetic approaches[16,17]. At the broader subclass level, START generates results consistent with established circuit tracing results, validating the utility of START as a circuit tracing tool that allows far more precise determination of input cell type identity–and by extension, circuit connectivity. Using START we were also able to uncover subtypes of Sst, Pvalb, Vip, and Lamp5 interneurons that provide selective input to five layer-specific populations of excitatory neurons.

Results

Transcriptomic characterization of rabies labeled input cells

To investigate subtype specific inputs to excitatory neurons in distinct cortical layers of mouse V1 we conducted monosynaptic rabies tracing across multiple layer-specific Cre-driver mouse lines [12] followed by snRNA-seq of rabies infected neurons that provided input to the Cre-expressing starter cells. To restrict initial glycoprotein-deleted RV (RVdG) infection to excitatory "starter neurons" in specific layers, we first injected a Cre-dependent helper adeno-associated virus (AAV) into Sepw1-Cre, Scnn1a-Tg3-Cre, Tlx3-Cre, Npr3-IRES-Cre, and Ntsr1-Cre mice to target L2/3, L4, L5 intratelencephalic (IT), L5 extratelencephalic (ET), and L6 cortical thalamic (CT) excitatory neurons respectively [18]. Pairing of AAV-DIO-TC66T-2A-oG with the Cre-driver mouse lines allows for the selective expression of a mutant TVA receptor, TVA^{66T}, and optimized rabies glycoprotein (oG) in layer specific Cre^+ neurons (Figure 2.1A). TVA is a receptor for the avian sarcoma leucosis virus envelope protein, EnvA, and is necessary for entry of pseudotyped $EnvA^+$ RVdG into Cre^+ cells. The use of mutant TVA^{66T}, with 10% efficiency for viral entry, eliminates Cre-independent background labeling[19], thus making it more suitable for tracing local monosynaptic inputs. (Control experiments verified the absence of leak expression and $EnvA^+$ RVdG infection in the absence of Cre; see Methods). Expression of oG in Cre^+ neurons allows for trans-complementation in $EnvA^+$ RVdG infected neurons, also termed starter cells, allowing the virus to spread retrogradely into presynaptically connected inputs[20]. Importantly, because input neurons lack the glycoprotein required for further retrograde spread, labeling is monosynaptically restricted.

Three weeks after helper virus injection, a variant of EnvA+ RVdG that expresses the mCherry fluorophore tagged with the histone H2B nuclear targeting sequence (EnvA+ RVdG-H2B-mCherry) was injected and allowed to express for 10 days (Figure 1A). Following retrograde spread of RVdG into input neurons, V1 tissue was dissected, and individual rabies-labeled nuclei sorted by flow cytometry (fluorescence-activated nuclear sorting - FANS) (Figure S1.1). Individual nuclei were subjected to snRNAseq using the 10X genomics V3.1 platform

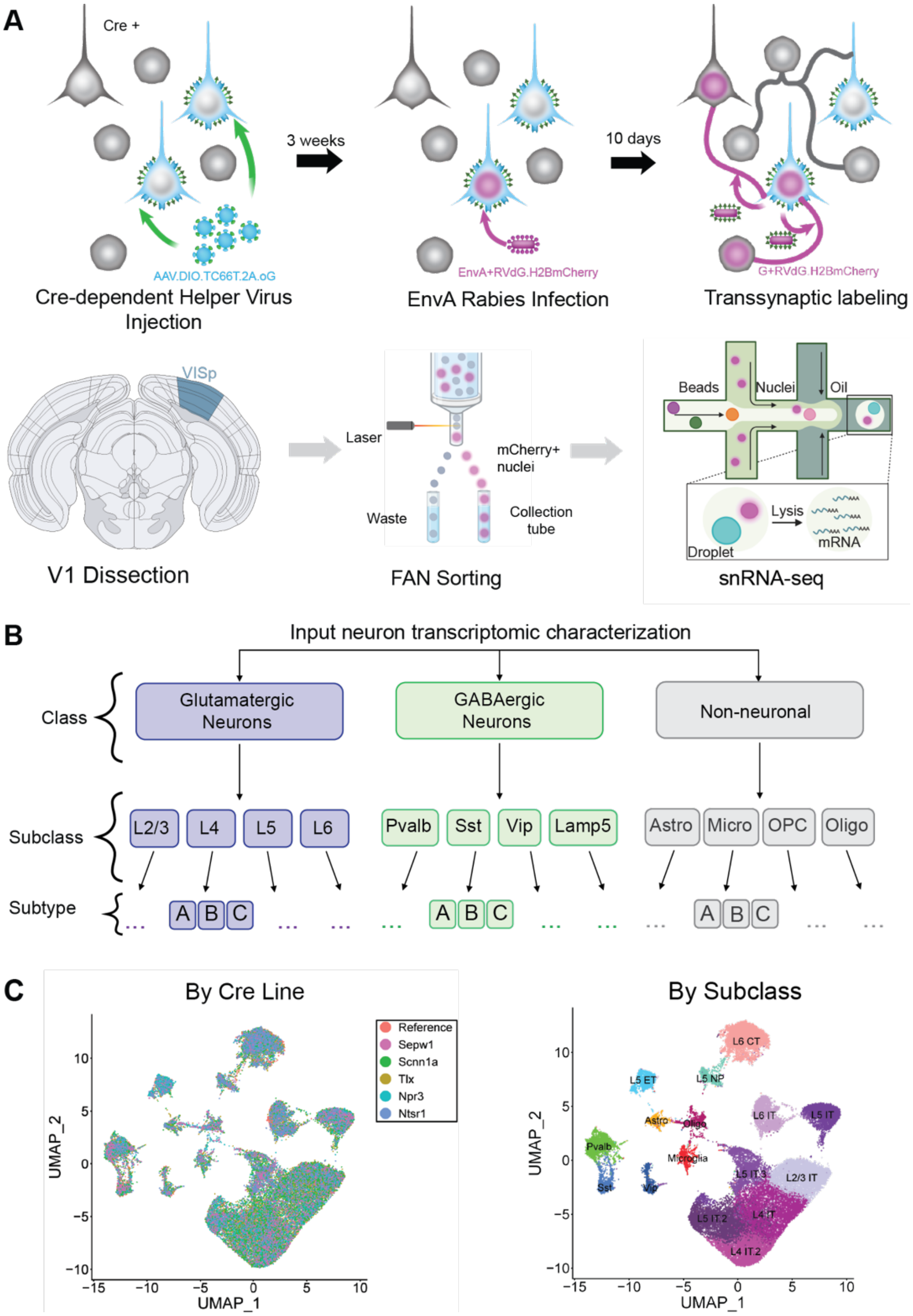

Figure 2.1. Transcriptomic characterization of rabies-labeled input cells.
(A) Monosynaptic rabies tracing of inputs to excitatory neurons in different cortical layers Schematic of experiment workflow. Monosynaptic rabies tracing was performed in Sepw1, Scnn1a, Tlx, Npr3, and Ntsr1 Cre driver mouse lines. Four mice per line were injected with AAV-DIO-TC66T-2A-oG in V1. Three weeks after helper virus injection, EnvA+ RVdG-H2B-mCherry was injected into the same region. 10 days after injection, V1 was dissected and mCherry+ nuclei were collected using FANS. snRNAseq of FANS-sorted nuclei was performed using the 10X Genomics platform. (B) Input neuron transcriptomic characterization. Levels of taxonomy used to transcriptomically identify input neurons (adapted from Cheng et al. 2022). (C) UMAP of 23,940 rabies-labeled nuclei color coded by the Cre-line tracing experiment they were collected from (left) or by subclass identity (right). Data from each line and tracing experiment were analyzed separately and then merged for visualization purposes.

(Figure 2.1A). A total of 23,940 nuclei were sequenced and passed quality control (See Methods) from at least 4 animals of each of the five genotypes (see Table 2.S1).

To transcriptomically classify rabies-labeled input neurons according to established transcriptomic cortical cell types we used SingleR to transfer the taxonomy cell type labels from a reference dataset to the rabies-labeled input neurons. We used a transcriptomic reference dataset composed of uninfected nuclei collected from V1 with cell type annotations established according to the Allen Institute for Brain Science (AIBS) cell type taxonomy[5,21] that has been previously shown to allow accurate characterization of rabies-infected cortical neurons[22].

SingleR was used to conduct supervised label transfer annotation of cell types for its robustness against cell type similarity and increased cell type number compared to other computational methods[23,24]. Input neurons were classified at the class level (glutamatergic, GABAergic, or non-neuronal), subclass level (e.g. L2/3, L4, L5 IT; Sst, Pvalb, Vip; etc.) and at the subtype level (e.g. Sst Chodl, Sst Esm1, etc.) (Figures 2.1B, 2.S2).

Transcriptomic inputs to Excitatory neurons of mouse V1 at subclass resolution

We begin by describing results in which input neurons are classified by their gene expression at the level of subclasses. Because numerous previous studies have described local cortical circuits at this level of resolution, we can compare our results to expectations from those studies before moving to our primary focus on descriptions at the much finer subtype resolution afforded by single cell transcriptomics, particularly for the highly diverse inhibitory neuron subtypes. In particular, previous studies have easily resolved laminar identities of excitatory neurons based on cell body locations, and inhibitory neuron subclasses based on antibody staining or use of subclass-specific Cre driver lines[25–29]. Detailed comparisons between prior

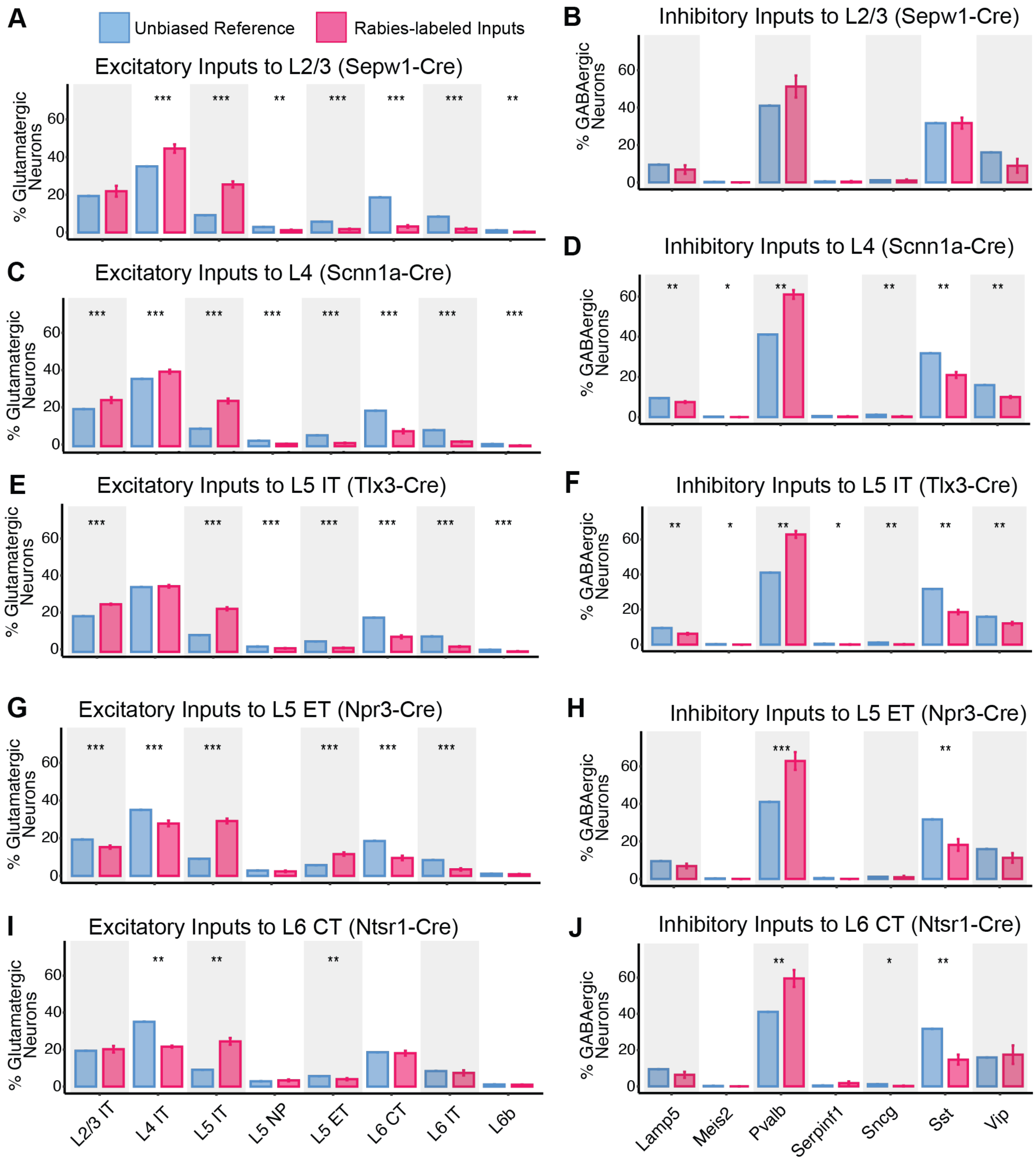

Figure 2.2. Transcriptomic Subclasses Providing Input to Distinct Excitatory Populations in Mouse V1. (A-J). Bar plots comparing proportions of inputs to layer-specific excitatory cell populations from rabies-labeled input neurons and inputs from neurons in an unbiased reference dataset. (A-B) Proportion of input from Glutamatergic (A) and GABAergic (B) cell classes to L2/3 Cre(+) starter cells in the SepW1-Cre mouse line. Red bars indicate proportion of input from rabies-labeled neurons of that subclass and blue bars are the proportions of inputs of the same subclass from the unbiased reference mouse V1. (C-J). Same as (A-B), with excitatory starter cell/output population in L4 using the Scnn1a-Cre mouse line (C-D), L5 IT using the Tlx3-Cre mouse line (E-F), L5 ET using the Npr3-Cre line (G-H), and L6 CT using the Ntsr1-Cre line (I-J). P values were determined by Wilcoxon rank-sum test and adjusted for multiple comparisons using Benjamini–Hochberg method. ns: $p > 0.05$, *: $p <= 0.05$, **: $p <= 0.01$, ***: $p <= 0.001$. Error bars indicate s.e.m.

studies and across our results are reserved for consideration in the supplemental results. Here we note that all of our observations at the subclass level are consistent with expectations from prior knowledge and we highlight just a few of those observations.

Figure 2.1 shows results of START experiments with input neurons assigned to their subclass identities. Input neurons are first separated into excitatory and inhibitory classes and then analyzed independently at the level of subclasses. Direct comparisons should not be made between results from different mouse lines due to systematic differences in the numbers of starter cells between mouse lines. Furthermore, while quantitative comparisons between the numbers/proportions of different input cell types are meaningful for inferring likely functional impact of each input population onto a given starter cell population, statistical differences are expected to be largely reflective of the different numbers of neurons of each type that are present in the cortex. For example, there are far more L4 excitatory neurons than other excitatory subclasses and far more Pvalb than other inhibitory subclasses. Therefore, to assess the prevalence with which different input cell types might selectively connect to each starter cell population we compared input cell type distributions to expectations from an "unbiased" reference data set.

For each Cre-driver line, the proportions of excitatory or inhibitory input neurons were calculated and compared to the expected proportions from a mouse V1 snRNAseq reference data set in which an unbiased collection of neurons was evaluated. Statistical differences between the experimental samples (Figure 2.2, red bars) and the reference sample (Figure 2.2, blue bars) were evaluated using a Monte Carlo analysis, repeatedly sampling randomly a number of neurons from the reference set that matches the size of the relevant experimental sample and then comparing the value from the experimental sample to the distributions from the random sampling (See Methods).

At the subclass level the proportions of excitatory input neurons from each subclass vary between mouse lines, largely reflecting the known laminar specificity of the axonal projections from each cell type. For example, L4 IT neurons are over-represented in the inputs to L2/3 and underrepresented in the in the inputs to L5 ET and to L6 CT neurons, reflecting the strong feedforward nature of L4 → L2/3 circuits and the more extensive axonal arbors from L4 IT neurons into L2/3 than to deeper layers[30,31]. (Note that values from the starter cell layer reflect a mixture of both starter cells and input cells and should not be interpreted as a simple reflection of relative input strength, while comparisons between cell classes outside the starter cell layer are more meaningful.) In addition to evaluating interlaminar connectivity between excitatory neurons, prior studies have shown cell type specificity of L5 intralaminar connections, with L5IT neurons having a 3-fold higher probability of connecting to L5 ET neurons than for connections from L5ET to L5 IT neurons[32,33]. Accordingly, results from L5ET starter cell tracing shows a highly significant enrichment of inputs from L5IT neurons (3.39-fold increase: 26.56% of glutamatergic inputs versus 7.845% in control dataset, P<.001), while inputs from L5ET cells onto L5 IT starter neurons are significantly impoverished (41.5% reduction: 2.029% of glutamatergic inputs versus 4.884% in control dataset, P<.001).

In contrast to excitatory inputs, inhibitory inputs at the subclass level were remarkably similar across mouse lines. As a general rule, Pvalb inputs were over-represented while Vip and Sst were under-represented. This trend reflects the known propensity observed in paired recordings from brain slices for Pvalb basket cells to connect at very high rates to their neighboring pyramidal neurons, while Sst cells connect with about 5-fold lower probability, and Vip cells preferentially target Sst cells rather than pyramidal neurons[11,34].

A benefit of mapping transcriptomic inputs to excitatory neurons is that we can compare the finding revealed using START to other methods that have been used to examine this circuitry across distinct cortical areas, albeit at coarser resolutions[17,35–39]. We conducted rabies tracing as described above using Sepw1-Cre to restrict starter cells to L2/3 excitatory neurons. After transcriptomically characterizing input cells, for each experimental animal (n=4, 1 male, 3 females) we calculated the number of inputs belonging to distinct neuronal subclasses as a fraction of the total neuronal inputs. At this resolution, we can better compare the proportions of inputs to prior findings. Furthermore, to determine whether certain subclass and subtypes were over or underrepresented in inputs to cortical L2/3–L6 we compared the proportions obtained to a computed estimate of the prevalence of distinct cell types in wild-type control mouse V1.

After transcriptomically characterizing input cells to L2/3 we first calculated the proportion of rabies-labeled inputs belonging to distinct neuronal subclasses as a percent of the total neuronal inputs, allowing us to determine what proportions of distinct subclasses provide input to L2/3. We found that L4 IT neurons make up about 40% of all neuronal input to L2/3, whereas L5 IT neurons make up about 20% of all neuronal inputs. Overall, these results align with previous work suggesting that most inputs are from L4 and L5 and very few from L6[26,27,40-44].

We then calculated the prevalence of specific cell subclasses in mouse V1 in the absence of circuit tracing. To obtain a measure of the likely prevalence of cell types, we performed 10,000 iterations of random sampling from a control dataset composed of nuclei collected from V1 from an uninjected wild-type mouse. The collected nuclei should be representative of the amount or prevalence of subclasses found in mouse V1 (Figure 2.2). This second measure allows us to determine whether certain subclasses were enriched or underrepresented in inputs to L2/3 compared to the unbiased sample. For example, even though L5IT neurons account for less than 10% of neurons in the unbiased sample shown in blue, they make up 20% of neuronal inputs to L2/3, a more than 2-fold enrichment of this subclass in inputs to L2/3.

On a broader scale, we found that excitatory L4 IT excitatory neurons were significantly overrepresented in rabies-labeled inputs to L2/3 compared to baseline prevalence (39.38% vs 30.21% respectively, p = 0.002; Figure 2.2A), largely in agreement with previously reported connectivity[36–38]. Conflicting findings have been reported regarding excitatory projections from L5 to L2/3, with certain studies observing sparse connectivity[37,45,46] and others reporting a high number of excitatory L5 projections to L2/3[36,39]. We observed an overrepresentation of L5 IT neurons (22.56% vs 7.84%. p = 0.002; Figure 2.2A) in rabies-labeled inputs to L2/3. On the other hand, L5 ET and L5 near-projecting (NP) neurons were underrepresented (1.51% vs 4.88%. p = 0.002 and 1.06% vs 2.44%, p = 0.003 respectively; Figure 2.2A). Excitatory L6 CT, L6 IT, and L6b were all underrepresented in rabies-label input neurons (2.8% vs 16%, p = 0.002; 1.64% vs 7.22%, p = 0.002; 0.31% vs 0.97%, p = 0.0048 respectively; Figure 2.2A).

Descriptions of inputs from inhibitory cell subclasses to L2/3 pyramidal neurons have previously been reported; however, these approaches largely fail to separate the major inhibitory cell subclasses (Sst, Pvalb, Vip) on a finer scale[17,36]. We therefore sought to comprehensively examine inhibitory inputs to L2/3 at the much more precise resolution conferred by transcriptomic characterization. Specifically, we investigated whether L2/3 excitatory neurons receive differential input from distinct inhibitory subtypes. We calculated the number of inputs belonging to distinct inhibitory subtypes as a fraction of the total inputs from the corresponding subclass.

Like our current understanding of L2/3 local connectivity, our knowledge of local inputs to L6 CT excitatory neurons is limited to broad classifications of inputs[17,35,39]. At the subclass level, we observed an overrepresentation of L5 IT neurons (22.83% vs 7.85%, p = 0.0023) and an underrepresentation of L4 IT (20.17% vs 30.21%, p = 0.0023) and most inhibitory neuron subclasses (Figure 2.3A). At the subtype level two Pvalb subtypes and one Sst subtype were enriched in inputs to L6 CT (Figure 2.3B and 2.3C). Both enriched Pvalb subtypes, Pvalb Sema3e Kank4 (18.68% vs 7.97%, p = 0.01) and Pvalb Gpr149 Islr (17.95% vs 9.53%, p = 0.03) have axons targeting deep cortical layers[47]. Conversely, Pvalb Tpbg, which was overrepresented in inputs to L2/3, was underrepresented in inputs to L6 CT (12.16% vs 20.7%, p = 0.03). The Sst Chodl subtype was the only Sst subtype significantly overrepresented in input to L6 CT (19.35% vs 1.68%, p = 0.005). The Sst Chodl subtype corresponds to long-range projecting non-Martinotti inhibitory interneurons that are found primarily in deeper layers[47–51]. Multiple Sst subtypes had sparse representation in L6 CT inputs including: Sst Chrna2 Glra3, Sst Chrna2 Ptgdr, Sst Hpse Cbln4, and Sst Tac2 Tacstd2.

Inputs from Pvalb cell subtypes

Parvalbumin-expressing cells represent one of the primary inhibitory cell subclasses in cortex. Because Pvalb basket neurons synapse primarily on the somata of their target cells, the laminar targets of basket cells with known laminar positions and layer-restricted axonal arbors can be predicted[52,53]. These properties correspond to some Pvalb subtypes, making the laminar excitatory neuron targets of such cells predictable from their morphologies alone. Using START

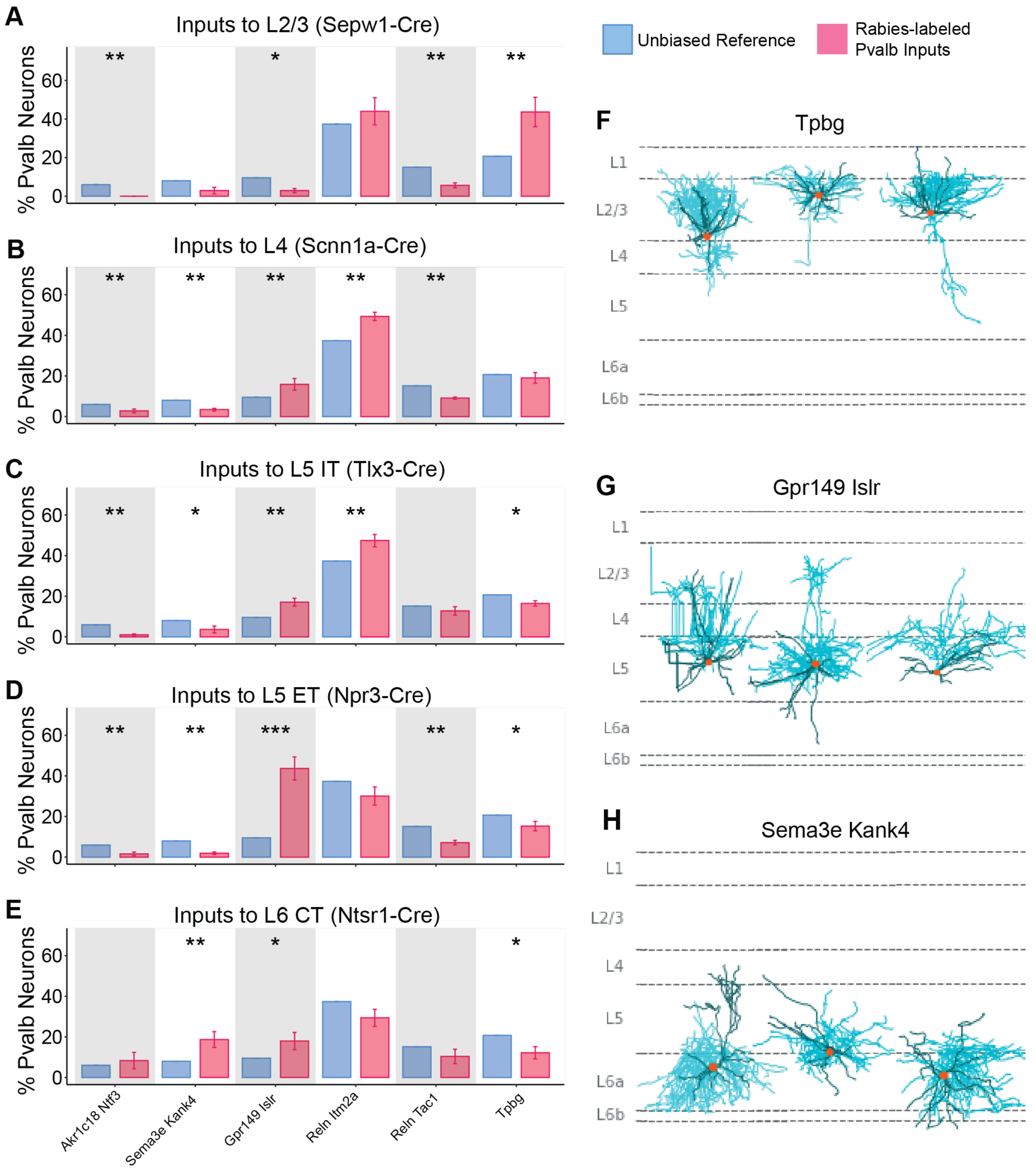

Figure 2.3. Transcriptomic Pvalb Subtypes Providing Input to Distinct Excitatory Populations in Mouse V1. (A-E). Bar plots comparing proportions of inputs to layer-specific excitatory cell populations (mouse Cre starter cell line) between rabies-labeled Pvalb-expressing neurons (red bars) and Pvalb-expressing neurons from an unbiased reference dataset (blue bars). Data are plotted by Pvalb transcriptomic subclass (T type, Allen Cell Types Database). Subclasses constituting <.5% of all GABAergic neurons were defined as rare cell types and omitted from analysis. P values were determined by Wilcoxon rank-sum test and adjusted for multiple comparisons using Benjamini–Hochberg method. *: $p <= 0.05$, **: $p <= 0.01$, ***: $p <= 0.001$. Error bars indicate s.e.m. (F-H). Reconstructions for 3 example filled cells belonging to Pvalb Tpbg (F), Pvalb Gpr149 Islr (G), and Pvalb Sema3e Kank4 (H) subclasses, adapted from the Allen Brain Map Cell Types Database. Dendrites are in dark green, and axons are cyan.

we can confirm the presence of these monosynaptic connections as well as reveal connectivity of other cell types. Quantification of layer-specific inputs from PV cells confirmed this hypothesis and further demonstrated that rabies does not spread retrogradely in the absence of synaptic input. Furthermore, we saw specificity of inputs from cell types that could not be predicted from overlap of axons and cell bodies.

Within the Pvalb subclass, we found one subtype that was overrepresented and three subtypes that were underrepresented in its inputs to specific cortical layers. The Pvalb Tpbg subtype was significantly enriched compared to its prevalence in control mouse V1 (43.65% vs 20.7%, p = 0.015; Figure 2.2B). Pvalb Tpbg interneurons predominantly reside in and send extensive axonal projections within L2/3[47]. Pvalb Akr1c18 Ntf3, Pvalb Gpr149 Islr, and Pvalb Reln Tac1 were all underrepresented in Pvalb inputs to L2/3 (0% vs 5.99%, p = 0.015; 2.94% vs 9.55%, p = 0.022; and 5.67% vs 15.07%, p = 0.015; Figure 2.2B). Pvalb Reln Tac1 has been found to correspond to fast-spiking cells with L5-dominant axon innervation. Similarly Pvalb Akr1c18 Ntf3 and Pvalb Gpr149 Islr send extensive axonal projections to deep layers, but largely avoid L2/3[47]. When examining Pvalb inputs to L6CT we found two enriched subtypes, Sema3e Kank4 and Gpr149. These subtypes each account for about 20% of all Pvalb inputs, even though they are found at much lower proportions in unbiased (control) tissue. Pvalb Tpbg, a subtype enriched with enriched input to L2/3 excitatory neurons, is underrepresented in its inputs to L6 corticothalamic neurons, accounting for about 10% of inputs compared to 20% in the unbiased sample (Figure 2.3E). This result accords with a previous finding from Allen Institute illustrating an overrepresentation of Pvalb-expressing cells in inputs to L2/3.

Inputs from SST subtypes

While layer-specific input may be inferred from morphological reconstructions of Pvalb neurons whose dendrites primarily target somata, it is more difficult to predict connectivity from anatomical overlap in somatostatin-expressing (SST) cells which typically synapse on distal regions of the recipient dendritic arbor[54]. START enables us to observe inputs from somatostatin-expressing neurons to layer-specific excitatory populations in the absence of anatomical data. Targeted recordings of Sst-expressing interneurons spanning cortical layers reveal differential patterns of functional connectivity and behavior-dependent activity changes, suggesting the presence of laminarly-defined Sst subtypes and subtype-specific circuits[54–56].

Within the Sst subclass, we found 2 subtypes that were overrepresented and two subtypes that were underrepresented in their inputs to L2/3. Sst Mme Fam114a1, one of the enriched Sst subtypes exhibiting more than a 2-fold difference between inputs to L2/3 and unbiased sample (19.26% vs 4.81%, p = 0.013; Figure 2.2C), has been found to send axons to L1 (Martinotti-like), but additionally is characterized as having axonal projections that split evenly across two distinct layers[47]. We found cells of this type were overrepresented in their input to superficial layers and underrepresented in their input to deep layers. Sst Esm1, the other overrepresented subtype (9.67% vs 1.9% of Sst neurons in unbiased sample, p = 0.048; Figure 2.4), is found primarily in L5 and interestingly sends projections primarily to deeper layers and have few projections to superficial layers[47]. Sst Chrna2 Glra3 and Sst Chrna2 Ptgdr were both underrepresented in Sst inputs (0% vs 7.89%, p = 0.039 and 0% vs 7.28%, p = 0.039; Figure 2.4). Although both subtypes that are underrepresented avoid axonal projections to L2/3, they do project to layer 1 where L2/3 neuron dendrites are found.

If we compare our data to Patchseq data from the Allen Institute[3,57], we can start to appreciate how our finding would have been difficult to arrive at if using morphological

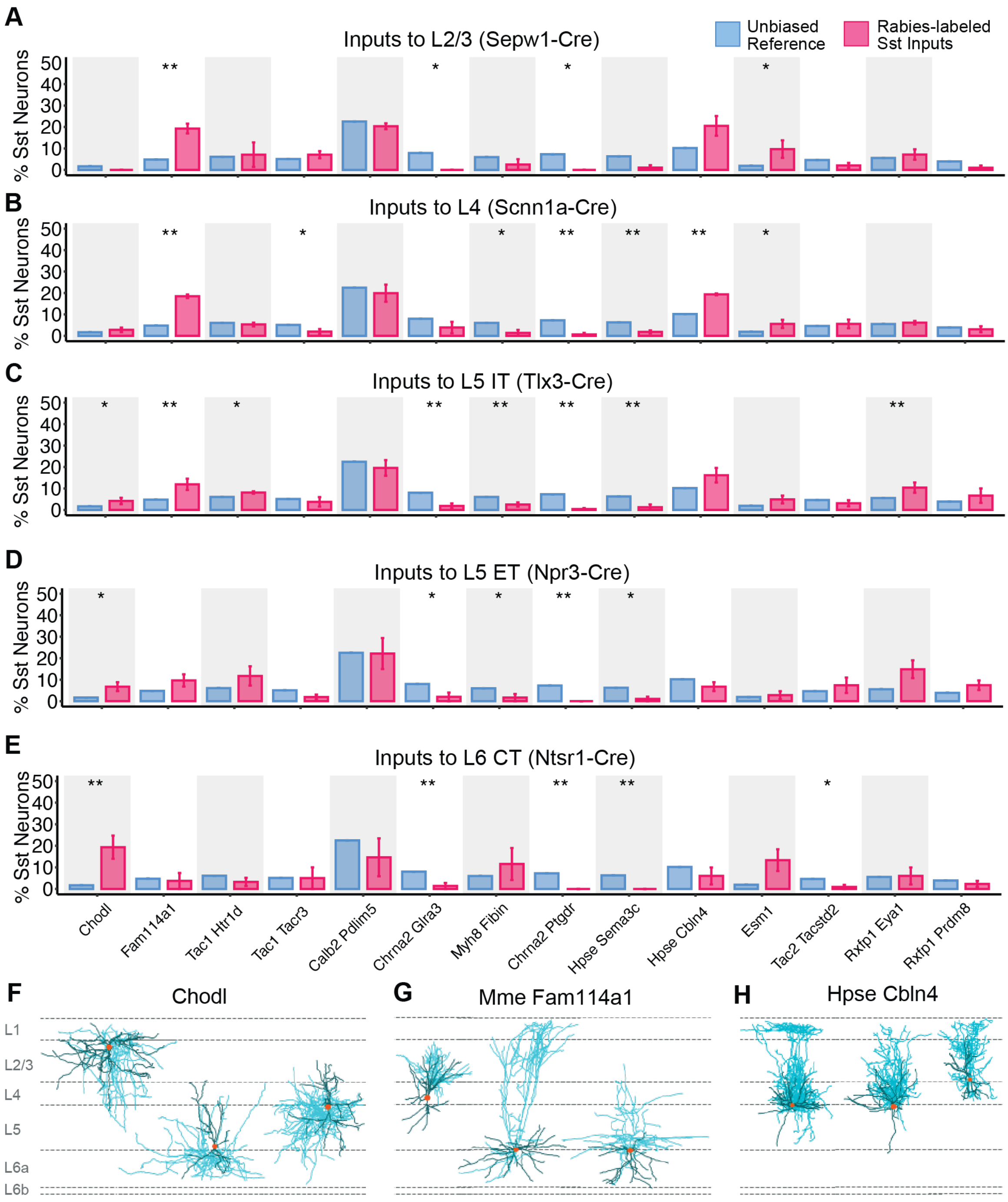

Figure 2.4. Transcriptomic Sst Subtypes Providing Input to Distinct Excitatory Populations in Mouse V1. (A-E). Bar plots comparing proportions of inputs to layer-specific excitatory cell populations (Cre starter lines) between rabies-labeled Sst-expressing neurons (red bars) and Sst-expressing neurons from an unbiased reference dataset (blue bars). Data are plotted by Sst transcriptomic subtype (T type, Allen Cell Types Database). Subtypes containing <.5% of all GABAergic neurons in the control dataset were classified as rare and omitted from analysis (see Methods). P values were determined by Wilcoxon rank-sum test and adjusted for multiple comparisons using Benjamini–Hochberg method. *: $p <= 0.05$, **: $p <= 0.01$, ***: $p <= 0.001$. Error bars indicate s.e.m. (F-H). Reconstructions for 3 example filled cells belonging to Sst Chodl (F), Sst Mme Fam114a1 (G), and Sst Hpse Cbln4 (H) subclasses adapted from the Allen Brain Map Cell Types Database. Dendrites are in dark green, and axons are in cyan.

reconstructions alone. For example, while Sst Mme neurons (which are overrepresented in our experiment) have axons projecting to L2/3 they also have axons projecting to L5. Moreover, using START we can verify that Sst Mme axons in L2/3 are in fact providing input to L2/3 excitatory neurons specifically, rather than to cells in other cortical layer that happen to have dendrites in layer 2/3 as might have been predicted from morphological reconstructions.

Since L6 CT neurons have extensive dendrites in layer 5[58,59], they could have received input from any of these subtypes at that location. However, our data suggest L5-specific excitatory subtypes are not monosynaptically connected to L6 CT neurons. Interestingly, we found that the most prevalent subtype providing input to L6CT is the rare Sst Chodl type (Figure 2.4C) which corresponds to the nitric oxide synthase positive, long-range projecting inhibitory interneurons that have been implicated in sleep regulation[49]. Sst Chodl is found in all layers and sends axons to all layers, thus the connection between this subtype and L6CT could not have been easily predicted without START.

The Allen Institute has data on morphology and functional properties of distinct transcriptomic neurons through their Patchseq work that suggests that transcriptomically-defined clusters are more meaningful in cell type classification than morpho-electrical types[47]. When we compare our results with morphological reconstructions from distinct transcriptomic cell types from the Allen Institute, we find broad consistencies between datasets. For example, we found an overrepresentation of Pvalb Tpbg inputs to L2/3 pyramidal cells, in alignment with the Allen data showing that Tpbg neurons have axons projecting extensively to L2/3[47]. On the contrary, Pvalb Akr1c18 neurons (an underrepresented subtype in our tracing experiments) have axons primarily in L5 and L6 and almost none in L2/3. Broadly, START generated results consistent with established circuit models, validating its utility as both a circuit-tracing tool and a means of

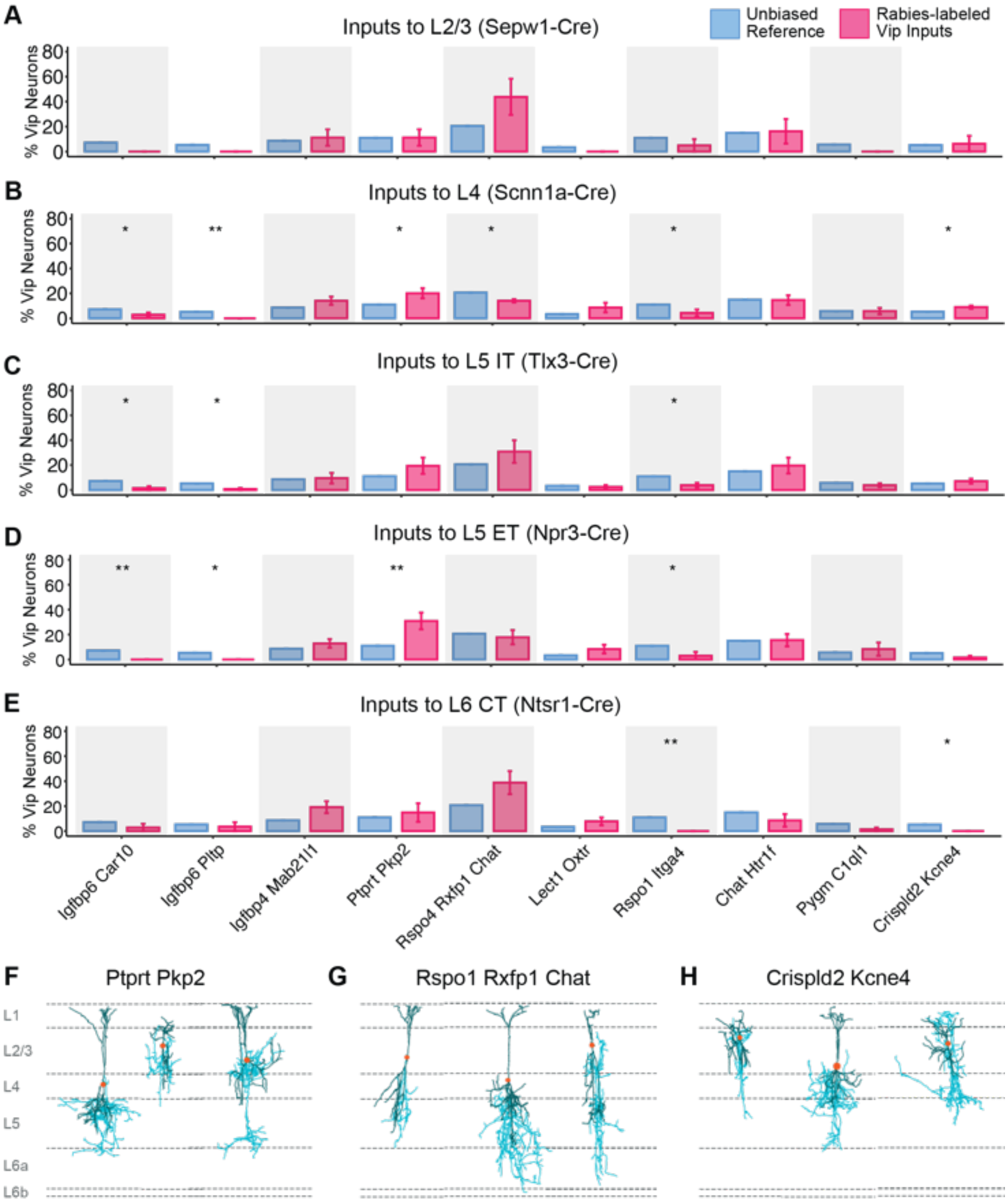

Figure 2.5. Transcriptomic Vip Subtypes Providing Input to Distinct Excitatory Populations in Mouse V1. (A-E). Bar plots comparing proportions of inputs to layer-specific excitatory cell populations (Cre starter lines) between rabies-labeled Vip-expressing neurons (red bars) and Vip-expressing neurons from an unbiased reference dataset (blue bars). Data are plotted by Vip transcriptomic subtype (T type, Allen Cell Types Database). Subtypes containing <.5% of all GABAergic neurons in the control dataset were classified as rare and omitted from analysis (see Methods). P values were determined by Wilcoxon rank-sum test and adjusted for multiple comparisons using Benjamini–Hochberg method. *: p <= 0.05, **: p <= 0.01, ***: p <= 0.001. Error bars indicate s.e.m.(F-H). Reconstructions for 3 example filled cells belonging to Vip Ptprt Pkp2 (F), Vip Rspo1 Itga4 (G), and Vip Crispld2 Kcne4 (H) subclasses, adapted from the Allen Brain Map Cell Types Database. Dendrites are in dark green, and axons are cyan.

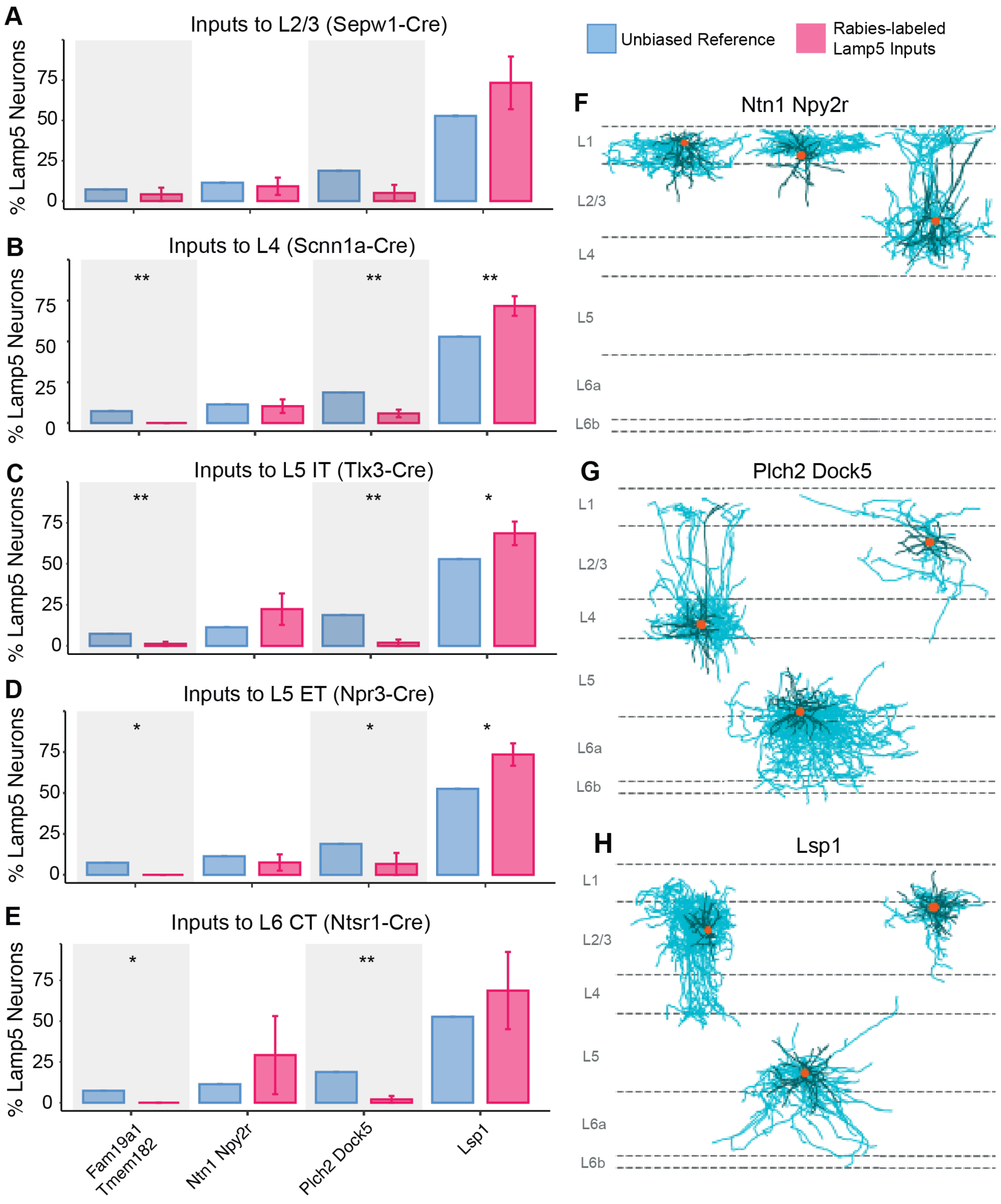

Figure 2.6. Transcriptomic Lamp5 Subtypes Providing Input to Distinct Excitatory Populations in Mouse V1. (A-E). Bar plots comparing proportions of inputs to layer-specific excitatory cell populations (Cre starter lines) between rabies-labeled Lamp5-expressing neurons (red bars) and Lamp5-expressing neurons from an unbiased reference dataset (blue bars). Data are plotted by Lamp5 transcriptomic subtype (T type, Allen Cell Types Database). Subtypes containing <.5% of all GABAergic neurons in the control dataset were classified as rare and omitted from analysis (see Methods). P values were determined by Wilcoxon rank-sum test and adjusted for multiple comparisons using Benjamini–Hochberg method. *: $p <= 0.05$, **: $p <= 0.01$, ***: $p <= 0.001$. Error bars indicate s.e.m. (F-H). Reconstructions for 3 example filled cells belonging to Lamp5 Ntn1 Npy2r (F), Lamp5 Plch2 Dock5 (G), and Lamp5 Lsp1 (H) subclasses, adapted from the Allen Brain Map Cell Types Database. Dendrites are in dark green and axons in cyan.

delineating cell type based on their anatomical input. START thereby permits more precise determination of cell type identity in the context of its circuitry than can be achieved by anatomical tracing or transcriptomic characterization alone.

Inputs from Vip and Lamp5 Subtypes

As Vip and Lamp5 neurons are much rarer and comprise a smaller subset of interneurons than Pvalb and Sst, we found fewer and less dramatic over- and underrepresentations of these subtypes in their laminar input distribution vs. the reference dataset. We found consistent underrepresentations of Vip Igfbp6 Car10, Igfbp6 Pltp, and Rspo1 Itga4 subtypes in their inputs to all 5 layer-specific pyramidal populations (Figure 2.5) while the Vip Ptprt Pkp2 subtype was significantly overrepresented in its inputs to middle cortical layers. Because Vip neurons provide substantial inputs to Sst neurons[11], we suspect that the underrepresented subtypes may instead be providing intracortical input to other inhibitory classes instead. We also found that the Lamp5 subtypes Fam19a1 Tmem182 and Plch2 Dock5 were significantly underrepresented in their inputs to all cortical layers except L2/3, the Lamp5 Lsp1 subtype was overrepresented in inputs provided across all cortical layers (Figure 2.6).

Discussion

The recent surge in novel transcriptomic technologies has enabled our ability to characterize neural cell types based on their gene expression patterns[4,60–64], facilitating work towards the creation of a catalog of the cellular building blocks that make up the mammalian brain. However, cells do not function in isolation and our newfound understanding of neural diversity has generated new questions regarding connectivity principles at the level of transcriptomic cell types. Here we present START, a new technical approach for coupling circuit connectivity tracing with transcriptomic classification of neural cells, and use START to investigate interlaminar synaptic connectivity of mouse V1. By conducting our analysis at multiple levels of cell type granularity (subclass and subtype) we were able to compare subclass level results to prior published work and establish START's utility as a circuit tracing tool. More importantly, with the more precise neural characterization achievable with START we were able to uncover new circuit connectivity motifs between inhibitory subtypes and excitatory neurons in distinct layers.

Of course, gene expression alone is insufficient as a metric for delineating neuronal subtypes. Cells can have different patterns of gene expression but the same function, and cells assigned to the same transcriptomic cluster can often be further separated based on their anatomical projection patterns, functional connectivity, and intrinsic physiology[1]. Thus, in order to more comprehensively understand the nuances of cell type specification it is necessary to acknowledge and incorporate additional metrics of connectivity and physiology into genomic sequencing analysis. Despite these limitations, START serves as an important step toward the development of novel functional and behavioral studies exploring the contribution of genetically-defined, cortical layer-specific inputs to fundamental circuitry underlying sensory information processing.

Methods

Mouse Transgenic Lines

All experimental procedures were approved by the Salk Institute Animal Care and Use Committee. C57BL/6J mice were used as wild-type. GENSAT BAC transgenic Sepw1-Cre

NP39, Scnn1a-Tg3-Cre, Tlx3-Cre PL56, Npr3-IRES-Cre-neo, and Ntsr1-Cre GN220 mice have been previously described[29,65,66]. Transgenic mice were maintained on C57BL/6J backgrounds. Mice were housed with a 12-hour light and 12-hour dark cycle and *ad libitum* access to food and water. Both male and female mice were used for RNA sequencing experiments.

Virus Preparation

AAV8-DIO-TC66T-2A-oG (4.31E+13 GC/mL) and EnvA+RVdG-H2BmCherry (7.43E+07 GC/mL) were produced by the Salk GT3 Viral Core. Prior to injection, AAV8-DIO-TC66T-2A-oG was diluted 1:10 in PBS for a final titer of 4.31E+12 GC/mL.

Animal Surgery for Virus Injection

For rabies input tracing transgenic mice received AAV helper injections at P49 – P60. Mice were initially anesthetized with 2% isoflurane and maintained at 1.5% isoflurane after placement on a stereotax (David Kopf Instruments, Model 940 series) for surgery and stereotaxic injections. A small craniotomy was made with a mounted drill over the primary visual cortex of the left hemisphere using the following coordinates: 3.4 mm posterior and 2.6 mm lateral relative to bregma. 100 nL of diluted AAV8-DIO-TC66T-2A-oG (4.31E+12 GC/mL, Addgene # 178430) was injected into the center of V1 0.5–0.7 mm ventral from the pia using a pulled glass pipette with a tip size of 30 um connected to a 1ml syringe with 18G tubing adaptor and tubing. To prevent backflow, the pipette was left in the brain for 5 minutes after injection. Three weeks after AAV helper virus injection, 200 nL of EnvA+RVdG-H2BmCherry (7.43E+07 IU/ml) was injected into the same site in V1. After recovery, mice were given water with ibuprofen

(30mg/kg) and housed for 10 days before tissue harvest to allow for fluorescent protein expression.

Brain Dissection and Single Nuclei Isolation

Ten days after rabies injection, animals were euthanized with an overdose of isoflurane. Brains were extracted and immediately submerged in ice-cold slicing solution (2.5mM KCl, 0.5mM CaCl2, 7mM MgCl2, 1.25mM NaH2PO4, 110mM sucrose, 10mM glucose and 25mM NaHCO3) that was bubbled with carbogen. Coronal brain slices (400um thick) were cut using VF-300 Compresstome^{TM} (Precisionary Instruments, Greenville, NC) and submerged in ice-cold slicing solution. Subregions of V1 containing mCherry+ nuclei in brain slices were micro-dissected out under a fluorescent dissection microscope (Olympus SZX6) and transferred to microcentrifuge tubes and immediately frozen in dry ice, and subsequently stored at -80°C. The remaining brain slices after dissection were collected, fixed with ice-cold 4% PFA overnight, stained with DAPI, and scanned with a 10x objective to validate correct V1 dissection using an Olympus BX63 Microscope.

Single nuclei preparations were performed following a published protocol (Lacar et al., 2016) with modification. In summary, the frozen brain tissues were transferred to pre-chilled dounce homogenizers with 1ml NIM buffer (0.25M sucrose, 25mM KCl, 5mM MgCl2, 10mM Tris-HCl (pH7.4), 1mM DTT (Sigma 646563), 10ul of protease inhibitor (Sigma P8340), 1.5ul of RNasin Plus RNase inhibitor (Promega, N2611)), 0.1% Triton X-100, and 10 uM DAPI, and gently homogenized on ice with ice-cold pestles 10 - 15 times. The homogenate was transferred to pre-chilled microcentrifuge tubes and centrifuged at 1000 rcf for 8 min at 4°C to pellet the nuclei. The supernatant was aspirated, the pellet gently resuspended in ice-cold 1ml NIM buffer, and again centrifuged at 1000 rcf for 8 min at 4°C. The pellet was then resuspended in 450ul of nuclei storage buffer (0.25M sucrose, 5mM $MgCl_2$, 10mM Tris-HCl (pH7.4), 1mM DTT, 9ul of Protease inhibitor), and filtered through a 40μM cell strainer. The sample was incubated with 50ul of nuclease-free BSA to prevent nuclei clumping.

Fluorescence-activated nuclei sorting of single nuclei was performed using a FACS Aria Fusion sorter with a 70 μM nozzle at 22.5 PSI sheath pressure. DAPI+/mCherry+ rabies-infected nuclei were sorted into 0.2ml Eppendorf PCR tubes and immediately loaded onto the 10X Genomics Chromium Controller. Biological replicates were processed on different days.

10x Chromium RNA-Sequencing

For 10x processing, we used Chromium Next GEM single-cell 3' Kit (v3.1 Dual Index) and Chromium Next GEM single-cell 3' LT Kit (v3.1 Dual Index) (10x Genomics, PN-1000127 and PN-1000325). We followed the manufacturer's instructions for single-cell capture, barcoding, reverse transcription, cDNA amplification, and library construction. We targeted sequencing depth of about 100,000 reads per cell. Pooled libraries were sequenced on Illumina NovaSeq^{TM} 6000 Sequencing System (S4) and raw read (fastq) files were aligned to the mouse pre-mRNA reference transcriptome (mm10) using the 10x Genomics CellRanger pipeline (version 6.0.). Intronic reads were included in expression quantification using the include-introns parameter.

RNA-seq data quality control and cell-type annotation

Reference data used in this study includes 10x v3 single nucleus RNA-seq from primary visual cortex obtained from the Allen Institute for Brain Science (AIBS, GSE196771). Reference

10x v3 nuclei were assigned to previously published primary visual cortex cell type taxonomy[5] using a nearest centroid classifier based on a set of 563 markers that were detected in both datasets (expression > 0). To estimate the robustness of mapping, classification was repeated 100 times, each time using 80% of randomly sampled markers, and the probability for each cell to map to every reference cluster was computed. R (version 4.1.1), Seurat (version 4.0)[67,68] and SingleR (version 4.1)[23] were used for snRNA-seq analysis. Doublets were identified using DoubletFinder[69] and excluded from analysis. The percentage of mitochondrial transcripts for each nucleus was calculated and added as metadata to the Seurat object using percent.mito. Nuclei with less than 500 genes, more than 8000 genes, and greater than 0.5% of mitochondrial genes were excluded from analysis.

SingleR was used for supervised labeled transfer of class, subclass, and subtype taxonomy from the reference dataset to rabies-labeled input neurons. To decrease supervised annotation performance susceptibility to the effects of large subtype numbers, cell type similarity, and rare cell type detection we employed pseudo-bulk aggregation of reference cells within specific subtype labels[24]. After log-normalization and principal components analysis, k-means clustering within each subtype label is performed to create pseudo-bulk reference samples that preserve the label's internal distribution. To classify rabies-labeled input neurons the Spearman correlation between each rabies-labeled input neuron's expression profile and that of each reference sample is computed. This process is performed iteratively, rerunning the correlation analysis but using only the top cell types from the previous step until only one cell type annotation remains. At each iteration only the variable genes between the top cell types are used to differentiate between closely related cell types. Poor quality or ambiguous assignments were determined according to the per-cell delta score, which is the difference between the score for the assigned label and the median across all labels for each cell. Low deltas indicate an uncertain assignment and high deltas score indicate a high confidence assignment. Cells with small deltas that were outliers compared to other annotated cells in that label were excluded from further analysis.

We compared the proportion of rabies-labeled input neurons corresponding to distinct transcriptomic subtypes to the prevalence of those subtypes in wild-type control mouse V1. To obtain a comparable measure of the likely prevalence of any given subtype we first performed random sampling from the control dataset, where the number of cells sampled (n) = the average number of input cells obtained across mice within a Cre-mouse line (4 mice per line). 10,000 iterations of random sampling of n cells were performed independently for each Cre-mouse line. Random sampling was performed against each Cre driver mouse line used, with sampling size equal to the average number of neurons (nuclei) obtained across animals from that line. We used this as a measure of cell type prevalence across cortex on both a subclass and subtype level. The prevalence of a given subtype was reported as the mean of the subtype proportion across all 10,000 iterations. This mean was compared to the proportion mean obtained across 4 animals in each set of rabies tracing experiments. Statistical significance was assessed by Wilcoxon rank-sum test with Benjamini–Hochberg correction for multiple comparison using R. Not significant (ns): $P > 0.05$, $^{*}P \leq 0.05$, $^{**}P \leq 0.01$, $^{***}P \leq 0.001$, $^{****}P \leq 0.0001$.

Rare cell type classification and exclusion

Cell subclasses with $n<7$ cells assigned were classified as “rare” subtypes; this is equivalent to .5% of all inhibitory neurons in our reference control dataset (see Table 2.S2).

Appendix

Table 2.S1. Total nuclei isolated from each Cre-dependent mouse line. Mouse line shown in left column; a total of 21 mice were used across all experiments. Total cells from each line shown in right column.

Mouse Line	# mice	Excitatory	Inhibitory	Total # cells
SepW1	4	1713	217	1930
Scnn1a	4	11412	1005	12417
Tlx	4	10660	839	11499
Npr3	5	4393	433	4826
Ntsr1	4	4714	331	5045
Totals	**21**	**32892**	**2825**	**35717**

Table 2.S2. Cell counts from Allen Brian Atlas RNAseq Reference dataset. Subclasses shown in gray were non-neuronal and therefore not included in analysis. Total cell counts listed in bottom rows.

Reference Dataset: Cell Counts by Subclass					
Excitatory	**Count**	**Inhibitory**	**Count**	**Other***	**Count**
L2/3 IT	1575	Lamp5	123	Astro	18
L4 IT	2857	Meis2	3	Endo	1
L5 IT	742	Pvalb	536	Microglia	41
L5 NP	232	Serpinf1	6	NA	14992
L5 PT	462	Sncg	15	Oligo	6
L6 CT	1510	Sst	414	OPC	8
L6 IT	681	Vip	208	VLMC	1
L6b	91	**Total**	**1305**	**Total***	**15067**
Total	**8150**	*excluded from analysis			

Table 2.S3. Total rabies-labeled cell counts for Glutamatergic and GABAergic cell subclasses. Glutamatergic / Excitatory input cell subclasses are listed in (A), and GABAergic / Inhibitory cell subclasses are in (B). Input cell subclass is listed in the first column; each row corresponds to rabies-labeled cells of each type providing input to each layer, organized by mouse line (cre-expressing, layer-specific population). First column is raw count; 2nd column is percentage of total excitatory (A) or inhibitory (B) rabies-labeled cells for that mouse line.

A	**Glutamatergic Subclasses**									
	SepW1 - L2/3 IT		**Scnn1a - L4 IT**		**Tlx3 - L5 IT**		**Npr3 - L5 ET**		**Ntsr1 - L6 CT**	
Input cell type	# rabies cells	% E Rabies cells	# rabies cells	% E Rabies cells	# rabies cells	% E Rabies cells	# rabies cells	% E Rabies cells	# rabies cells	% E Rabies cells
L2/3 IT	354	20.67	2713	23.77	2730	25.61	670	15.25	1013	21.49
L4 IT	781	45.59	4473	39.20	3744	35.12	1241	28.25	1039	22.04
L5 IT	445	25.98	2664	23.34	2500	23.45	1290	29.36	1118	23.72
L5 NP	21	1.23	140	1.23	198	1.86	96	2.19	157	3.33
L5 ET	28	1.63	190	1.66	236	2.21	516	11.75	165	3.50
L6 CT	52	3.04	918	8.04	909	8.53	402	9.15	816	17.31
L6 IT	27	1.58	270	2.37	310	2.91	141	3.21	361	7.66
L6b	5	0.29	44	0.39	33	0.31	37	0.84	45	0.95
Total	**1713**	**100.00**	**11412**	**100.00**	**10660**	**100.00**	**4393**	**100.00**	**4714**	**100.00**

B	**GABAergic Subclasses**									
	SepW1 - L2/3 IT		**Scnn1a - L4 IT**		**Tlx3 - L5 IT**		**Npr3 - L5 ET**		**Ntsr1 - L6 CT**	
Input cell type	# rabies cells	% I Rabies cells	# rabies cells	% I Rabies cells	# rabies cells	% I Rabies cells	# rabies cells	% I Rabies cells	# rabies cells	% I Rabies cells
Lamp5	14	6.45	76	7.56	54	6.44	26	6.00	21	6.34
Meis2	0	0.00	0	0.00	0	0.00	0	0.00	0	0.00
Pvalb	118	54.38	607	60.40	517	61.62	287	66.28	209	63.14
Serpinf1	1	0.46	3	0.30	1	0.12	0	0.00	4	1.21
Sncg	2	0.92	3	0.30	2	0.24	2	0.46	1	0.30
Sst	68	31.34	215	21.39	161	19.19	78	18.01	53	16.01
Vip	14	6.45	101	10.05	104	12.40	40	9.24	43	12.99
Total	**217**	**100.00**	**1005**	**100.00**	**839**	**100.00**	**433**	**100.00**	**331**	**100.00**

Table 2.S4. Total rabies-labeled cell counts for inhibitory subtypes. Inhibitory subtype listed in far left column, rabies-labeled cell counts organized by layer-specific cre cell population (mouse line, 2nd row). For each mouse line, left column is raw cell count; right column represents the percentage of all rabies-labeled cells belonging to that inhibitory subclass. (A), counts for Pvalb subtypes; (B), for Sst subtypes; (C), for Vip subtypes; (D), for Lamp5 subtypes.

A	**Pvalb Subtypes**									
	SepW1 - L2/3 IT		**Scnn1a - L4 IT**		**Tlx3 - L5 IT**		**Npr3 - L5 ET**		**Ntsr1 - L6 CT**	
Input subtype	# rabies cells	% Pv Rabies cells	# rabies cells	% Pv Rabies cells	# rabies cells	% Pv Rabies cells	# rabies cells	% Pv Rabies cells	# rabies cells	% Pv Rabies cells
Pvalb Akr1c18 Ntf3	0	0.00	18	2.97	6	1.16	5	1.74	19	9.09
Pvalb Gpr149 Islr	4	3.39	89	14.66	94	18.18	115	40.07	32	15.31
Pvalb Reln Itm2a	57	48.31	300	49.42	242	46.81	91	31.71	67	32.06
Pvalb Reln Tac1	6	5.08	56	9.23	61	11.80	20	6.97	27	12.92
Pvalb Sema3e Kank4	5	4.24	22	3.62	22	4.26	6	2.09	34	16.27
Pvalb Tpbg	45	38.14	118	19.44	82	15.86	49	17.07	23	11.00
Other Pvalb	1	0.85	4	0.66	10	1.93	1	0.35	7	3.35
Total	**118**	**100.00**	**607**	**100.00**	**517**	**100.00**	**287**	**100.00**	**209**	**100.00**

B	**Sst Subtypes**									
	SepW1 - L2/3 IT		**Scnn1a - L4 IT**		**Tlx3 - L5 IT**		**Npr3 - L5 ET**		**Ntsr1 - L6 CT**	
Input cell type	# rabies cells	% Sst Rabies cells	# rabies cells	% Sst Rabies cells	# rabies cells	% Sst Rabies cells	# rabies cells	% Sst Rabies cells	# rabies cells	% Sst Rabies cells
Sst Calb2 Pdlim5	14	20.59	42	19.53	32	19.88	14	17.95	6	11.32
Sst Chodl	0	0.00	7	3.26	5	3.11	6	7.69	7	13.21
Sst Chrna2 Glra3	0	0.00	9	4.19	4	2.48	2	2.56	1	1.89
Sst Chrna2 Ptgdr	0	0.00	1	0.47	1	0.62	0	0.00	0	0.00
Sst Esm1	5	7.35	13	6.05	10	6.21	2	2.56	9	16.98
Sst Hpse Cbln4	14	20.59	42	19.53	22	13.66	6	7.69	5	9.43
Sst Hpse Sema3c	1	1.47	3	1.40	3	1.86	1	1.28	0	0.00
Sst Mme Fam114a1	13	19.12	39	18.14	21	13.04	9	11.54	4	7.55
Sst Myh8 Fibin	1	1.47	2	0.93	5	3.11	2	2.56	4	7.55
Sst Rxfp1 Eya1	4	5.88	13	6.05	17	10.56	10	12.82	5	9.43
Sst Rxfp1 Prdm8	1	1.47	7	3.26	7	4.35	7	8.97	2	3.77
Sst Tac1 Htr1d	7	10.29	12	5.58	13	8.07	6	7.69	3	5.66
Sst Tac1 Tacr3	4	5.88	6	2.79	5	3.11	2	2.56	1	1.89
Sst Tac2 Tacstd2	2	2.94	10	4.65	6	3.73	8	10.26	1	1.89
Other Sst	2	2.94	9	4.19	10	6.21	3	3.85	5	9.43
Total	**68**	**100.00**	**215**	**100.00**	**161**	**100.00**	**78**	**100.00**	**53**	**100.00**

C	**Vip Subtypes**									
	SepW1 - L2/3 IT		**Scnn1a - L4 IT**		**Tlx3 - L5 IT**		**Npr3 - L5 ET**		**Ntsr1 - L6 CT**	
Input cell type	# rabies cells	% Vip Rabies cells	# rabies cells	% Vip Rabies cells	# rabies cells	% Vip Rabies cells	# rabies cells	% Vip Rabies cells	# rabies cells	% Vip Rabies cells
Vip Chat Htr1f	3	21.43	17	16.83	16	15.38	6	15.00	3	6.98
Vip Crispld2 Kcne4	1	7.14	9	8.91	6	5.77	1	2.50	0	0.00
Vip Igfbp4 Mab21l1	2	14.29	16	15.84	12	11.54	5	12.50	7	16.28
Vip Igfbp6 Car10	0	0.00	2	1.98	2	1.92	0	0.00	2	4.65
Vip Igfbp6 Pltp	0	0.00	0	0.00	1	0.96	0	0.00	1	2.33
Vip Lect1 Oxtr	0	0.00	9	8.91	3	2.88	3	7.50	3	6.98
Vip Ptprt Pkp2	2	14.29	18	17.82	25	24.04	13	32.50	8	18.60
Vip Pygm C1ql1	0	0.00	6	5.94	5	4.81	3	7.50	1	2.33
Vip Rspo1 Itga4	1	7.14	4	3.96	5	4.81	2	5.00	0	0.00
Vip Rspo4 Rxfp1 Chat	4	28.57	14	13.86	28	26.92	6	15.00	17	39.53
Other Vip	1	7.14	6	5.94	1	0.96	1	2.50	1	2.33
Total	**14**	**100.00**	**101**	**100.00**	**104**	**100.00**	**40**	**100.00**	**43**	**100.00**

D	**Lamp5 Subtypes**									
	SepW1 - L2/3 IT		**Scnn1a - L4 IT**		**Tlx - L5 IT**		**Npr3 - L5 ET**		**Ntsr1 - L6 CT**	
Input cell type	# rabies cells	% Lamp5 Rabies cells	# rabies cells	% Lamp5 Rabies cells	# rabies cells	% Lamp5 Rabies cells	# rabies cells	% Lamp5 Rabies cells	# rabies cells	% Lamp5 Rabies cells
Lamp5 Fam19a1 Tmem182	1	7.14	0	0.00	1	1.85	0	0.00	0	0.00
Lamp5 Lsp1	8	57.14	55	72.37	39	72.22	20	76.92	17	80.95
Lamp5 Ntn1 Npy2r	2	14.29	8	10.53	9	16.67	2	7.69	3	14.29
Lamp5 Plch2 Dock5	1	7.14	5	6.58	1	1.85	1	3.85	1	4.76
Other Lamp5	2	14.29	8	10.53	4	7.41	3	11.54	0	0.00
Total	**14**	**100.00**	**76**	**100.00**	**54**	**100.00**	**26**	**100.00**	**21**	**100.00**

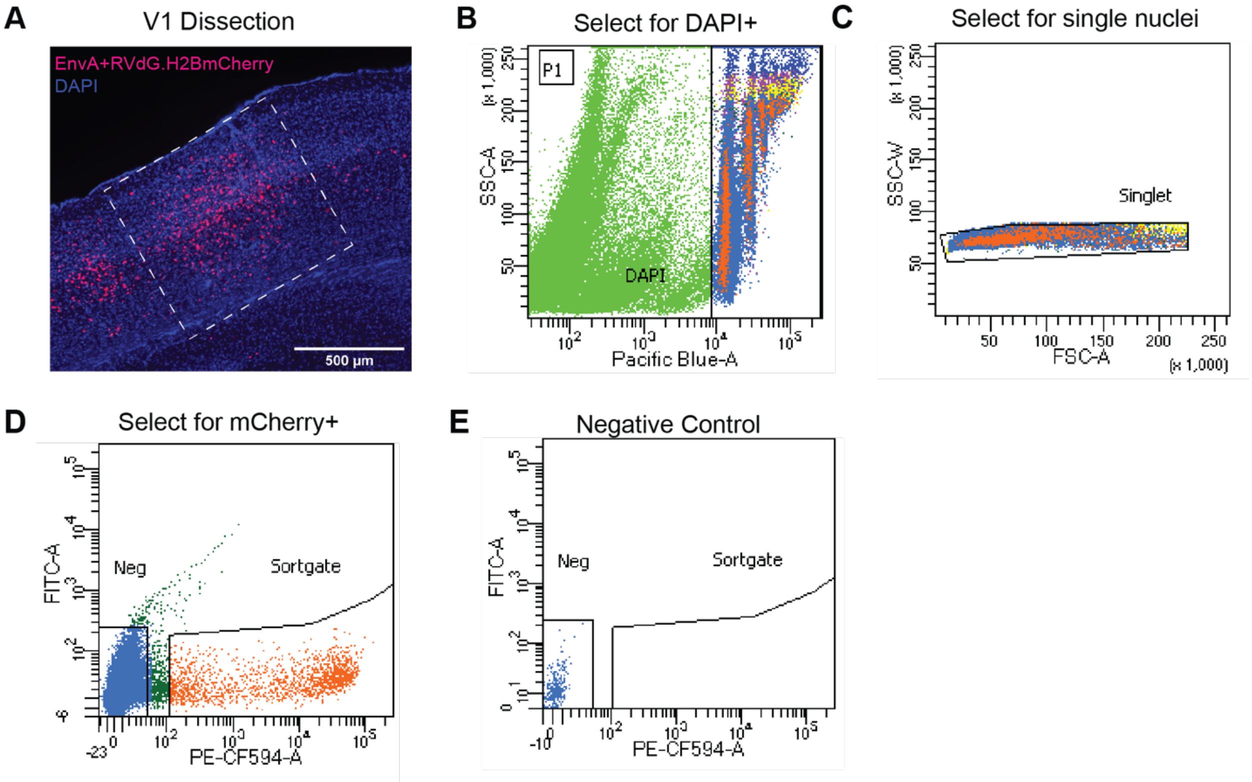

Figure 2.S1. V1 tissue dissection and subsequent FANS gating strategy.
(A). Example image of coronal brain slice from a monosynaptic rabies tracing experiment before V1 dissection. Dashed box indicates dissected region. Scale bar is 500um. (B-E). Detailed gating strategy of FAN sorting used for sorting mCherry+ rabies-labeled nuclei. (B) Gate selects for DAPI+ nuclei to exclude debris. (C) Gate to exclude cell doublets based on single nuclei morphology. (D) Gate to select for mCherry+ fluorescence. (E) Negative control sample.

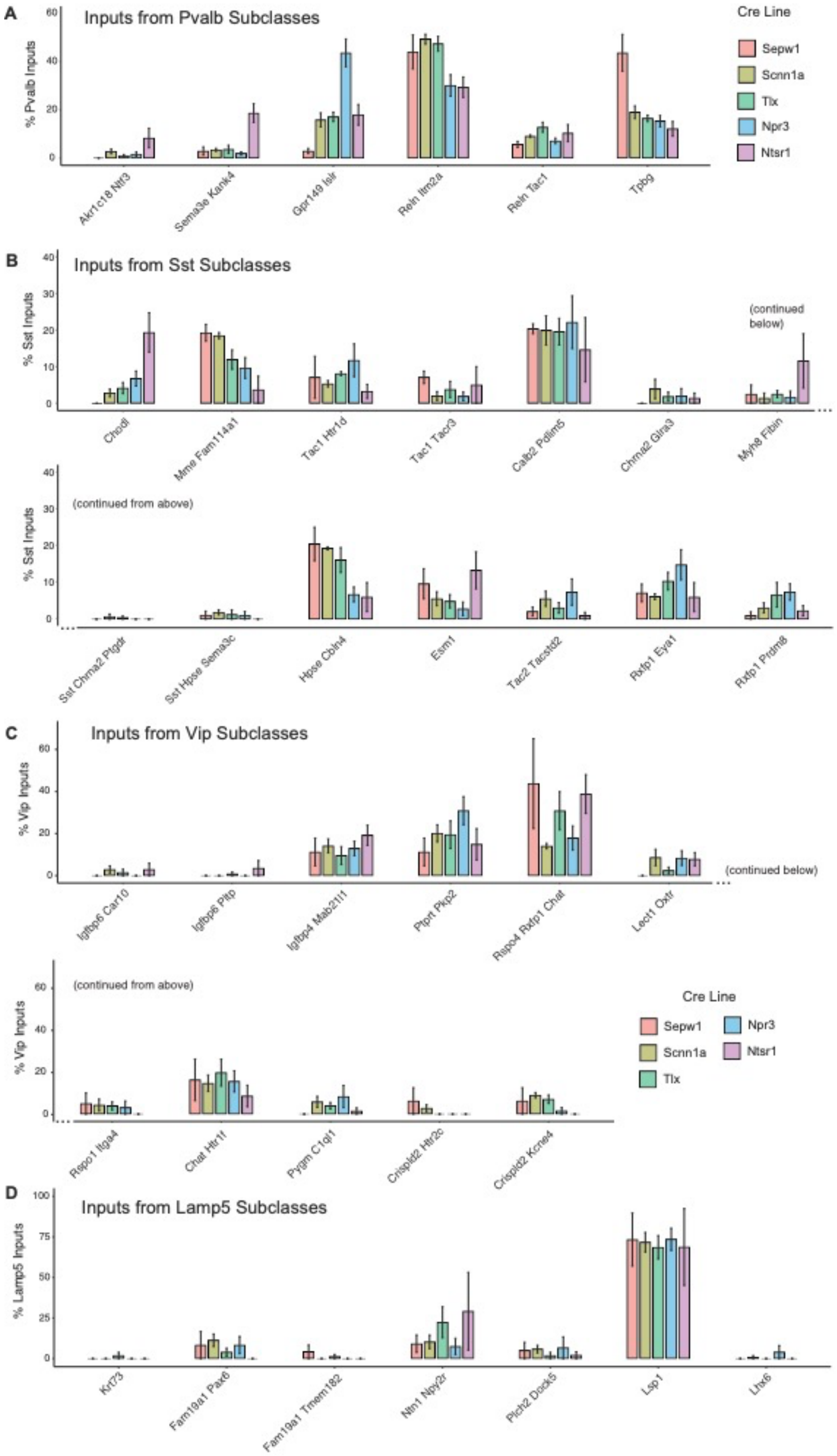

Figure 2.S2. Transcriptomic Subtypes Providing Input to Inhibitory Neurons in Mouse V1.
(A-D). Bar plots show proportion of inputs from subtypes of rabies-labeled neurons belonging to 4 distinct inhibitory subclasses, grouped by excitatory starter neuron populations (A), Input from the Pvalb subtypes to each cortical layer expressed as a percentage of input of all Pvalb inputs to the cre-expressing starter cell population. (B-D). Same as in (A), for Sst, Vip, and Lamp5 subtypes respectively. Statistical differences in input to each subtype across Cre lines using Wilcoxon sign rank test were not significant after correcting for multiple comparisons.

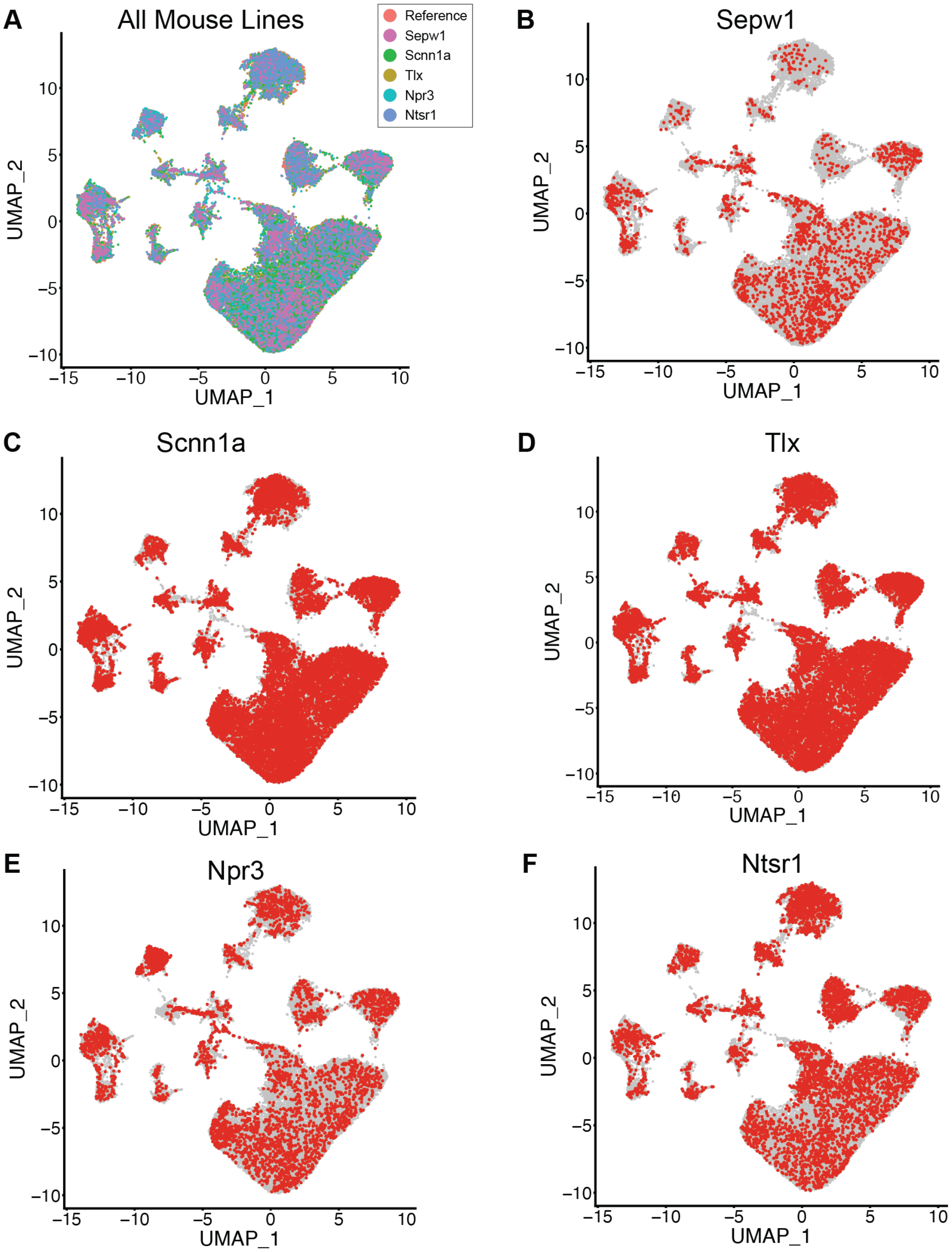

Figure 2.S3. UMAP Visualization of Excitatory Cells by Input population.
(A). Uniform manifold approximation (UMAP) visualization of 36,057 quality control (QC) filtered rabies-infected nuclei and 9,509 uninfected reference nuclei after anchor-based data integration colored by subclass annotations. Rabies-infected nuclei were obtained from 21 monosynaptic rabies tracing experiments across 5 different starter Cre mouse lines. (B) UMAP of nuclei passing QC colored by starter Cre mouse line of origin: Sepw1-Cre (n = 4, nuclei = 2,007), Scnn1a-Cre (n = 4, nuclei = 12,935), Tlx-Cre (n = 4, nuclei = 11,893), Npr3-Cre (n = 5, nuclei = 3,999), Ntsr1-Cre (n = 4, nuclei = 5,223). (C) UMAPs highlighting nuclei (red) obtained from each mouse line.

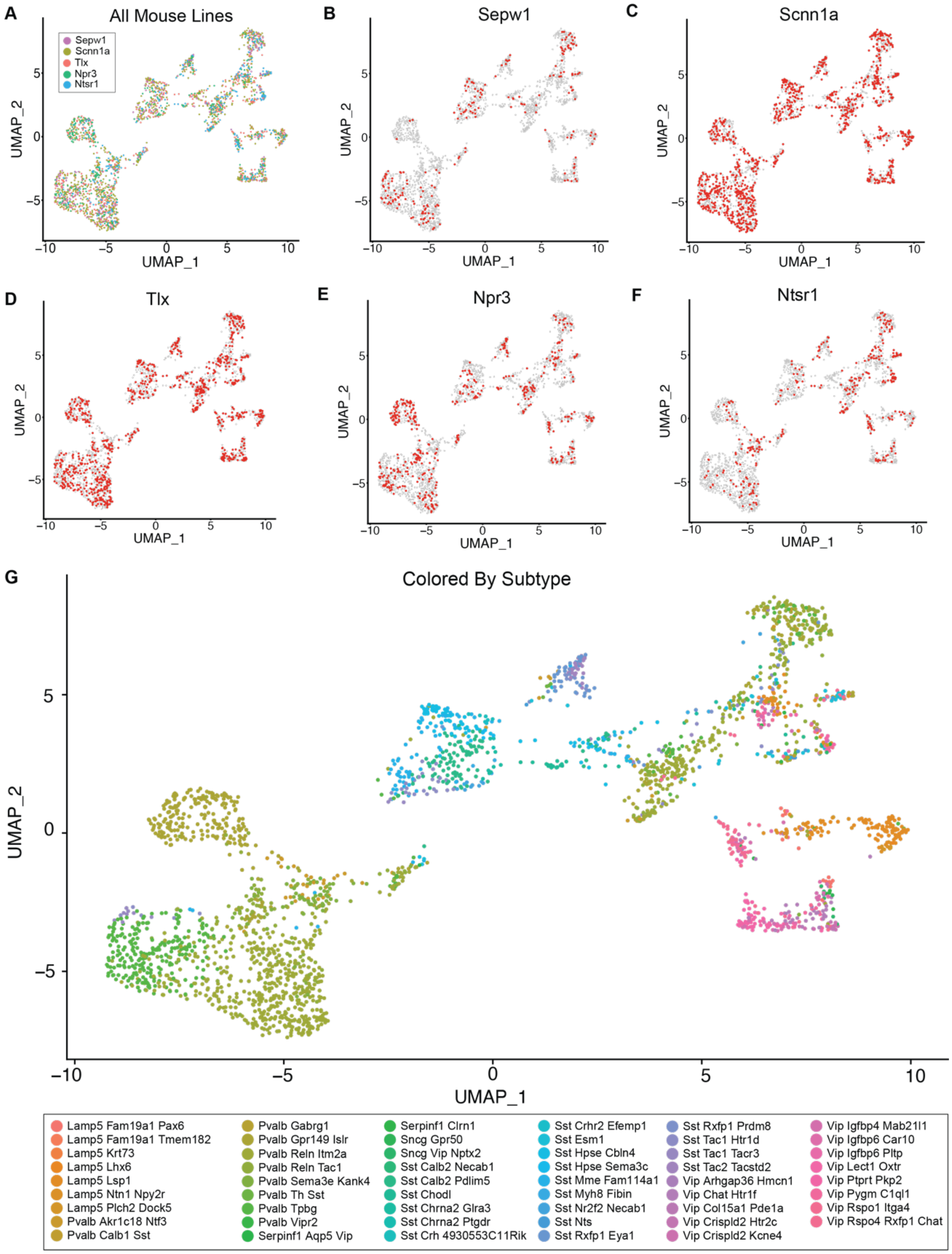

Figure 2.S4. UMAP Visualization of Inhibitory Cells by Starter Cre mouse line.
(A). Uniform manifold approximation (UMAP) visualization of 2825 quality control (QC) filtered rabies-infected nuclei from inhibitory cells across 5 different starter cell Cre mouse lines and 21 rabies-tracing experiments. Nuclei are colored by Starter Cre mouse line of origin. (B-F). UMAPs highlighting nuclei obtained from each starter Cre mouse line in red: Sepw1-Cre (n = 4, nuclei = 217), Scnn1a-Cre (n = 4, nuclei = 1,005), Tlx-Cre (n = 4, nuclei = 839), Npr3-Cre (n = 5, nuclei = 433), Ntsr1-Cre (n = 4, nuclei = 331). (G) UMAP visualization colored by approximate subtype annotations.

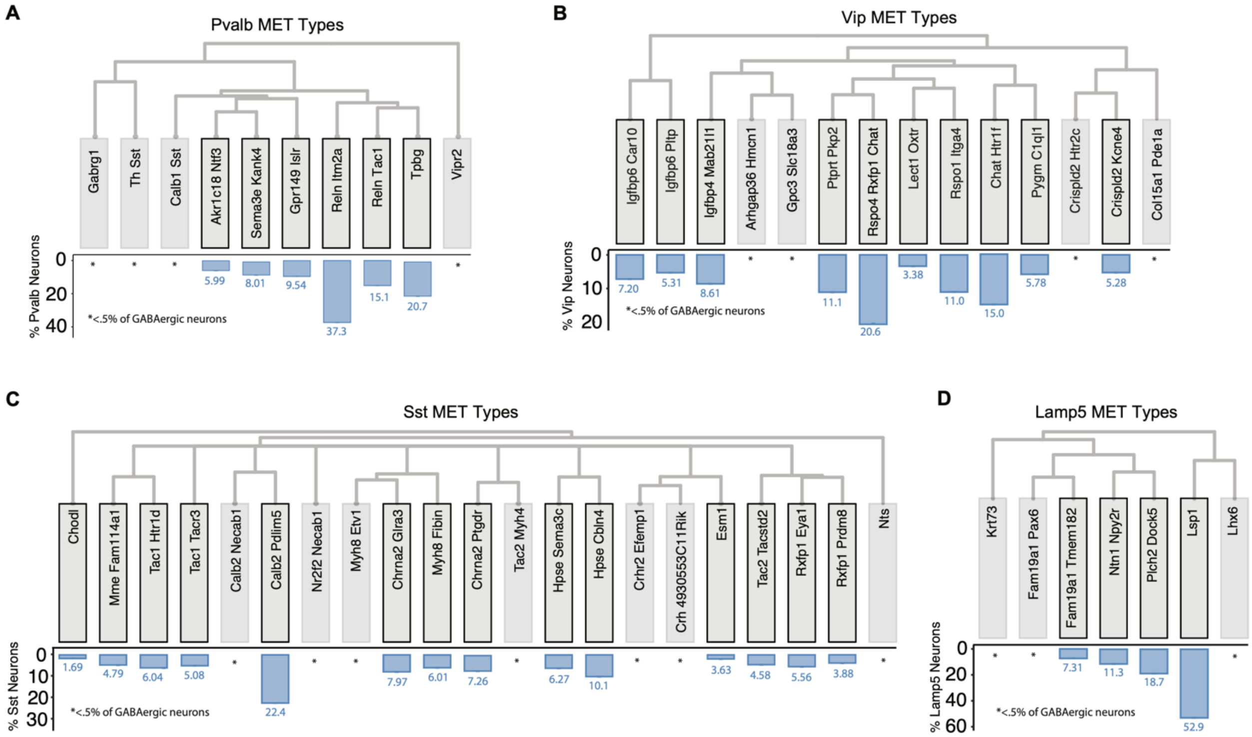

Figure 2.S5. Prevalence of Inhibitory Cell Types in Mouse V1.
(A-D). Dendrograms indicating the organization of Morphological, Electrophysiological and Transcriptomic (MET) cell types for Pvalb (A), Vip (B), Sst (C), and Lamp5 (D) neurons, obtained and adapted from the Allen Brain Map. Subtype names without a black outline and with an asterisk indicate rare cell subtypes, defined as those consisting of <.5% of all GABAergic neurons. Rare subtypes were excluded from main analyses (see Methods). Blue bars indicate relative frequency of each subtype within subclass of mouse V1 as determined by 10,000 iterations of random sampling from the control dataset.

Acknowledgments

Chapter 2, in full, is currently being prepared for submission for publication of the material. Patiño M & Rossa MA, Lagos WM, Patne N, Callaway EM (2023). The dissertation author was a co-first author and one of 2 primary investigators of this paper.

References

1. Zeng, H., & Sanes, J. R. (2017). Neuronal cell-type classification: Challenges, opportunities and the path forward. *Nature Reviews Neuroscience*, *18*(9), Article 9. https://doi.org/10.1038/nrn.2017.85
2. Bakken, T. E., Hodge, R. D., Miller, J. A., Yao, Z., Nguyen, T. N., Avermann, B., Barkan, E., Bertagnolli, D., Casper, T., Dee, N., Garren, E., Goldy, J., Graybuck, L. T., Kroll, M., Lasken, R. S., Lathia, K., Parry, S., Rimorin, C., Scheuermann, R. H., … Tasic, B. (2018). Single-nucleus and single-cell transcriptomes compared in matched cortical cell types. *PLOS ONE*, *13*(12), e0209648. https://doi.org/10.1371/journal.pone.0209648
3. Cadwell, C. R., Palasantza, A., Jiang, X., Berens, P., Deng, Q., Yilmaz, M., Reimer, J., Shen, S., Bethge, M., Tolias, K. F., Sandberg, R., & Tolias, A. S. (2016). Electrophysiological, transcriptomic and morphologic profiling of single neurons using Patch-seq. *Nature Biotechnology*, *34*(2), Article 2. https://doi.org/10.1038/nbt.3445
4. Tasic, B., Menon, V., Nguyen, T. N., Kim, T. K., Jarsky, T., Yao, Z., Levi, B., Gray, L. T., Sorensen, S. A., Dolbeare, T., Bertagnolli, D., Goldy, J., Shapovalova, N., Parry, S., Lee, C., Smith, K., Bernard, A., Madisen, L., Sunkin, S. M., … Zeng, H. (2016). Adult mouse cortical cell taxonomy revealed by single cell transcriptomics. *Nature Neuroscience*, *19*(2), 335–346. https://doi.org/10.1038/nn.4216
5. Tasic, B., Yao, Z., Graybuck, L. T., Smith, K. A., Nguyen, T. N., Bertagnolli, D., Goldy, J., Garren, E., Economo, M. N., Viswanathan, S., Penn, O., Bakken, T., Menon, V., Miller, J., Fong, O., Hirokawa, K. E., Lathia, K., Rimorin, C., Tieu, M., … Zeng, H. (2018). Shared and distinct transcriptomic cell types across neocortical areas. *Nature*, *563*(7729), 72–78. https://doi.org/10.1038/s41586-018-0654-5
6. Zeng, H. (2022). What is a cell type and how to define it? *Cell*, *185*(15), 2739–2755. https://doi.org/10.1016/j.cell.2022.06.031
7. Douglas, R. J., Koch, C., Mahowald, M., Martin, K. A. C., & Suarez, H. H. (1995). Recurrent Excitation in Neocortical Circuits. *Science*, *269*(5226), 981–985. https://doi.org/10.1126/science.7638624
8. Douglas, R. J., & Martin, K. A. C. (2004). Neuronal circuits of the neocortex. *Annual Review of Neuroscience*, *27*, 419–451. https://doi.org/10.1146/annurev.neuro.27.070203.144152
9. Douglas, R. J., & Martin, K. A. C. (2007). Mapping the Matrix: The Ways of Neocortex. *Neuron*, *56*(2), 226–238. https://doi.org/10.1016/j.neuron.2007.10.017

10. Kätzel, D., Zemelman, B. V., Buetfering, C., Wölfel, M., & Miesenböck, G. (2011). The columnar and laminar organization of inhibitory connections to neocortical excitatory cells. *Nature Neuroscience*, *14*(1), Article 1. https://doi.org/10.1038/nn.2687
11. Pfeffer, C. K., Xue, M., He, M., Huang, Z. J., & Scanziani, M. (2013). Inhibition of inhibition in visual cortex: The logic of connections between molecularly distinct interneurons. *Nature Neuroscience*, *16*(8), 1068–1076. https://doi.org/10.1038/nn.3446
12. Wall, N. R., Wickersham, I. R., Cetin, A., De La Parra, M., & Callaway, E. M. (2010). Monosynaptic circuit tracing in vivo through Cre-dependent targeting and complementation of modified rabies virus. *Proceedings of the National Academy of Sciences*, *107*(50), 21848–21853. https://doi.org/10.1073/pnas.1011756107
13. Wickersham, I. R., Finke, S., Conzelmann, K.-K., & Callaway, E. M. (2007). Retrograde neuronal tracing with a deletion-mutant rabies virus. *Nature Methods*, *4*(1), 47–49. https://doi.org/10.1038/nmeth999
14. Wickersham, I. R., Lyon, D. C., Barnard, R. J. O., Mori, T., Finke, S., Conzelmann, K.-K., Young, J. A. T., & Callaway, E. M. (2007). Monosynaptic Restriction of Transsynaptic Tracing from Single, Genetically Targeted Neurons. *Neuron*, *53*(5), 639–647. https://doi.org/10.1016/j.neuron.2007.01.033
15. Lacar, B., Linker, S. B., Jaeger, B. N., Krishnaswami, S. R., Barron, J. J., Kelder, M. J. E., Parylak, S. L., Paquola, A. C. M., Venepally, P., Novotny, M., O'Connor, C., Fitzpatrick, C., Erwin, J. A., Hsu, J. Y., Husband, D., McConnell, M. J., Lasken, R., & Gage, F. H. (2016). Nuclear RNA-seq of single neurons reveals molecular signatures of activation. *Nature Communications*, *7*(1), Article 1. https://doi.org/10.1038/ncomms11022
16. Ährlund-Richter, S., Xuan, Y., van Lunteren, J. A., Kim, H., Ortiz, C., Pollak Dorocic, I., Meletis, K., & Carlén, M. (2019). A whole-brain atlas of monosynaptic input targeting four different cell types in the medial prefrontal cortex of the mouse. *Nature Neuroscience*, *22*(4), 657–668. https://doi.org/10.1038/s41593-019-0354-y
17. Yetman, M. J., Washburn, E., Hyun, J. H., Osakada, F., Hayano, Y., Zeng, H., Callaway, E. M., Kwon, H.-B., & Taniguchi, H. (2019). Intersectional monosynaptic tracing for dissecting subtype-specific organization of GABAergic interneuron inputs. *Nature Neuroscience*, *22*(3), 492–502. https://doi.org/10.1038/s41593-018-0322-y
18. Kim, E. J., Juavinett, A. L., Kyubwa, E. M., Jacobs, M. W., & Callaway, E. M. (2015). Three Types of Cortical Layer 5 Neurons That Differ in Brain-wide Connectivity and Function. *Neuron*, *88*(6), 1253–1267. https://doi.org/10.1016/j.neuron.2015.11.002
19. Miyamichi, K., Shlomai-Fuchs, Y., Shu, M., Weissbourd, B. C., Luo, L., & Mizrahi, A. (2013). Dissecting Local Circuits: Parvalbumin Interneurons Underlie Broad Feedback Control of Olfactory Bulb Output. *Neuron*, *80*(5), 1232–1245. https://doi.org/10.1016/j.neuron.2013.08.027
20. Kim, E. J., Jacobs, M. W., Ito-Cole, T., & Callaway, E. M. (2016). Improved Monosynaptic Neural Circuit Tracing Using Engineered Rabies Virus Glycoproteins. *Cell Reports*, *15*(4), 692–699. https://doi.org/10.1016/j.celrep.2016.03.067
21. Gouwens, N. W., Sorensen, S. A., Berg, J., Lee, C., Jarsky, T., Ting, J., Sunkin, S. M., Feng, D., Anastassiou, C. A., Barkan, E., Bickley, K., Blesie, N., Braun, T., Brouner, K., Budzillo, A., Caldejon, S., Casper, T., Castelli, D., Chong, P., … Koch, C. (2019). Classification of electrophysiological and morphological neuron types in the mouse visual cortex. *Nature Neuroscience*, *22*(7), Article 7. https://doi.org/10.1038/s41593-019-0417-0

22. Patiño, M., Lagos, W. N., Patne, N. S., Tasic, B., Zeng, H., & Callaway, E. M. (2022). Single-cell transcriptomic classification of rabies-infected cortical neurons. *Proceedings of the National Academy of Sciences*, *119*(22), e2203677119. https://doi.org/10.1073/pnas.2203677119
23. Aran, D., Looney, A. P., Liu, L., Wu, E., Fong, V., Hsu, A., Chak, S., Naikawadi, R. P., Wolters, P. J., Abate, A. R., Butte, A. J., & Bhattacharya, M. (2019). Reference-based analysis of lung single-cell sequencing reveals a transitional profibrotic macrophage. *Nature Immunology*, *20*(2), Article 2. https://doi.org/10.1038/s41590-018-0276-y
24. Huang, Q., Liu, Y., Du, Y., & Garmire, L. X. (2021). Evaluation of Cell Type Annotation R Packages on Single-cell RNA-seq Data. *Genomics, Proteomics & Bioinformatics*, *19*(2), 267–281. https://doi.org/10.1016/j.gpb.2020.07.004
25. Gao, L., Liu, S., Wang, Y., Wu, Q., Gou, L., & Yan, J. (2023). Single-neuron analysis of dendrites and axons reveals the network organization in mouse prefrontal cortex. *Nature Neuroscience*, 1–16. https://doi.org/10.1038/s41593-023-01339-y
26. Gao, L., Liu, S., Gou, L., Hu, Y., Liu, Y., Deng, L., Ma, D., Wang, H., Yang, Q., Chen, Z., Liu, D., Qiu, S., Wang, X., Wang, D., Wang, X., Ren, B., Liu, Q., Chen, T., Shi, X., … Yan, J. (2022). Single-neuron projectome of mouse prefrontal cortex. *Nature Neuroscience*, *25*(4), Article 4. https://doi.org/10.1038/s41593-022-01041-5
27. Xu, X., Roby, K. D., & Callaway, E. M. (2010). Immunochemical characterization of inhibitory mouse cortical neurons: Three chemically distinct classes of inhibitory cells. *The Journal of Comparative Neurology*, *518*(3), 389–404. https://doi.org/10.1002/cne.22229
28. Ferguson, K. A., Salameh, J., Alba, C., Selwyn, H., Barnes, C., Lohani, S., & Cardin, J. A. (2023). VIP interneurons regulate cortical size tuning and visual perception. *BioRxiv*, 2023.03.14.532664. https://doi.org/10.1101/2023.03.14.532664
29. Gerfen, C. R., Paletzki, R., & Heintz, N. (2013). GENSAT BAC cre-recombinase driver lines to study the functional organization of cerebral cortical and basal ganglia circuits. *Neuron*, *80*(6), 1368–1383. https://doi.org/10.1016/j.neuron.2013.10.016
30. Gilbert, C. D. (1983). Microcircuitry of the visual cortex. *Annual Review of Neuroscience*, *Vol. 6*, 217–247. https://doi.org/10.1146/annurev.ne.06.030183.001245
31. Gilbert, C. D., & Wiesel, T. N. (1989). Columnar specificity of intrinsic horizontal and corticocortical connections in cat visual cortex. *The Journal of Neuroscience: The Official Journal of the Society for Neuroscience*, *9*(7), 2432–2442. https://doi.org/10.1523/JNEUROSCI.09-07-02432.1989
32. Brown, S. P., & Hestrin, S. (2009). Intracortical circuits of pyramidal neurons reflect their long-range axonal targets. *Nature*, *457*(7233), 1133–1136. https://doi.org/10.1038/nature07658
33. Brown, A. P. Y., Cossell, L., & Margrie, T. W. (2020). *Excitatory and inhibitory L2/3 neurons in mouse primary visual cortex are balanced in their input connectivity* (p. 2020.04.21.053504). bioRxiv. https://doi.org/10.1101/2020.04.21.053504
34. Pfeffer, C. K., & Beltramo, R. (2017). Correlating Anatomy and Function with Gene Expression in Individual Neurons by Combining in Vivo Labeling, Patch Clamp, and Single Cell RNA-seq. *Frontiers in Cellular Neuroscience*, *11*. https://www.frontiersin.org/article/10.3389/fncel.2017.00376

35. DeNardo, L. A., Berns, D. S., DeLoach, K., & Luo, L. (2015). Connectivity of mouse somatosensory and prefrontal cortex examined with trans-synaptic tracing. *Nature Neuroscience*, *18*(11), 1687–1697. https://doi.org/10.1038/nn.4131
36. Hage, T. A., Bosma-Moody, A., Baker, C. A., Kratz, M. B., Campagnola, L., Jarsky, T., Zeng, H., & Murphy, G. J. (2022). Synaptic connectivity to L2/3 of primary visual cortex measured by two-photon optogenetic stimulation. *ELife*, *11*, e71103. https://doi.org/10.7554/eLife.71103
37. Rossi, M. A., Basiri, M. L., Liu, Y., Hashikawa, Y., Hashikawa, K., Fenno, L. E., Kim, Y. S., Ramakrishnan, C., Deisseroth, K., & Stuber, G. D. (2021). Transcriptional and functional divergence in lateral hypothalamic glutamate neurons projecting to the lateral habenula and ventral tegmental area. *Neuron*, *109*(23), 3823-3837.e6. https://doi.org/10.1016/j.neuron.2021.09.020
38. Wertz, A., Trenholm, S., Yonehara, K., Hillier, D., Raics, Z., Leinweber, M., Szalay, G., Ghanem, A., Keller, G., Rózsa, B., Conzelmann, K.-K., & Roska, B. (2015). Single-cell–initiated monosynaptic tracing reveals layer-specific cortical network modules. *Science*, *349*(6243), 70–74. https://doi.org/10.1126/science.aab1687
39. Yao, Z., van Velthoven, C. T. J., Nguyen, T. N., Goldy, J., Sedeno-Cortes, A. E., Baftizadeh, F., Bertagnolli, D., Casper, T., Chiang, M., Crichton, K., Ding, S.-L., Fong, O., Garren, E., Glandon, A., Gouwens, N. W., Gray, J., Graybuck, L. T., Hawrylycz, M. J., Hirschstein, D., … Zeng, H. (2021). A taxonomy of transcriptomic cell types across the isocortex and hippocampal formation. *Cell*, *184*(12), 3222-3241.e26. https://doi.org/10.1016/j.cell.2021.04.021
40. Harris, J. A., Mihalas, S., Hirokawa, K. E., Whitesell, J. D., Choi, H., Bernard, A., Bohn, P., Caldejon, S., Casal, L., Cho, A., Feiner, A., Feng, D., Gaudreault, N., Gerfen, C. R., Graddis, N., Groblewski, P. A., Henry, A. M., Ho, A., Howard, R., … Zeng, H. (2019). Hierarchical organization of cortical and thalamic connectivity. *Nature*, *575*(7781), Article 7781. https://doi.org/10.1038/s41586-019-1716-z
41. Campagnola, L., Seeman, S. C., Chartrand, T., Kim, L., Hoggarth, A., Gamlin, C., Ito, S., Trinh, J., Davoudian, P., Radaelli, C., Kim, M.-H., Hage, T., Braun, T., Alfiler, L., Andrade, J., Bohn, P., Dalley, R., Henry, A., Kebede, S., … Jarsky, T. (2022). Local connectivity and synaptic dynamics in mouse and human neocortex. *Science*, *375*(6585), eabj5861. https://doi.org/10.1126/science.abj5861
42. DeNardo, L. A., Berns, D. S., DeLoach, K., & Luo, L. (2015). Connectivity of mouse somatosensory and prefrontal cortex examined with trans-synaptic tracing. *Nature Neuroscience*, *18*(11), 1687–1697. https://doi.org/10.1038/nn.4131
43. Voelcker, B., Pancholi, R., & Peron, S. (2022). Transformation of primary sensory cortical representations from layer 4 to layer 2. *Nature Communications*, *13*(1), Article 1. https://doi.org/10.1038/s41467-022-33249-1
44. Yao, S., Wang, Q., Hirokawa, K. E., Ouellette, B., Ahmed, R., Bomben, J., Brouner, K., Casal, L., Caldejon, S., Cho, A., Dotson, N. I., Daigle, T. L., Egdorf, T., Enstrom, R., Gary, A., Gelfand, E., Gorham, M., Griffin, F., Gu, H., … Zeng, H. (2023). A whole-brain monosynaptic input connectome to neuron classes in mouse visual cortex. *Nature Neuroscience*, *26*(2), Article 2. https://doi.org/10.1038/s41593-022-01219-x
45. Jiang, X., Shen, S., Cadwell, C. R., Berens, P., Sinz, F., Ecker, A. S., Patel, S., & Tolias, A. S. (2015). Principles of connectivity among morphologically defined cell types in adult neocortex. *Science*, *350*(6264), aac9462. https://doi.org/10.1126/science.aac9462

46. Lefort, S., Tomm, C., Sarria, J.-C. F., & Petersen, C. C. H. (2009). The Excitatory Neuronal Network of the C2 Barrel Column in Mouse Primary Somatosensory Cortex. *Neuron*, *61*(4), 301–316. https://doi.org/10.1016/j.neuron.2008.12.020
47. Gouwens, N. W., Sorensen, S. A., Baftizadeh, F., Budzillo, A., Lee, B. R., Jarsky, T., Alfiler, L., Baker, K., Barkan, E., Berry, K., Bertagnolli, D., Bickley, K., Bomben, J., Braun, T., Brouner, K., Casper, T., Crichton, K., Daigle, T. L., Dalley, R., … Zeng, H. (2020). Integrated Morphoelectric and Transcriptomic Classification of Cortical GABAergic Cells. *Cell*, *183*(4), 935-953.e19. https://doi.org/10.1016/j.cell.2020.09.057
48. He, M., Tucciarone, J., Lee, S., Nigro, M. J., Kim, Y., Levine, J. M., Kelly, S. M., Krugikov, I., Wu, P., Chen, Y., Gong, L., Hou, Y., Osten, P., Rudy, B., & Huang, Z. J. (2016). Strategies and Tools for Combinatorial Targeting of GABAergic Neurons in Mouse Cerebral Cortex. *Neuron*, *91*(6), 1228–1243. https://doi.org/10.1016/j.neuron.2016.08.021
49. Kilduff, T. S., Cauli, B., & Gerashchenko, D. (2011). Activation of Cortical Interneurons During Sleep: An Anatomical Link to Homeostatic Sleep Regulation? *Trends in Neurosciences*, *34*(1), 10–19. https://doi.org/10.1016/j.tins.2010.09.005
50. Paul, A., Crow, M., Raudales, R., He, M., Gillis, J., & Huang, Z. J. (2017). Transcriptional Architecture of Synaptic Communication Delineates GABAergic Neuron Identity. *Cell*, *171*(3), 522-539.e20. https://doi.org/10.1016/j.cell.2017.08.032
51. Tasic, B., Yao, Z., Graybuck, L. T., Smith, K. A., Nguyen, T. N., Bertagnolli, D., Goldy, J., Garren, E., Economo, M. N., Viswanathan, S., Penn, O., Bakken, T., Menon, V., Miller, J., Fong, O., Hirokawa, K. E., Lathia, K., Rimorin, C., Tieu, M., … Zeng, H. (2018). Shared and distinct transcriptomic cell types across neocortical areas. *Nature*, *563*(7729), 72–78. https://doi.org/10.1038/s41586-018-0654-5
52. Atallah, B. V., Bruns, W., Carandini, M., & Scanziani, M. (2012). Parvalbumin-Expressing Interneurons Linearly Transform Cortical Responses to Visual Stimuli. *Neuron*, *73*(1), 159–170. https://doi.org/10.1016/j.neuron.2011.12.013
53. Fino, E., Packer, A. M., & Yuste, R. (2013). The Logic of Inhibitory Connectivity in the Neocortex. *The Neuroscientist*, *19*(3), 228–237. https://doi.org/10.1177/1073858412456743
54. Yavorska, I., & Wehr, M. (2016). Somatostatin-Expressing Inhibitory Interneurons in Cortical Circuits. *Frontiers in Neural Circuits*, *10*. https://doi.org/10.3389/fncir.2016.00076
55. Muñoz, W., Tremblay, R., Levenstein, D., & Rudy, B. (2017). Layer-specific modulation of neocortical dendritic inhibition during active wakefulness. *Science*, *355*(6328), 954–959. https://doi.org/10.1126/science.aag2599
56. Nigro, M. J., Hashikawa-Yamasaki, Y., & Rudy, B. (2018). Diversity and Connectivity of Layer 5 Somatostatin-Expressing Interneurons in the Mouse Barrel Cortex. *The Journal of Neuroscience*, *38*(7), 1622–1633. https://doi.org/10.1523/JNEUROSCI.2415-17.2017
57. Cadwell, C. R., Scala, F., Li, S., Livrizzi, G., Shen, S., Sandberg, R., Jiang, X., & Tolias, A. S. (2017). Multimodal profiling of single-cell morphology, electrophysiology, and gene expression using Patch-seq. *Nature Protocols*, *12*(12), Article 12. https://doi.org/10.1038/nprot.2017.120
58. Kim, J., Matney, C. J., Blankenship, A., Hestrin, S., & Brown, S. P. (2014). Layer 6 Corticothalamic Neurons Activate a Cortical Output Layer, Layer 5a. *Journal of Neuroscience*, *34*(29), 9656–9664. https://doi.org/10.1523/JNEUROSCI.1325-14.2014

59. Yamawaki, N., & Shepherd, G. M. G. (2015). Synaptic Circuit Organization of Motor Corticothalamic Neurons. *Journal of Neuroscience*, *35*(5), 2293–2307. https://doi.org/10.1523/JNEUROSCI.4023-14.2015

60. BRAIN Initiative Cell Census Network (BICCN), BRAIN Initiative Cell Census Network (BICCN) Corresponding authors, Callaway, E. M., Dong, H.-W., Ecker, J. R., Hawrylycz, M. J., Huang, Z. J., Lein, E. S., Ngai, J., Osten, P., Ren, B., Tolias, A. S., White, O., Zeng, H., Zhuang, X., BICCN contributing principal investigators, Ascoli, G. A., Behrens, M. M., Chun, J., … Sunkin, S. (2021). A multimodal cell census and atlas of the mammalian primary motor cortex. *Nature*, *598*(7879), 86–102. https://doi.org/10.1038/s41586-021-03950-0

61. Lein, E. S., Hawrylycz, M. J., Ao, N., Ayres, M., Bensinger, A., Bernard, A., Boe, A. F., Boguski, M. S., Brockway, K. S., Byrnes, E. J., Chen, L., Chen, L., Chen, T.-M., Chi Chin, M., Chong, J., Crook, B. E., Czaplinska, A., Dang, C. N., Datta, S., … Jones, A. R. (2007). Genome-wide atlas of gene expression in the adult mouse brain. *Nature*, *445*(7124), Article 7124. https://doi.org/10.1038/nature05453

62. Scala, F., Kobak, D., Bernabucci, M., Bernaerts, Y., Cadwell, C. R., Castro, J. R., Hartmanis, L., Jiang, X., Laturnus, S., Miranda, E., Mulherkar, S., Tan, Z. H., Yao, Z., Zeng, H., Sandberg, R., Berens, P., & Tolias, A. S. (2021). Phenotypic variation of transcriptomic cell types in mouse motor cortex. *Nature*, *598*(7879), Article 7879. https://doi.org/10.1038/s41586-020-2907-3

63. Peng, H., Xie, P., Liu, L., Kuang, X., Wang, Y., Qu, L., Gong, H., Jiang, S., Li, A., Ruan, Z., Ding, L., Yao, Z., Chen, C., Chen, M., Daigle, T. L., Dalley, R., Ding, Z., Duan, Y., Feiner, A., … Zeng, H. (2021). Morphological diversity of single neurons in molecularly defined cell types. *Nature*, *598*(7879), 174–181. https://doi.org/10.1038/s41586-021-03941-1

64. Yao, Z., Liu, H., Xie, F., Fischer, S., Adkins, R. S., Aldridge, A. I., Ament, S. A., Bartlett, A., Behrens, M. M., Van den Berge, K., Bertagnolli, D., de Bézieux, H. R., Biancalani, T., Booeshaghi, A. S., Bravo, H. C., Casper, T., Colantuoni, C., Crabtree, J., Creasy, H., … Mukamel, E. A. (2021). A transcriptomic and epigenomic cell atlas of the mouse primary motor cortex. *Nature*, *598*(7879), 103–110. https://doi.org/10.1038/s41586-021-03500-8

65. Daigle, T. L., Madisen, L., Hage, T. A., Valley, M. T., Knoblich, U., Larsen, R. S., Takeno, M. M., Huang, L., Gu, H., Larsen, R., Mills, M., Bosma-Moody, A., Siverts, L. A., Walker, M., Graybuck, L. T., Yao, Z., Fong, O., Nguyen, T. N., Garren, E., … Zeng, H. (2018). A Suite of Transgenic Driver and Reporter Mouse Lines with Enhanced Brain-Cell-Type Targeting and Functionality. *Cell*, *174*(2), 465-480.e22. https://doi.org/10.1016/j.cell.2018.06.035

66. Madisen, L., Zwingman, T. A., Sunkin, S. M., Oh, S. W., Zariwala, H. A., Gu, H., Ng, L. L., Palmiter, R. D., Hawrylycz, M. J., Jones, A. R., Lein, E. S., & Zeng, H. (2010). A robust and high-throughput Cre reporting and characterization system for the whole mouse brain. *Nature Neuroscience*, *13*(1), 133–140. https://doi.org/10.1038/nn.2467

67. Butler, A., Hoffman, P., Smibert, P., Papalexi, E., & Satija, R. (2018). Integrating single-cell transcriptomic data across different conditions, technologies, and species. *Nature Biotechnology*, *36*(5), 411–420. https://doi.org/10.1038/nbt.4096

68. Stuart, T., Butler, A., Hoffman, P., Hafemeister, C., Papalexi, E., Mauck, W. M., Hao, Y., Stoeckius, M., Smibert, P., & Satija, R. (2019). Comprehensive Integration of Single-Cell Data. *Cell*, *177*(7), 1888-1902.e21. https://doi.org/10.1016/j.cell.2019.05.031

69. McGinnis, C. S., Patterson, D. M., Winkler, J., Conrad, D. N., Hein, M. Y., Srivastava, V., Hu, J. L., Murrow, L. M., Weissman, J. S., Werb, Z., Chow, E. D., & Gartner, Z. J. (2019). MULTI-seq: Sample multiplexing for single-cell RNA sequencing using lipid-tagged indices. *Nature Methods*, *16*(7), 619–626. https://doi.org/10.1038/s41592-019-0433-8